MReadings: MR in RT

Contributions of our MAGNETOM users
4th Edition ESTRO 2018

Not for distribution in the US

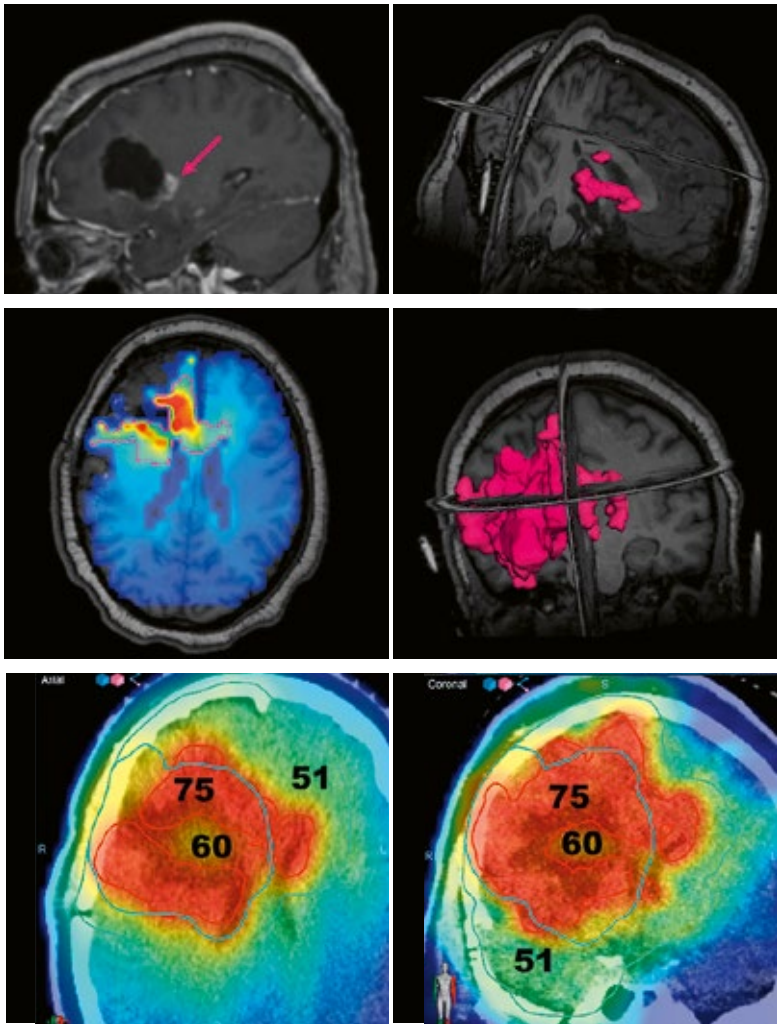

siemens.com/magnetom-world-rt

SIEMENS Healthineers

Paul Keall is a Professor in the Sydney Medical School at the University of Sydney, Australia, and an NHMRC Senior Professorial Research Fellow. Prior to his current role, he was the Director of the Radiation Physics Division at Stanford University, Standford, CA, USA.

At the University of Sydney Professor Keall and his team of 25 scientists have the mission to create, share and apply novel cancer imaging and targeted radiotherapy methods that improve human health. His team has achieved significant bench-to-bedside clinical translational milestones in cancer imaging and targeted radiotherapy. Additional programs include the research and development of the Australian MRI-Linear accelerator, and the Nano-X cancer radiotherapy system.

Professor Keall's research is funded by over $25M of competitive government grant funding. The scientific work has resulted in over 270 articles with a high number of citations (h-index 46). He is regularly invited to speak at large international meetings. The cutting edge technological nature of the research has resulted in a number of patents, licenses and industrial engagement, including founding two companies.

Professor Keall is engaged professionally in several roles within the American Association of Physicists in Medicine (AAPM) and the American Society for Radiation Oncology. Outside of work, he enjoys time with his family, and all forms of sport.

Sydney, Australia

MRI and cancer radiotherapy

As I write this editorial I see dawn's silhouette through the trees, the first rays from the sun, and the promise of the new day. We are also seeing the dawn of MRI in radiotherapy as its own specialty, confirmed by the fast-growing annual international meeting held in Sydney, Australia in 2017 and Utrecht in the Netherlands this year[1]. These meetings demonstrate the clinical, scientific and industrial interest in maximizing the role and value of MRI in cancer radiotherapy.

Of the estimated 17 million new cancers diagnosed in 2018[2], evidence suggests 48% of these patients [1] – more than 8 million – should be treated with radiotherapy. The good news is that due to the reduction in smoking and advances in early detection and treatment that cancer mortality is dropping nearly 2% per year[3].

In this editorial I will briefly describe a few areas where MRI is and could change clinical practice and outcomes in radiotherapy.

MRI as the primary tool to delineate the cancer target in radiotherapy

MRI is generally acknowledged as the best imaging modality to differentiate soft tissue, but is challenging to provide the underlying image data and geometric fidelity needed for the accurate radiation transport required for modern radiotherapy planning. Through the development of elegant new methods, e.g. [2], and careful understanding and addressing each source of error in the treatment pathway [3], MRI-only planning[4] is becoming mainstream in some centers. MRI-only planning has the benefits of avoiding the imaging dose, cost and additional work associated with CT scanning, and can also reduce some uncertainties, such as the MRI to CT registration challenge. In this issue you will find articles describing the role of MRI-only planning for prostate cancer [4], head and neck cancer [5], proton therapy [6], stereotactic radiosurgery [7] and the central role of MRI in image-guided brachytherapy [8]. Collectively, these articles represent a myriad of approaches that bring MRI as the central modality for one of the most critical and uncertain steps in the cancer radiotherapy process, target delineation. Hopefully the role of MRI can reduce uncertainty, improve consistency and allow us to better understand the spatiotemporal nature of tumor and normal tissue response to radiotherapy.

MRI for dose escalation

One of the most attractive features of MRI is the broad availability of ways to measure tumor physiology, such as the spectroscopic MRI [9] study discussed here. The use of functional MRI opens up new opportunities for selective dose escalation, to provide increased amounts of radiation to the parts of the tumors that are most aggressive, radioresistant and/or have high metastatic potential. I personally feel this is one of the most exciting applications of MRI in radiotherapy with the potential to have a significant impact on cancer outcomes.

MRI for motion assessment

The description of the use of MRI to measure laryngeal motion [10] is one example of the role of MRI for motion assessment, quantification and margin assessment for radiotherapy. Studies in the larynx and other sites reinforce the complexity of motion where not only the primary target but surrounding critical tissues can be moving, rotating and deforming due to normal physiological function such as breathing, swallowing and digesting. The ability to measure complex motion for individual patients creates opportunities for personalized medicine, to give the appropriate patient-specific margin maximizing the probability of tumor coverage and minimizing normal tissue toxicity on an individual level.

MRI for response assessment

Two articles in this issue describe the role of MRI in tumor response [11], as well as normal tissue response [12]. Serial MRI, with its exquisite soft tissue imaging capabilities, will enable us to get a much better understanding of radiation effects on cancer and normal anatomy, providing us with addition information to inform future radiobiological response models and treatment plans.

The growth of 4D MRI

Two articles in this issue [13, 14] describe the investigation of 4D MRI methods which is an active area of research and development. It is interesting to draw a parallel between 4D MRI and the development of 4D CT imaging in the early 2000s. 4D CT imaging started with a few centers developing in-house solutions. Once vendors enabled the technology the technology uptake was approximately

[1] www.mrinrt2018.com
[2] https://www.cancer.org/content/dam/cancer-org/research/cancer-facts-and-statistics/annual-cancer-facts-and- figures/2018/cancer-facts-and-figures-2018.pdf
[3] https://www.cancer.org/latest-news/facts-and-figures-2018-rate-of-deaths-from-cancer-continues-decline.html
[4] The product is not commercially available. Radiotherapy where MR data is the only imaging information is ongoing research. The concepts and information presented in this article are based on research and are not commercially available. Its future availability cannot be ensured. Not for clinical use.
[5] https://www.henryford.com/news/2017/07/viewray-firstpatient

7% per year resulting in over 40% of centers offering this technology by 2009 [15]. 4D CT is now a mainstream tool for lung cancer radiotherapy. It will be interesting to watch the growth and transition of 4D MRI from an investigative tool to a mainstream clinical instrument.

MRI as the primary tool to track cancer during treatment

2017 was an amazing year for integrated MRI-Linear accelerators (MRI-Linacs). The first MRI-Linac patient treatments were performed in Utrecht [16] and ViewRay successfully transitioned its MRIdian system from a cobalt radioisotope to a linac source, with the first patients treated at Henry Ford Hospital[5]. Adaptive radiotherapy, a long standing challenge for traditional linacs, has become mainstream on ViewRay's integrated radiotherapy systems [17]. The early clinical findings for pancreas cancer [18] have raised tremendous interest in the community and, if validated, will transform patterns of care for many cancer patients.

MRI to unleash the potential of proton therapy?

Based on the physics and multiple planning studies, would expect particle therapy to show markedly reduced clinical toxicity. However, the data to date which includes a retrospective SEER database medical claims review for prostate cancer [19], systematic review of early stage lung cancer [20] and prospective randomized clinical lung cancer trial [21] have yet to unequivocally clinically realize this expectation. This mismatch between expected and observed outcomes leads to a compelling hypothesis: advanced image guidance – the ultimate being real-time MRI – is required to unleash the clinical potential of particle therapy. A recent Future of Medical Physics paper reviews and describes the potential and barriers for MRI-guided particle therapy [22].

Research is global as reflected by the varied contributions to this issue of MReadings. It is heartening to see researchers from 'down-under' active in the topics discussed and providing three articles for this issue.

Enjoy!

Paul Keall

References

1 Barton MB, Jacob S, Shafiq J, et al. Estimating the demand for radiotherapy from the evidence: a review of changes from 2003 to 2012. Radioth Onc. 2014;112(1):140-144.
2 Dowling JA, Lambert J, Parker J, et al. An Atlas-Based Electron Density Mapping Method for Magnetic Resonance Imaging (MRI)-Alone Treatment Planning and Adaptive MRI-Based Prostate Radiation Therapy. Int J Rad Onc Biol Phys. 2012;83(1):e5-e11.
3 Kapanen M, Collan J, Beule A, Seppälä T, Saarilahti K, Tenhunen M. Commissioning of MRI-only based treatment planning procedure for external beam radiotherapy of prostate. Magnetic resonance in medicine. 2013;70(1):127-135.
4 Mourtada F, Prisciandaro, JI, et al. MRI for prostate and gynecol-ogicalbrachytherapy is here to stay. See also page 10 of this issue.
5 Thorwarth D, Nikolaou K, et al. MR-simulation for radiotherapy treatment planning of head and neck cancer using 3T MAGNETOM Vida. See also page 22 of this issue.
6 Huijsse SEM, Borra RJH, et al. MR-only guided proton therapy: advances, future perspectives and challenges. See also page 16 of this issue.
7 Fatemi A, Taghizadeh S, et al. Optimizing MRI sequences and images for MRI-based stereotactic radiosurgery treatment planning. See also page 28 of this issue.
8 Mourtada F, Prisciandaro JI, et al. MRI for prostate and gynecol-ogical brachytherapy is here to stay. See also page 10 of this issue.
9 Shim H, Gurbani SS, et al. Spectroscopic MRI for dose-escalated radiation therapy. See also page 40 of this issue.
10 Bahig H, Lambert L, et al. Dynamic 2D magnetic resonance imaging for assessment of larynx motion in early glottic cancer radiotherapy. See also page 25 of this issue.
11 Emblem KE, Grøvik E, et al. TREATMENT: Improved therapy response assessment in metastatic brain tumors. See also page 37 of this issue.
12 Liney G, Tang S. MyoMap quantification of myocardial toxicity following concurrent chemoradiotherapy for esophageal carcinoma. See also page 44 of this issue.
13 Oar A, Liney G, Lee M, et al. First experience of 4D-MRI for abdominal radiotherapy planning. See also page 50 of this issue.
14 Ken S, Parent L, et al. 4D-MRI Sequence for Radiotherapy Application: Validation of a Retrospective Method on a Motion Phantom. See also page 54 of this issue.
15 Simpson DR, Lawson JD, Nath SK, Rose BS, Mundt AJ, Mell LK. Utilization of advanced imaging technologies for target delineation in radiation oncology. Journal of the American College of Radiology. 2009;6(12):876-883.
16 Raaymakers B, Jürgenliemk-Schulz I, Bol G, et al. First patients treated with a 1.5T MRI-Linac: clinical proof of concept of a high-precision, high-field MRI guided radiotherapy treatment. Physics in Medicine & Biology. 2017;62(23):L41.
17 Acharya S, Fischer-Valuck BW, Kashani R, et al. Online magnetic resonance image guided adaptive radiation therapy: first clinical applications. International Journal of Radiation Oncology• Biology• Physics. 2016;94(2):394-403.
18 Rudra S, Jiang N, Rosenberg S, et al. High dose adaptive MRI guided radiation therapy improves overall survival of inoperable pancreatic cancer. International Journal of Radiation Oncology• Biology• Physics. 2017;99(2):E184.
19 Yu JB, Soulos PR, Herrin J, et al. Proton versus intensity-modulated radiotherapy for prostate cancer: patterns of care and early toxicity. Journal of the National Cancer Institute. 2012;105(1):25-32.
20 Chi A, Chen H, Wen S, Yan H, Liao Z. Comparison of particle beam therapy and stereotactic body radiotherapy for early stage non-small cell lung cancer: A systematic review and hypothesis-generating meta-analysis. Radiotherapy and Oncology. 2017;123(3):346-354.
21 Liao ZX, Lee JJ, Komaki R, et al. Bayesian randomized trial comparing intensity modulated radiation therapy versus passively scattered proton therapy for locally advanced non-small cell lung cancer. In: American Society of Clinical Oncology; 2016.
22 Oborn BM, Dowdell S, Metcalfe PE, Crozier S, Mohan R, Keall PJ. Future of Medical Physics: Real-time MRI guided Proton Therapy. Medical physics. 2017.

Content

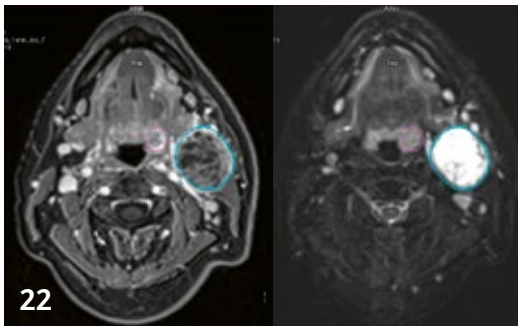

MR-simulation for radiotherapy treatment planning of head and neck cancer

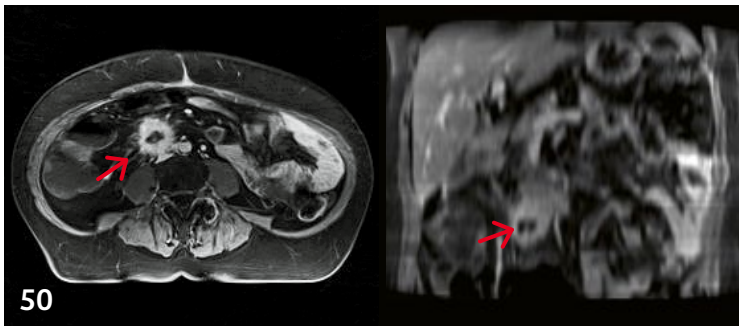

4D-MRI for abdominal radiotherapy planning

Editorial Comment

Radiation Therapy

Meet Siemens Healthineers

Replacement of a CT-simulator with an MRI-simulator within a radiation oncology department

Peter Greer; John Simpson; Joanna Ludbrook; Karen Jovanovic; Lynette Cassapi; Ashley Powell; Rochelle Greene; Mahesh Kumar

Radiation Oncology, Calvary Mater Newcastle, Newcastle, New South Wales, Australia

Department's experience with MRI

The Radiation Oncology Department of the Calvary Mater Newcastle is one of the largest clinical and academic departments providing public radiation therapy in New South Wales (NSW), Australia. The department has five linear accelerators with over 2,000 new patient referrals in 2016 and approximately 30,000 annual linear accelerator occasions of service. As a major centre in regional NSW, the department offers advanced radiation techniques to regional and rural patients with stereotactic cranial radiosurgery, stereotactic ablative body radiotherapy, and gynecological brachytherapy. In 2016 about 60% of patients received complex conformal treatments with either intensity modulated radiation therapy (IMRT) or volumetric modulated arc radiotherapy (VMAT). It is also one of three major centres in NSW identified as providing pediatric radiotherapy.

In 2011 a MAGNETOM Skyra 3T MRI system (Siemens Healthcare, Erlangen, Germany) was installed in the hospital radiology department. As part of this installation the radiation therapy equipment that was required to operate the scanner as an MRI-simulator was purchased and commissioned. This included an external laser bridge for patient positioning (LAP, Lüneburg, Germany), a flat indexed detachable couch top and pelvic and head and neck coil bridges (Civco, Orange City, IA, USA). Previous to

1

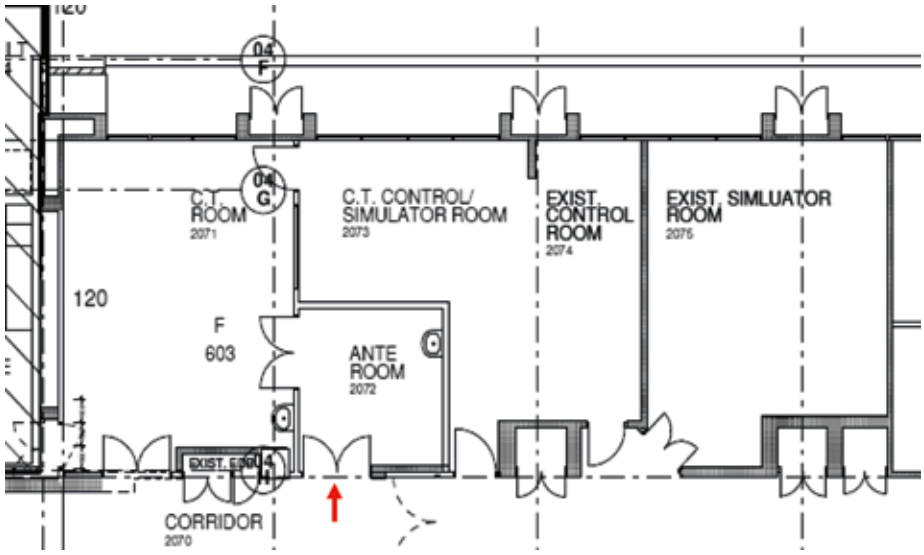

Figure 1: Existing configuration of two CT-simulators.

this, diagnostic radiology scans had been utilized for planning purposes. The availability of this scanner, albeit with limited access resulted in an increase in the use of MRI scanning for radiotherapy planning. The benefit of MRI scanning for many radiotherapy treatment sites quickly become apparent. Gynecological brachytherapy was transitioned to MRI only at that time. The department became one of the main drivers in Australia for the use of MRI simulation, MRI-only planning and clinical studies incorporating MRI.

Justification for a dedicated MRI-simulator

In spite of the benefits, restricted access to a busy radiology scanner meant that the department was limited to less than 10 patients per week for radiotherapy planning scans which were predominantly prostate, brain, cervix, spine and soft tissue tumors. Timely access to MRI scanning slots were by necessity limited as the radiology department must prioritize sessions for acutely unwell inpatients and routine diagnostic procedures. A further diasadvantage of utilizing a radiology MRI was that our patients were required to attend two separate imaging sessions (CT in radiation oncology department and MRI in radiology department) with time intervals of between 2 and 48 hours between them. This not only inconvenienced the patients and was disruptive to departmental workflows but the time interval between scans increased the possibility and magnitude of anatomical changes occurring between the two scans. In the majority of cases it was not possible to setup patients in the treatment position due to time and staff limitations. In addition access for the development of radiotherapy planning optimized scanning protocols or for research and development was very problematic.

The role of MRI in clinical radiation oncology and radiotherapy treatment planning is evolving and to adopt new and emerging practices it is necessary to have a level of control and access to MRI that requires it to be within the radiation oncology department.

It has been recognized that instead of the acquisition and registration of two separate imaging modalities CT and MRI, that an MRI-only process would have advantages to reduce costs, patient burden, and reduce registration induced systematic errors [1]. Methods to develop synthetic CT scans from MRI scans for MRI-only prostate planning have been developed [2]. Advances in the methods of synthetic CT generation and number of treatment sites is an active area of continued development.

MRI provides vastly superior soft-tissue contrast than CT for a large number of treatment sites including brain, head and neck, prostate, rectum, anal, pelvic sites, and gynecological treatments. This has been shown in multiple studies to reduce the inter-clinician variation in tumor delineation as well as to increase sparing of some normal tissues including the penile bulb for prostate cancer treatments. In addition to the the benefit of improved anatomical information from T1 and T2-weighted images, multiparametric MRI combining anatomical and functional MRI methods can increase the sensitivity and specificity of cancer detection and staging and also yield additional information about the cancer status, used to predict and monitor treatment response [3, 4]. This opens up the possibility of personalized treatment based on an individual's imaging profile for dose boosting or on-treatment response monitoring for treatment adaptation [5, 6]. There is also the prospect of improving imaging of tumor motion with MRI using both cine and 4D-MRI techniques that are currently under development.

Departmental MRI-simulator

In 2016 the decision was made to replace our two CT scanners due to their age. A multi-disciplinary working group was established comprising medical physicists, radiation therapists, radiation oncologists, a nurse, and a business manager. An initial recommendation was made to investigate if an MRI-simulator could replace one of the CT scanners. It was concluded that the installation of an MRI-simulator would meet the department's needs for MRI simulation by integrating the MRI within the department allowing improved access for patient scanning and development. A streamlined MRI simulation process would ensure that regional and rural patients would have timely and ready access to high-quality radiation treatment. In a single appointment a patient would undergo either an MRI simulation scan alone or both an MRI and CT scan. Our department felt that this recommendation was in concordence with the rapid increase in MRI utilization in radiation therapy as well as international recommendations. The recent Cancer Strategy 2015–2020 for England report that states "The greatest improvements in radiotherapy over the next decade will likely be driven by improvements in imaging technology" and their recommendation that "NHS England should support the provision of dedicated MRI and PET imaging facilities for radiotherapy planning in major treatment centres" [7].

MRI vendors were approached to assess if the space requirements were adequate for their MRI scanners given the current building construction and room space. All of the vendors approached confirmed that an MRI-simulator could be installed in the current space given some relatively minor modifications. This required engineering reports to determine which walls were load-bearing and could be modified and which could not. The room layout for the two existing CT-simulators is shown in Figure 1.

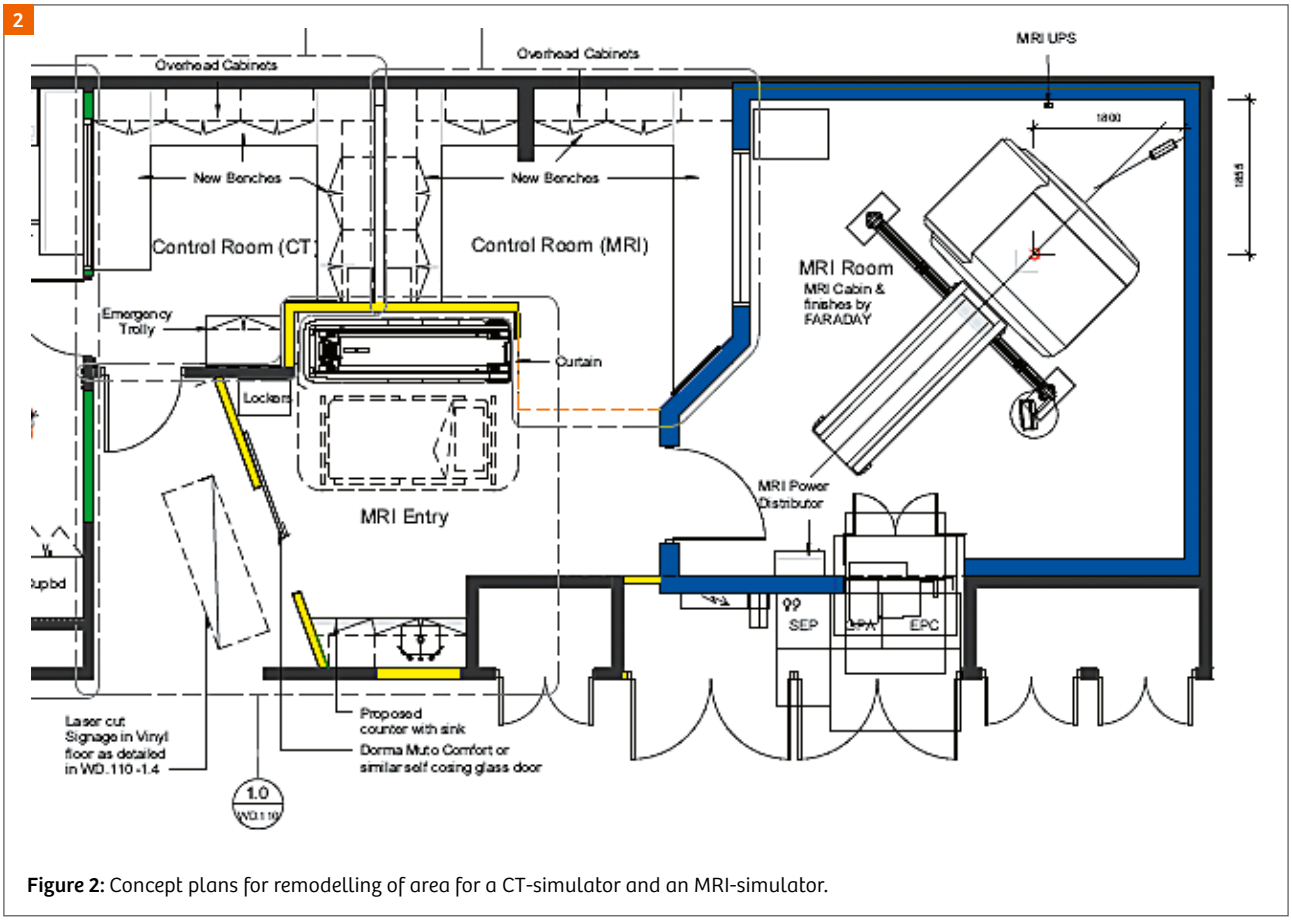

Figure 2: Concept plans for remodelling of area for a CT-simulator and an MRI-simulator.

While the two existing simulator rooms were relatively small, an advantage was the large control area that was shared by the two scanners and an ante room that was used for patient consults that gave some flexibility. However use of the space was restricted by existing load bearing walls, concrete cabinets housing supply infrastructure, and fire doors which could not be altered. This resulted in a single practical option for the placement of door access to the CT and MRI scanner control areas which has been shown with the arrow in Figure 1.

Following this, broader consultation was undertaken within the department where issues could be raised by staff and addressed by the working group. A major concern arising from moving to a single CT was addressed with a trial of a single CT to ensure that reduction in CT capacity could be managed.

Requirements

A technical specification (available on request) was made after consultation with other sites that had or were considering purchasing MRI-simulators. Site visits were also made to two existing centres with MRI-simulators.

With the implementation of a new MRI-simulator into the radiotherapy department where such equipment had not previously been housed the addition of specialist staffing was required. This included a dedicated MRI radiographer, MRI physicist, and part-time radiologist. These were included to ensure optimal MRI scanning and facilitate development and research into improved scanning techniques including MRI-only planning, functional (metabolic) scanning techniques for improved tumor visibility and assessment of treatment response, as well as scanning to measure tumor motion (4D-MRI) to ensure dose coverage of tumors. They are also critical to train other staff including radiation oncologists, radiation therapists, and medical physicists in MRI safety, technology, scanning, imaging features, and physics.

Concept plans

A plan was developed by Siemens Healthineers to enable the installation of the MRI-simulator in one of the CT-simulator rooms. Only minor structural modifications were necessary to the wall between the room and console area. For reasons of safety, the MRI suite is required to be in a controlled access environment.

The MRI suite design consisted of an MRI examination room, MRI control room, and prep room (Fig. 2). The design allows a single entry access to the MRI suite restricted to authorized personal via swipe card while allowing unhindered access to the CT console area. The suite provides an MRI preparation area including a patient change and transfer area. Access to the high magnetic field MRI-simulator room is via a second appropriately signed and secured door.

The project is being staged so that CT-simulator access is continuous. In the first stage the CT-simulator was replaced in Room 2071 (left) along with console area modifications. This allowed the second CT-simulator to continue clinically. Once this new scanner was operational the installation of the MRI-simulator commenced and it will be operational in April 2018.

Summary

Based on the clinical benefit of increased accuracy and taking a forward looking approach to our radiotherapy simulation needs, we have determined to replace a CT-simulator with an MRI-simulator. The inherent limitations of space and site configuration when adapting an existing area have been accommodated in the design. Ready access to, and control over the MRI-simulator will allow for the increased utilization of MRI in treatment planning, response monitoring and treatment adaptation.

References

1 Greer P, Dowling J, Lambert J, Fripp J, Parker, J, Denham J, et al. A magnetic resonance imaging-based workflow for planning radiation therapy for prostate cancer. Med. J. Aust. 2011;194:S24.
2 Dowling JA, Lambert J, Parker J, Salvado O, Fripp J, Capp A, et al. An atlas-based electron density mapping method for magnetic resonance imaging (MRI)-alone treatment planning and adaptive MRI-based prostate radiation therapy. Int. J. Radiat. Oncol. Biol. Phys. 2012;83:e5–11.
3 Akin O, Gultekin DH, Vargas HA et al. Incremental value of diffusion weighted and dynamic contrast enhanced MRI in the detection of locally recurrent prostate cancer after radiation treatment: preliminary results. European Radiology. 2011;21(9):1970-78.
4 Thoeny HC and Ross BD. Predicting and Monitoring Cancer Treatment Response with DW-MRI. J Magn Reson Imaging. 2010;32(1):2-16.
5 Padhani AR and Miles KA. Multiparametric Imaging of Tumor Response to Therapy. Radiology. 2010;256(2):348-64.
6 Kim Y, Tomé WA. Risk-adaptive optimization: selective boosting of high-risk tumor subvolumes. Int.J.Radiat.Oncol. Biol. Phys.2006;66:1528-1542.
7 https://www.england.nhs.uk/publication/achieving-world-class-cancer-outcomes/

Contact

Peter Greer
Principal Physicist
Calvary Mater Newcastle

Corner of Edith & Platt Streets
Waratah, NSW, 2298
Australia
Tel.: +61 2 4014 3689
peter.greer@newcastle.edu.au

MRI for prostate and gynecological brachytherapy is here to stay

Firas Mourtada, Ph.D.[1]; Daniel G. Petereit, M.D.[2]; Sushil Beriwall, M.D.[3]; Joann I. Prisciandaro, Ph.D.[4]

[1] Helen F. Graham Cancer Center & Research Institute, Christiana Care Health System, Newark, DE, USA
[2] Rapid City Regional Cancer Care Institute, Rapid City, SD, USA
[3] UPMC Hillman Cancer Center, Pittsburgh, PA, USA
[4] Department of Radiation Oncology, University of Michigan, Ann Arbor, MI, USA

Key points

In this article, we describe the status of MRI utilization[1] for both gynecological and prostate cancer radiotherapy treatments using HDR brachytherapy in the United States. The current clinical evidence has demonstrated MRI should be incorporated in the standard of care for all gynecological and prostate brachytherapy patients. However, unlike Europe, in the U.S. we continue to look for ways to adapt MRI within our constraints (initial costs and reimbursement), and to provide our patients the best MRI based approach to manage their disease effectively and safely. We share what we have learned from our collective experiences.

Introduction

Brachytherapy has a long history in cancer therapy, with its initial applications performed shortly after the discovery and isolation of radium from pitchblende by Pierre and Marie Curie in 1898. Two-dimensional radiographic films were used for treatment planning prior to the inception of 3D volumetric imaging in the 1970s. In particular, computed tomography (CT) and transrectal ultrasound (TRUS) were first implemented for several disease sites. More recently, magnetic resonance imaging (MRI) has demonstrated superior soft tissue contrast and spatial resolution, a clear advantage for accurate treatment planning using brachytherapy sources. Over the last few years, the use of MRI for patient selection and treatment planning has gained significant momentum with growing clinical experience. In the United States, MRI utilization for cervical cancers has increased from 2% in 2007 to 34% in 2014 [1]. MRI is superior to ultrasound and CT for visualizing intra-prostatic tumors and evaluating macroscopic extracapsular extension and/or seminal vesicle invasion that would preclude brachytherapy as a monotherapy option. In 2012, the American Brachytherapy Society (ABS) developed guidelines to use MRI for disease staging and treatment planning in “clinically relevant circumstances” by “experienced teams” [2]. In 2017 The American Association of Physicists in Medicine (AAPM) approved the formation of Task Group 303 – MRI Guidance

[1] The product is not commercially available. Radiotherapy where MR data is the only imaging information is ongoing research. The concepts and information presented in this article are based on research and are not commercially available. Its future availability cannot be ensured. Not for clinical use.

Figure 1:
(1A) MAGNETOM Aera (1.5T) Tim Dockable table at the Christiana Care Health System community hospital, Newark, DE, USA.

(1B) Wide-bore MAGNETOM Skyra (3T) MRI with the Tim Dockable table at the University of Michigan, Ann Arbor, MI, USA.

in HDR Brachytherapy – Considerations from Simulation to Treatment – in response to the growing interest in MRI guided brachytherapy. The committee consists of brachytherapy physicists and clinicians from academic and community cancer centers, as well as MRI industry representatives. These experts have been charged with developing recommendations and guidelines for the commissioning, clinical implementation, and on-going quality assurance specifically for MRI-based prostate and gynecological HDR brachytherapy. Herein we present on key evidence to support the statement that MRI is here to stay for brachytherapy.

MRI future for prostate cancer brachytherapy

A special issue in the *Brachytherapy Journal* was recently published on the treatment of prostate cancer, including several pivotal articles on the use of MRI in the diagnosis, treatment, response assessment, and "the management of recurrent disease in the setting of rising prostate-specific antigen levels after low-dose-rate (LDR) or high-dose-rate (HDR) brachytherapy" [3]. The goal of the issue was to "bend the brachytherapy curve" by optimizing the therapeutic ratio through the utilization of MRI [3]. To highlight a few articles, Venkatesan *et al.* presented an overview of multi-parametric MRI (mp-MRI) techniques for high-resolution of prostate anatomy. They discussed the pros and cons of using an endorectal coil (ERC) with emerging evidence that it may not be necessary when using a 3T MRI [4]. In a second paper from Venkatesan *et al.*, they summarized prostate cancer findings, tumor staging, and presented an overview of the Prostate Imaging Reporting and Data System (PIRADS). In addition, they presented MRI findings observed in the post-therapy setting, including sites of recurrence, and MRI concepts pertinent to successful salvage brachytherapy [5]. Pugh and Pokharel reviewed MRI utilization in prostate brachytherapy and postulated future pathways for MRI integration. They detailed several advantages of MRI integration including "superior intra-prostatic soft tissue resolution, localization of the dominant intra-prostatic lesion, and improved anatomic visualization of the prostate apex, prostate-bladder interface, prostate-rectal interface, neurovascular bundles, and genitourinary diaphragm" [6].

LDR and HDR brachytherapy using TRUS or CT are commonly used in practice today. However, while the therapeutic ratio is largely favorable, ongoing dilemmas include 'cold' base and 'hot' spots in the apex, urethral strictures, bladder dysfunction, erectile dysfunction, and biochemical recurrences. The Androgen Suppression Combined with Elective Nodal and Dose Escalated Radiation Therapy (ASCENDE-RT) trial demonstrated an unequivocal improvement in biochemical control rates for intermediate to high risk patients treated with an LDR prostate brachytherapy boost, but with grade 3 late GU toxicities of 18.4% – half of which were urethral strictures, many of which resolved over time with a prevalence rate of 8.6% at five years [7].

MRI future for gynecological cancers brachytherapy

For gynecological cancer, the International Commission of Radiation Units and Measurements (ICRU) has recently updated their classical 1985 report 38 [8] with ICRU report 89 [9]. The updated report provides an excellent description of current volumetric imaging (MRI and CT) for the cervix with the addition of 4D adaptive target concepts and updated radiobiology and recommended dose volume histogram (DVH) parameters for target and organs-at-risk (OAR) [9]. Some of the ICRU updated guidelines were based on the Groupe Européen de Curie thérapie – European Society for Radiotherapy & Oncology (GEC-ESTRO) recommendations. GEC-ESTRO has taken the lead and recognized volumetric imaging for brachytherapy treatment planning for cervical cancer, with the formation of the gynecological (GYN) GEC-ESTRO work group. Over the last 18 years their work group has published a series of recommendations to assist in the standardization of image-based brachytherapy treatment planning. This has included the definition of a common language and means of delineating the target volumes (i.e., Intermediate Risk-CTV and High Risk-CTV for the definitive treatment of cervical cancer), discussions on issues related to applicator reconstruction, and suggestions on the appropriate MR imaging sequences utilized for treatment planning [10–13]. The outcome data with MRI-based planning is excellent in limited and well responding tumors demonstrating improved local control and decrease morbidities in comparison to historical 2D planning methods as demonstrated by the completed EMBRACE I (An Int**E**rnational study on **M**RI-guided **BR**achytherapy in locally **A**dvanced **CE**rvical cancer) multicenter protocol [14]. Key findings include an improvement in local control by 10% when comparing limited to advanced image based brachytherapy planning for large tumors (three year local failures rates of 2%, 7–9%, 21–25% for stages IB, IIB, IIIB, respectively), and ongoing, detailed quality of life analysis of vaginal, bladder, and bowel morbidity [15, 16]. The late rectal morbidity appears to be lower when D2cc ≤ 65 Gy versus ≥ 75 Gy, even though the HR CTV is dose escalated with Image Guided Advanced Brachytherapy (IGABT) [17]. Based on the positive outcomes from the RetroEMBRACE and EMBRACE I protocols, the EMBRACE research group has initiated the EMBRACE II protocol with the intention of using state of the art treatment techniques for external beam

and brachytherapy to enhance local, nodal, and systemic control while minimizing normal tissue toxicity [17].

How to navigate challenges transitioning to MRI-based brachytherapy

Often, we have the preconceived notion that MRI-based brachytherapy is resource intensive. Harkenrider *et al.* recently described their experience with transitioning from CT-based to MRI-based brachytherapy for cervical cancer at Loyola University Medical Center, Maywood, IL, USA) [18]. They suggest that the key to success is a multidisciplinary team approach involving radiation oncology, gynecologic oncology, radiology, and anesthesia. Once the 'big picture' was identified (e.g., MR applicator choice, dose fractionation schedule), they optimized their workflow to best suit their clinic [18].

MRI utilization for brachytherapy can be considered in three fundamental categories: pre-planning target diagnosis; implant guidance; MR-based treatment planning after implant insertion; and MRI-guided implant insertion and treatment planning. With this in mind, the basic requirements for the successful implementation of MRI in brachytherapy include:

1. Access to an MRI scanner (e.g., a diagnostic or dedicated radiation oncology simulator),
2. MR conditional ancillary equipment (e.g., leg straps, immobilization devices, transport table), and
3. an optimized clinical workflow, which involved input from all members of the multidisciplinary team involved in the patient's care.

Additionally, when integrating MR into brachytherapy, it is imperative to review and update the clinical workflow initially and on a periodic basis as your program matures. Considerations for MRI safety must also be a priority for a successful program with ongoing staff training to ensure patient and hardware safety.

At each of our four respective institutions, MRI has been utilized in the care of brachytherapy patients. Our departments are equipped with either the Siemens Healthineers MAGNETOM Aera (1.5T) or MAGNETOM Skyra (3T) MRI scanners (Figures 1A and 1B, respectively). Additionally, to minimize patient motion between planning simulation and treatment, MR-conditional transport systems, such as the Siemens Healthineers Tim Dockable table (Fig. 1C) and the Symphony™ (Qfix, Avondale, PA, USA) patient transport system[2], are being utilized (Fig. 2). However, each

[2] The information shown herein refers to products of 3rd party manufacturer's and thus are in their regulatory responsibility. Please contact the 3rd party manufacturer for further information.

Figure 1C:
The Tim Dockable table detached from the Siemens Healthineers MRI simulator.

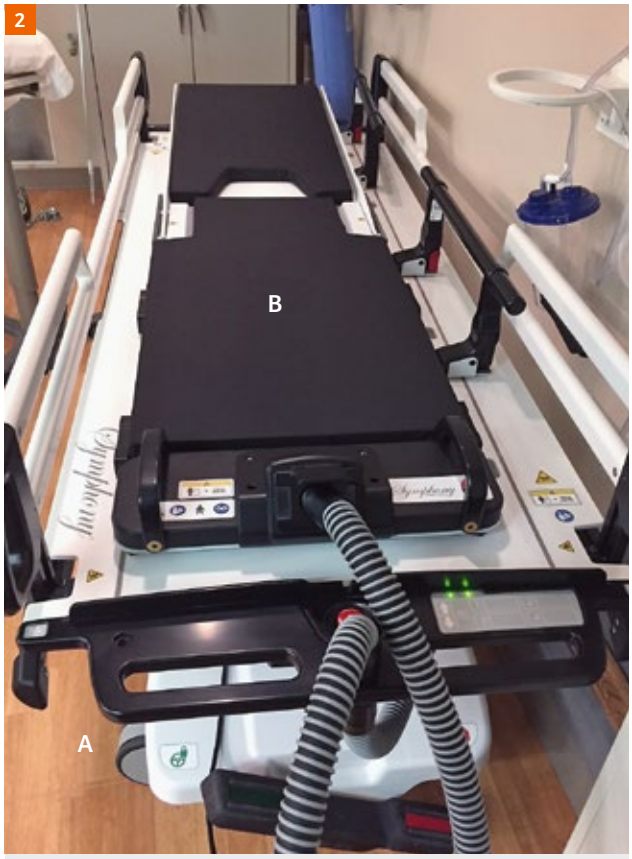

Figure 2:
Example of a patient transport system (Symphony Patient Transport System, Qfix, Avondale, PA, USA) that can easily move the patient from our Siemens Healthineers Tim Dockable table for the MAGNETOM Aera 1.5T scanner with minimal motion of applicator or needles. **(A)** Symphony patient trolley-integrated air pump, two batteries, and adjustable pillars. **(B)** Symphony Brachytherapy Transfer Device and leg extension. All devices are MR Conditional.

institutions approach to MR guided brachytherapy differs based on our resources, time, and financial constraints.

At one community-based cancer center (Helen F. Graham Cancer Center, Newark, DE, USA), for cervical cancer patients, applicator (plastic only) insertion is performed in a prep room that has OR lights and MR safe anesthesia equipment, adjacent to the MR scanner in our Radiology department. In the case of interstitial implants, diagnostic MR images are made available at the time of implant to assist in guiding needle/catheter placement. In general, the procedure starts with the patient lying supine on the Symphony patient trolley and Symphony Brachytherapy Transfer Device (Fig. 2). Once applicator insertion is complete using non-MR compatible stirrups, the patient is transferred onto the Siemens Healthineers Tim Dockable MR table. The patient is then transferred to the MAGNETOM Aera MRI scanner (Fig. 1A), and the 18-channel body coil (attached to Qfix Insight MR Bridge with Body Coil holder) is positioned about 1 cm above the patient's pelvis. MR scout images are taken (sagittal and coronal) to allow the physician to review the applicator placement quality, and if needed, make minor adjustments in the MR vault prior to the acquisition of the final T1- and T2-weighted 3D SPACE image protocols (< 10 min). Once the MR scans are complete, the patient is transferred back to the Symphony patient trolley and taken back to the HDR vault in Radiation Oncology. For MR-based treatment planning, the high risk clinical target volume (HR-CTV) and the organs at risk (OARs) are delineated on the T2-weighted 3D SPACE MRI dataset. MR-based planning is only performed for the first treatment fraction and MR/CT rigid registration tools available in Raystation v 5.0 (Raysearch Labs, Stockholm, Sweden) are used for subsequent HDR fractions planned on CT images (Fig. 3). This rigid registration relies on the Smit Sleeve location (not bony anatomy). The Smit Sleeve is clearly visible on both MR and CT and is reliable to map the MR HR-CTV onto the subsequent fraction CT. The physician can then modify the registered HR-CTV on the CT if needed. For HDR treatment planning, *solid applicator* models provided by the Oncentra planning system (Elekta Inc., Stockholm, Sweden) (Fig. 4) are used to align the applicator on MR or CT images. Based on our commissioning data, the applicator model can map the first dwell position of the source within an uncertainty of 2 mm. The OARs are contoured on CT for each fraction since CT (with contrast) is fairly accurate to contour the bladder and rectum. This workflow has been found to be efficient since the procedure starts at the MR station, saving time for patient transfer under anesthesia. The entire process, applicator insertion, MR imaging, and the HDR fraction delivery is typically completed within 90 minutes.

At an academic institution (University of Michigan), the extent to which we have adopted MRI-based brachytherapy varies based on treatment site and applicator. For all treatment sites, applicator insertion is performed either in a dedicated HDR suite or in an operating room. In the case of interstitial implants, diagnostic MR images are made available at the time of implant to assist in guiding needle/catheter placement. For gynecological cancers requiring cylindrical applicators (e.g., for the treatment of post-hysterectomy endometrial cancer), patients undergo MR (Fig. 1B) only planning simulations and a T1-weighted (VIBE) coronal image is

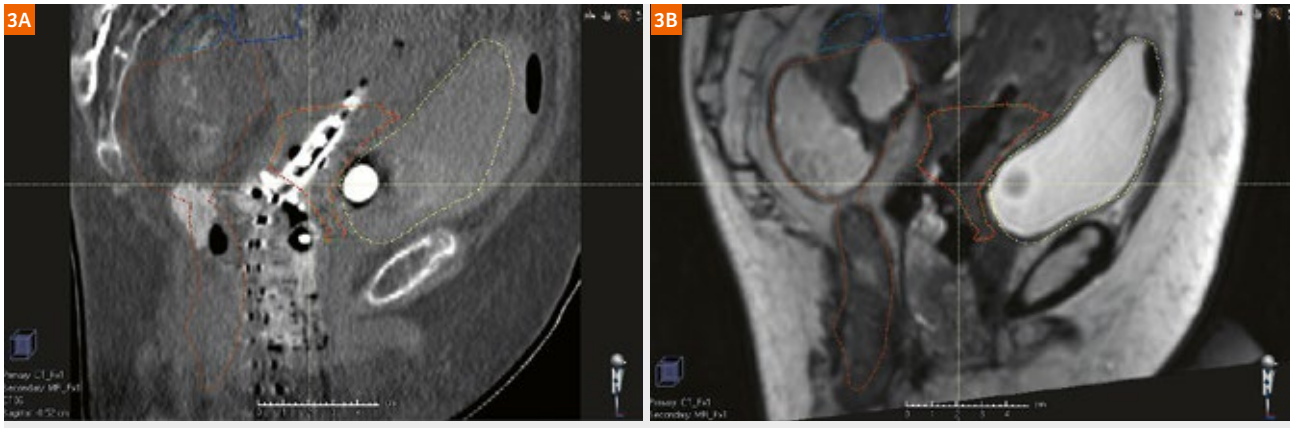

Figure 3:
HR-CTV target (red dotted line) defined following rigid registration in Raystation planning system, using the Smith Sleeve for a tandem and ring gynecological case of a sixty-year-old patient with stage IV cervical cancer **(3A)** clinical standard CT pelvis protocol (Siemens Healthineers SOMATOM Sensation Open) vs. **(3B)** T2w 3D SPACE AX ISO 1.3 mm^3 isotropic MRI (1.5T) MAGNETOM Aera. Coils used: Spine array coil in the Tim Dockable table and the 18-channel Body Matrix coil attached to the Qfix Insight MR Bridge with Body Coil holder. 3D distortion correction is turned on.

used for treatment planning [19]. To expedite planning, an applicator model is overlaid on the outline of the applicator as visualized on the MR images (i.e., observed as a signal void) (Fig. 5). In the case of patient's treated with a ring and tandem applicator (e.g., for cervical cancer), we are still in transition to MR only planning simulations, following the purchase of new plastic brachytherapy applicators. At present, both CT and MR simulations are acquired for each treatment fraction, and rigidly registered. The HR-CTV is delineated on a T2-weighted MRI dataset, and the contour is then copied to the CT scan. Treatment plans are generated using the CT planning simulation. In the future, we intend to transition to MR-only planning simulations, and in an attempt to reduce planning time (i.e., for subsequent treatment fractions), use deformable image registration to automate the contouring of the HR CTV and OARs [20]. For advanced gynecological cancers requiring an interstitial implant, both CT and MR planning simulations are acquired. The HR CTV is defined on a T2-weighted MRI and copied to the rigidly registered CT dataset for treatment planning. Lastly, in the case of prostate HDR brachytherapy, which is restarting following a three-year hiatus, the initial intent is to have diagnostic MR images available at the time of the US guided procedure to assist with dose escalation to intraprostatic lesions.

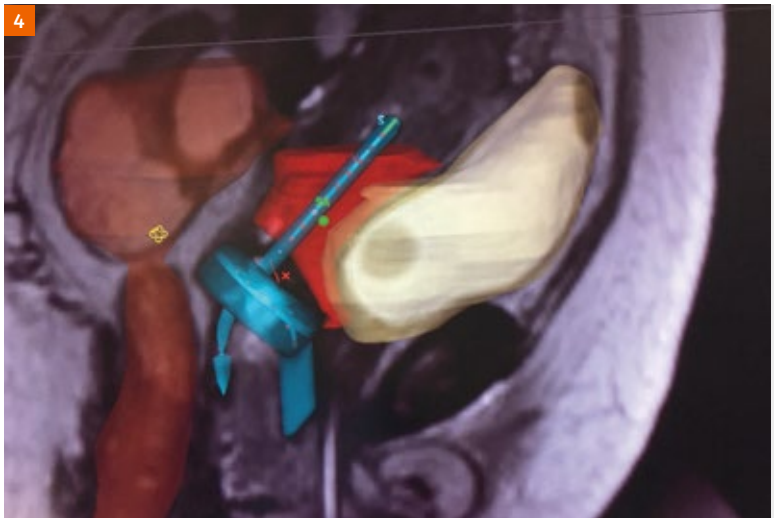

Figure 4:
In Oncentra HDR treatment planning system, the tandem and ring *solid applicator* model is accurately registered (within 2 mm uncertainty) to the 3D MR images of patient anatomy shown Figure 3. Images obtained using T2w 3D SPACE AX ISO 1.3 mm^3 isotropic MRI (1.5T) MAGNETOM Aera with spine array coil and 18-channel body coils, and 3D distortion correction is turned on.

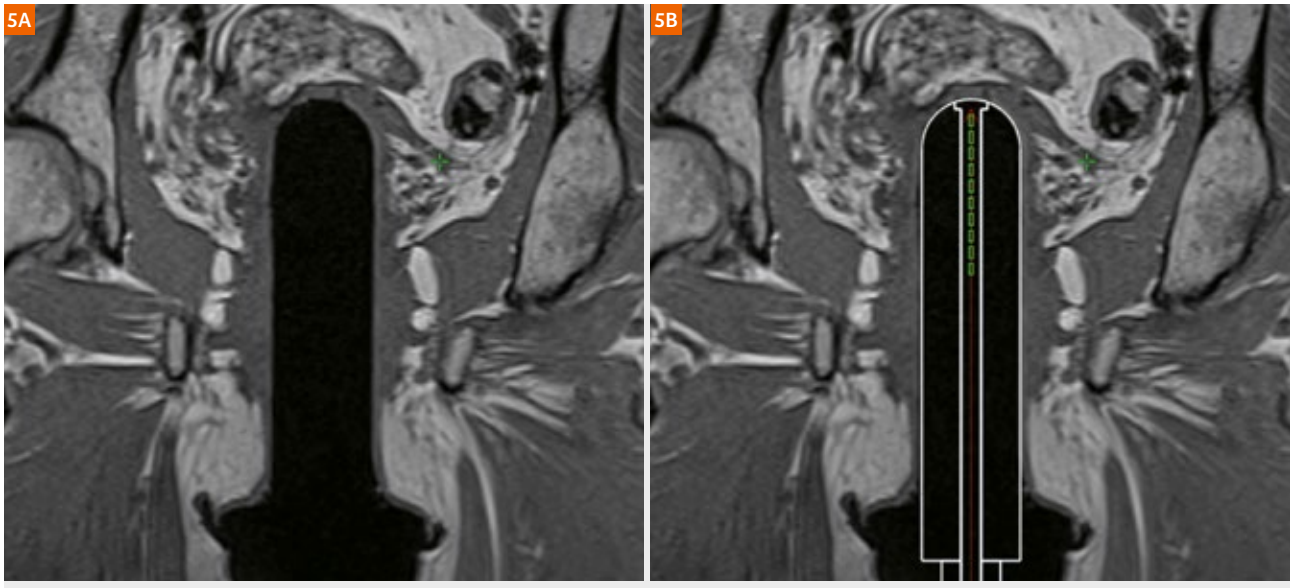

Figure 5:
(5A) Paracoronal 3D T1-weighted (VIBE) MRI of a patient with a plastic MR conditional vaginal cylinder in place. **(5B)** Alignment of the applicator model over the signal void representing the perimeter of the applicator for treatment planning purposes.

Conclusions

MR guided brachytherapy has strong supporting evidence that it will further improve the therapeutic ratio for prostate and gynecologic malignancies, and is feasible to implement in established brachytherapy practices. We believe more radiation oncology centers will and should begin implementing MR into their brachytherapy procedures. We look forward to seeing the future publication of the AAPM TG-303 report for further recommendations to aid brachytherapists in the expansion of MRI utilization in the United States for brachytherapy.

References

1 Grover S, H.M., Cho LP, Erickson B, Small C, Small W Jr, Viswanathan AN, Image Guided Cervical Brachytherapy: 2014 Survey of the American Brachytherapy Society. International Journal of Radiation Oncology Biology Physics, 2016. 94(3): p. 598-604.
2 Viswanathan, A.N., et al., American Brachytherapy Society consensus guidelines for locally advanced carcinoma of the cervix. Part II: high-dose-rate brachytherapy. Brachytherapy, 2012. 11(1): p. 47-52.
3 Frank, S.J. and F. Mourtada, Bending the slope of the brachytherapy curve: Magnetic resonance imaging-assisted radiosurgery for the treatment of prostate cancer. Brachytherapy, 2017. 16(4): p. 657-658.
4 Venkatesan, A.M., et al., Prostate magnetic resonance imaging for brachytherapists: Diagnosis, imaging pitfalls, and post-therapy assessment. Brachytherapy, 2017. 16(4): p. 688-697.
5 Venkatesan, A.M., et al., Prostate magnetic resonance imaging for brachytherapists: Anatomy and technique. Brachytherapy, 2017. 16(4): p. 679-687.
6 Pugh, T.J. and S.S. Pokharel, Magnetic resonance imaging in prostate brachytherapy: Evidence, clinical end points to data, and direction forward. Brachytherapy, 2017. 16(4): p. 659-664.
7 Rodda S, T.S., Morris J, Keyes M, Halperin R, Pai H, McKenzie M, Duncan G, Morton, G, Hamm J, Murray N, ASCENDE-RT: An Analysis of Treatment-Related Morbidity for a Randomized Trial Comparing a Low-Dose-Rate Brachytherapy Boost with a Dose-Escalated External Beam Boost for High- and Intermediate-Risk Prostate Cancer International Journal of Radiation Oncology Biology Physics, 2017. 98(2): p. 286-295.
8 ICRU Report No. 38, Dose and Volume Specification for Reporting Intracavitary Therapy in Gynecology. 1985, International Commission of Radiation Units and Measurements.
9 ICRU Report No. 89, Prescribing, Recording, and Reporting Brachytherapy for Cancer of the Cervix. Journal of the ICRU, 2013. 13(1).
10 Haie-Meder, C., et al., Recommendations from Gynaecological (GYN) GEC-ESTRO Working Group (I): concepts and terms in 3D image based 3D treatment planning in cervix cancer brachytherapy with emphasis on MRI assessment of GTV and CTV. Radiother Oncol, 2005. 74(3): p. 235-45.
11 Potter, R., et al., Recommendations from gynaecological (GYN) GEC ESTRO working group (II): concepts and terms in 3D image-based treatment planning in cervix cancer brachytherapy-3D dose volume parameters and aspects of 3D image-based anatomy, radiation physics, radiobiology. Radiother Oncol, 2006. 78(1): p. 67-77.
12 Hellebust, T.P., et al., Recommendations from Gynaecological (GYN) GEC-ESTRO Working Group: considerations and pitfalls in commissioning and applicator reconstruction in 3D image-based treatment planning of cervix cancer brachytherapy. Radiother Oncol, 2010. 96(2): p. 153-60.
13 Dimopoulos, J.C., et al., Recommendations from Gynaecological (GYN) GEC-ESTRO Working Group (IV): Basic principles and parameters for MR imaging within the frame of image based adaptive cervix cancer brachytherapy. Radiother Oncol, 2012. 103(1): p. 113-22.
14 Potter, R., et al., The EMBRACE II study: The outcome and prospect of two decades of evolution within the GEC-ESTRO GYN working group and the EMBRACE studies. Clinical & Translational Radiation Oncology, 2018. In Press.
15 Sturdza, A., et al., Image guided brachytherapy in locally advanced cervical cancer: Improved pelvic control and survival in RetroEMBRACE, a multicenter cohort study. Radiother Oncol, 2016. 120(3): p. 428-433.
16 Fokdal, L., et al., Image guided adaptive brachytherapy with combined intracavitary and interstitial technique improves the therapeutic ratio in locally advanced cervical cancer: Analysis from the retroEMBRACE study. Radiother Oncol, 2016. 120(3): p. 434-440.
17 Mazeron, R., et al., Dose-volume effect relationships for late rectal morbidity in patients treated with chemoradiation and MRI-guided adaptive brachytherapy for locally advanced cervical cancer: Results from the prospective multicenter EMBRACE study. Radiother Oncol, 2016. 120(3): p. 412-419.
18 Harkenrider, M.M., et al., How one institution overcame the challenges to start an MRI-based brachytherapy program for cervical cancer. J Contemp Brachytherapy, 2017. 9(2): p. 177-186.
19 Owrangi, A.M., et al., Clinical implementation of MR-guided vaginal cylinder brachytherapy. J Appl Clin Med Phys, 2015. 16(6): p. 490-500.
20 Chapman, C.H., et al., Deformable image registration-based contour propagation yields clinically acceptable plans for MRI-based cervical cancer brachytherapy planning. Brachytherapy, 2018. In Press.

Joann I. Prisciandaro, Ph.D.

Sushil Beriwall, M.D.

Daniel G. Petereit, M.D.

Firas Mourtada, Ph.D.

Contact

Firas Mourtada, Ph.D.
Chief of Clinical Physics
Radiation Oncology, Ste 1152
Helen F. Graham Cancer Center & Research Institute
4701 Ogletown-Stanton Rd
Christiana Care Health System
Newark, DE 19713, USA
Tel: +1 302-623-4691
Fax: +1 302-623-4547
fmourtada@christianacare.org

MR-only guided proton therapy: advances, future perspectives and challenges

S.E.M. Huijsse[1]; A. Knopf[2]; L.V. van Dijk[2]; S. Both[2]; R.A.J.O. Dierckx[3]; R.J.H. Borra[1,3]

[1] Department of Radiology, University Medical Center Groningen, University of Groningen, Groningen, The Netherlands
[2] Department of Radiation Oncology, University Medical Center Groningen, University of Groningen, Groningen, The Netherlands
[3] Department of Nuclear Medicine and Molecular Imaging, University Medical Center Groningen, University of Groningen, Groningen, The Netherlands

Introduction

At the end of January 2018, proton therapy was introduced at the University Medical Center Groningen (UMCG). The Groningen Proton Therapy Center (GPTC) is one of approximately 60 proton therapy centers in operation worldwide. Over the last decade, the number of proton therapy centers has been constantly increasing. Proton therapy allows for radiation of tumor tissue with high precision, while minimizing normal tissue damage. This is due to the intrinsic physical properties of protons that allow for decrease of radiation dose issued to tissue surrounding the target volumes compared to conventional photon therapy [1, 2]. However, to fully utilize the benefit of protons, very accurate identification of tumor location is required. The advantage of highly conformal dose distributions in proton therapy may be compromised by spatial distortions, as they increase the range uncertainty of the proton beam. Due to the energy deposition of protons with steep dose gradients, accurate positioning of these gradients is critical to successful treatment planning and treatment delivery [1]. Geometric errors and uncertainties in Computed Tomography (CT) and Magnetic Resonance (MR) images can have a significant dosimetric impact, especially when the radiation is targeted to a small volume or a volume close to organs at risk [3]. In other words, small uncertainties (e.g. a few millimeters) can lead to underdosage in the target volume and overdosage to healthy surrounding tissue [1, 4].

Radiotherapy treatment planning is conventionally guided by single energy CT images, for tumor delineation and radiation dose calculation. Radiation dose calculation is performed on CT, mainly because the CT intensity values (Hounsfield Units (HU)) give a reliable representation of the electron densities in tissue. However, CT imaging is sub-optimal for precise and reliable tumor localization due to its limited soft-tissue contrast [5]. MR images offer better soft-tissue contrast and are therefore often additionally acquired to supplement CT images in order to improve tumor delineation [5–7]. For treatment planning purposes, the CT and MR images have to be mapped by rigid registration which includes registration uncertainties. In conventional MR sequences there is an absence of signal from cortical bone. Because of this, and due to the inherent difference of contrast, registration of CT and MR images is difficult [3]. Additionally, the image registration might be challenged by geometric distortions, artifacts, varying patient setups and varying anatomy appearance. Furthermore, the acquisition of images from two different modalities per patient implies disadvantages due to increased costs, patient discomfort and increased workload for clinicians [8].

Another major disadvantage of the current workflow is that CT employs ionizing radiation. For most patients CT scans will be repeated weekly (or even daily) to allow for inter-fractional guidance and treatment adaption [9]. The use of CT in pediatric patients should be avoided, as the additional ionizing radiation may pose a significant risk for future development of secondary malignancies. Dismissing CT from the radiotherapy planning workflow will thus reduce radiation dose, which is also in accordance with the principle of keeping radiation dose to patients (and personnel) As Low As Reasonably Achievable (ALARA) [10].

In the treatment phase the total external dose is usually divided into several smaller doses, called fractions, to spare healthy tissue as much as possible. Compared to photon therapy, proton therapy is expected to be able to decrease radiation dose to healthy tissue even further as dose beyond the target is zero [11] or almost zero [12, 13]. Proton therapy therefore may prevent or reduce radiation induced side effects [14, 15]. Dismissing CT for image guidance in a proton therapy workflow is thus expected to be able to maximize the dose reduction to healthy tissue, preventing or highly reducing radiation induced side effects throughout the entire workflow (e.g. planning phase and treatment phase).

Due to the described limitations in the current multi-modality workflow and due to limitations of CT imaging,

there is an increased interest in developing an MR-only[1] radiotherapy treatment planning workflow. The growing enthusiasm of MR-only planning is further strengthened by the worldwide development of MR-LINAC accelerators[2] [16, 17]. Similar combined MR-proton therapy (MR-PT) machines are foreseen to be developed in the future. Adjustment of the workflow using MRI alone does prevent irradiation of healthy tissue for treatment planning purposes. Therefore, imaging can be repeated as often as necessary. An MR-only workflow allows for practically unlimited interfractional evaluations and adaptations of the proton therapy planning addressing uncertainties due to changes in the anatomy. It is also beneficial for the patient in terms of logistics, since only one imaging modality is required instead of two. Here we provide an overview of novel techniques that will allow for accurate (real-time) MR-only image guided proton therapy in the nearby future.

Synthetic-CT image guidance

Current status

For radiotherapy treatment planning tissue electron density information is required. In contrast to CT, no direct relationship exists between MR image intensity values and electron density values [18]. This is due to the lack of correspondence between the voxel intensity and the associated attenuation properties of the tissue in MRI [3]. This means that a method has to be available for an MRI-only workflow that is able to derive CT equivalent information from MR data.

To enable MR-only radiation treatment planning, the MR data has to be converted into maps relevant for radiotherapy planning [3]. The generated maps are generally referred to as "synthetic CT" [3], "substitute CT" [19], or "pseudo CT" [20]. In the following paragraphs the term "synthetic CT" will be used.

For the generation of synthetic CTs, several approaches can be used: voxel-based techniques, single or multi-atlas-based techniques, and hybrid techniques combining atlas- and voxel-based techniques. In the voxel-based technique the concept of machine learning is used, in which a model is trained to predict CT numbers from MRI data [3, 21]. The CT number assignment can be done on the basis of generic values to bulk groups of voxels [3, 22, 23], or by including patient-specific CT numbers in a training phase [3]. For atlas-based approaches, first a reference dataset or atlas has to be generated based on co-registered CT and MR scans of an indication-specific patient group. For a new patient, with only an MR scan available, the location of MRI voxels can then be aligned to the location of MRI voxels in the atlas by registration. The resulting transformation is then applied to the atlas CTs to generate a synthetic CT image [3, 16]. In a hybrid approach two probability density functions (PDFs) can be calculated, for example; one based on the outcome of the atlas approach and one based on the outcome of the voxel-based approach [3]. The PDFs for each voxel can then be combined to determine the electron density value [16, 24]. Voxel-based techniques have the advantage of being able to handle patients with atypical anatomy, since they are not being reliant on an atlas [16]. Atlas based techniques, however, provide more accurate bone matches and heterogeneous HU patterns for different anatomical structures, more closely resembling real CT images [25].

Future vision

A study by Nyholm et al. [26] has shown that in prostate cancer patients systematic uncertainties can be reduced from 3–4 mm for a CT & MR workflow to 2–3 mm for an MR-only workflow, where the main contributing factor to uncertainty was the co-registration of CT with MR data. In general, the registration uncertainty introduced by registration is estimated to be in the range of 0.5 to 3.5 mm for the prostate and the brain [22, 26, 27]. As mentioned in the introduction, proton therapy is highly sensitive to spatial distortions. Voxel-based conversion of MRI data to electron density data avoids the geometric uncertainty introduced by deformable registration as used in atlas-based techniques [28].

In proton therapy the range of protons is determined from the stopping power ratio (SPR) of tissue relative to water. Calculation of electron densities from conventional single energy CT images results in an uncertainty in the SPR [29]. This is due to the degeneracy between CT numbers and SPRs, making the estimation of the SPR susceptible to variations in human tissue [30]. Recent publications have shown promising results of proton beam range calculation uncertainties with dual energy CT (DECT) to be in the order of 1% [31–33]. Therefore, it is expected that applying a voxel-based synthetic CT method on DECT data will result in less uncertainties in proton beam range calculation as compared to the conventional single energy CT based workflow.

In Figure 1 an MR-only synthetic CT approach is illustrated, where a voxel-based or hybrid technique is used to generate the synthetic CT images. In this approach, a machine learning algorithm is trained by DECT and MRI data, to predict CT values. The aim is to obtain synthetic CT data suitable for proton beam calculations purposes.

[1] The product is not commercially available. Radiotherapy where MR data is the only imaging information is ongoing research. The concepts and information presented in this article are based on research and are not commercially available. Its future availability cannot be ensured. Not for clinical use.

[2] The information shown herein refers to products of 3rd party manufacturer's and thus are in their regulatory responsibility. Please contact the 3rd party manufacturer for further information.

For the foreseen MR-only workflow depicted in Figure 1, MR sequences should be used that allow for bone identification to minimize uncertainties due to registration processes. Automatic voxel-based methods generally require ultra-short echo time (UTE) MR sequences [34]. One of the MR protocols that is used by Siemens Healthineers for generation of synthetic CT images is the pointwise encoding time reduction with radial acquisition (PETRA). This is a type of UTE imaging [16]. This sequence allows for fast imaging, by using Cartesian acquisition for only a few percent of the total acquisition time and radial acquisition for the remaining acquisition time [35]. This enables visualization of tissues with (ultra)short transverse relaxation times such as bone [36]. Post-processed PETRA images have been shown to have sufficient power to discriminate air from bone for the purpose of defining air masks and supporting the generation of synthetic CT from MRI data [37]. A disadvantage of a voxel-based approach is the prolonged acquisition time when multiple sequences are used, increasing the likelihood for artefacts generated by patient motion [16]. Therefore, measures should be taken to minimize patient motion during the entire acquisition.

MR-based proton therapy planning and real-time imaging guided proton therapy

In recent years, it has been shown that for photon treatment planning absorbed dose can be accurately computed based on synthetic CT data, and that these images can also be applied as reference images for image-guided radiotherapy (IGRT) [38–40]. Recently, the first studies investigating the use of synthetic CT for proton therapy planning have also been published [41, 42]. They focus on evaluating the dose calculation accuracy for robustly optimized intensity modulated proton therapy (IMPT) when recalculated on synthetic CTs, derived via different methods. So far, these studies are limited to

1

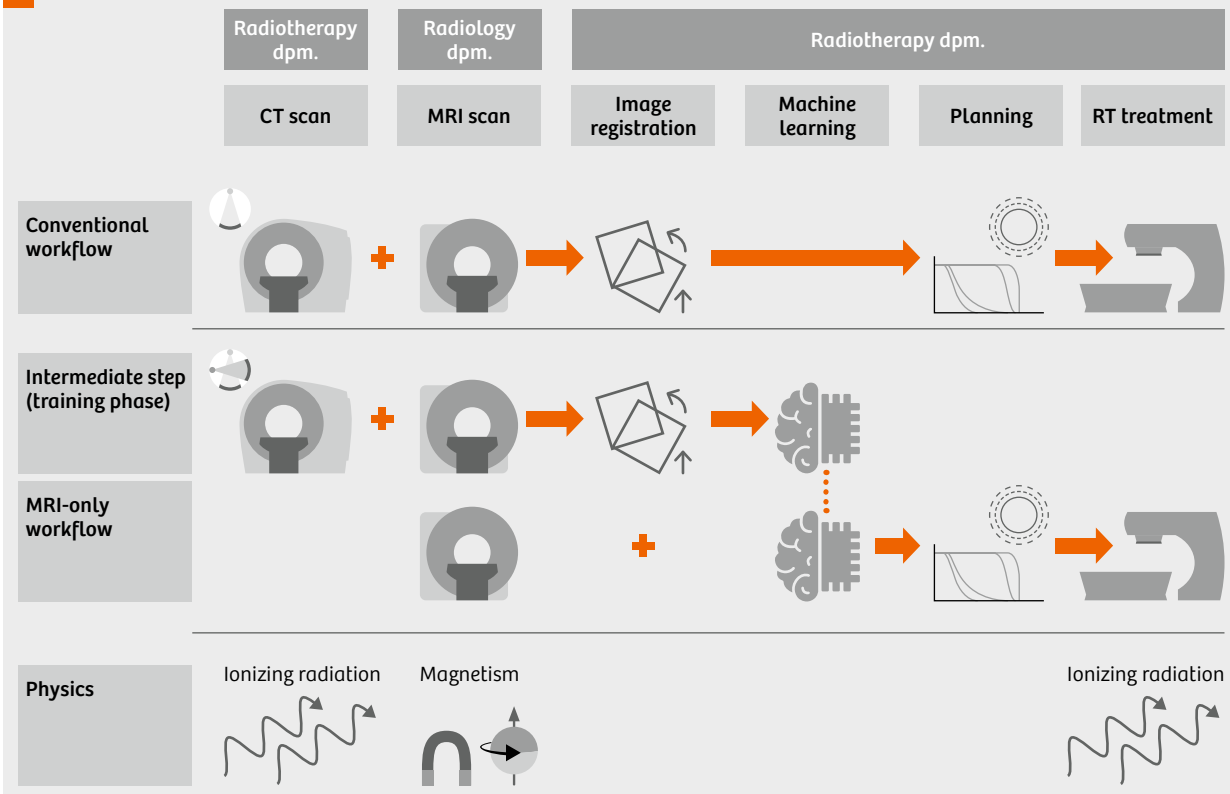

Figure 1:
This figure illustrates the conventional radiotherapy workflow and an MRI-only synthetic-CT workflow. The intermediate step, that consists of employing DECT to train a voxel-based or hybrid synthetic-CT (MRI-only) model, is also shown. It is expected that this will allow for relatively accurate proton beam range calculations in the MRI-only workflow. Furthermore, the physics behind the modalities are illustrated, showing that the MRI-only synthetic-CT based workflow eliminates the ionizing radiation dose for the purpose of proton therapy planning. Abbreviation: dpm., department.

validation cohorts of brain and prostate cancer patients. They show that for accurate MR-based proton dose calculation sophisticated synthetic CT approaches are required and that simple bulk density assignment methods are not adequate. Especially the correct modelling of internal air cavities was found to be crucial. Clinical implementation of MR-based proton therapy planning will require further investigations on the basis of considerably larger patient groups. Additionally, studies for more complex anatomical situations (where the proton beam would have to pass through considerable air or bone areas or where frequent anatomical changes are expected) are required.

In an MR-only based workflow, repeated imaging can be performed without the need for ionizing radiation, allowing for treatment monitoring and adaptation of the treatment plan on a day to day basis. Real-time MR-guided X-ray beam radiotherapy has been accomplished in combined (hybrid) MR-LINAC systems and was clinically launched in 2014 [43]. Real-time MR-guided proton therapy is receiving increased attention and is expected to be realized in the future.

Combined MR-PT machines are expected to further maximize tumor control probability and minimize radiation-related toxicity compared to real-time MR-guided photon therapy, due to the superior physical properties of the proton beam. Especially for moving tumors, real-time MR-guidance would lead to a better control of motion uncertainties and therefore improved radiotherapy treatments. Furthermore, proton beam tracking, which has always been regarded as the ultimate solution to treat moving tumors [44–47], could become clinical reality with the development of real-time MR-guided proton therapy. The concept of proton beam tracking is to dynamically steer the treatment beam and adapt its energy as a function of real-time tumor position obtained from real-time images. A synthetic CT based workflow would be the prerequisite for a real-time MR-guided proton (beam tracked) therapy treatment.

Challenges

The geometric accuracy of MR images affects the accuracy of final target volume delineation. It is limited by system-related geometric distortions arising from inhomogeneities of the static magnetic field, that increase with increasing magnetic field strength [48]. Another cause of system related geometric distortions is non-linearity of the gradient magnetic fields [48], even though manufacturers do apply non-linearity corrections to correct for this. Insight in the magnitude of those distortions and their potential impact on dose delivery can be obtained by performing a dedicated phantom study. An undistorted reference map can be generated by making a CT-scan of an MR-compatible phantom [34, 37]. Mallozzi et al. [49] found in their phantom study that even with three-dimensional distortion correction, measurable nonlinearity can occur. In a phantom study done by Pappas et al. [48] for three clinical MR protocols, mean absolute distortions of less than 0.5 mm in any direction were found for their custom-made phantom that fits inside a head coil. However, they also found control point (total) dispositions of up to 2 mm at the edges of the imaged area. In terms of image guid-ance for proton planning this is a considerable level of distortion. In a phantom study done by Jafar et al. [50] in which a three-dimensional printed grid phantom was used to measure spatial distortion in three dimensions for six clinical used MRI scanners, an overall mean error of less than 2 mm was found for all scanners, when using the body coil for signal acquisition. However, maximum errors above 6 mm were also detected. Although the magnitude and orientation of distortion strongly depends on imaging parameters and other influences, these kind of phantom studies do illustrate that geometric distortion has to be taken into account for proton planning purposes due to its high sensitivity to spatial distortions.

Besides being system related, geometric distortions can also be tissue related [51, 52]. Those patient-related image distortions can be minimized by using a sufficient bandwidth, for example [53, 54]. However, the bandwidth affects also the signal-to-noise ratio in the acquired images [54, 55]. Artificial Intelligence (AI) might be used to correct for geometric distortions in clinical data, based on quantification of geometric distortions in the phantom study and data obtained in the training phase in the foreseen workflow (see Figure 1). AI refers to the analysis of data with the aim of deriving a model that is used to predict and anticipate possible future events based on inferences from this model [56].

To allow for real-time MR-guided proton therapy treatment in the future, several challenges have to be overcome. Combining multiple complex technologies in one MR-PT machine requires critical evaluation of technical feasibility as mutual disturbances are introduced. For example, the magnetic field of the MR scanner will have an impact on the proton beam tracks [57, 58]. The specific geometry of an MR-PT machine might influence functional aspects of both modalities. The complex geometry of such a machine might introduce geometrical distortions in the MR images due to the magnetic field inhomogeneity [59, 60]. The proton beam arc might be limited in the choice of possible beam angles [61] as compared to standard proton therapy. Besides those modality related aspects, real-time MR-guided proton therapy also poses high demands on computational power and treatment planning capabilities. To synchronize beam delivery to the target motion real-time measurement of the target

position and real time adaptation will be required. In order to achieve that, imaging processing will have to be fast and automatic, including dose-recalculation and evaluation. In addition, decision support would need to be provided to perform the appropriate actions.

Summary

Proton therapy allows for the conforming of high radiation dose to the tumor volume, while minimizing normal tissue damage. An MR-only workflow allows for repeated imaging as MR does not involve ionizing radiation, allowing for monitoring of the treatment and an adaptation of the treatment plan with a higher frequency compared to a CT & MR based workflow. An MR-only image guided workflow also has the potential to reduce errors due to the avoidance of CT & MR co-registration.

To enable MR-only radiation treatment planning, a reliable method that converts MR data into maps relevant for radiotherapy planning is needed. This can be provided by the concept of synthetic CT. Approaches include a voxel-based or hybrid synthetic CT workflow, in which DECT data is used in the training phase, of which the value will need to be evaluated in future studies. The dose distribution in proton therapy planning is generally relatively susceptible to errors as they increase the range uncertainty of the proton beam, and therefore the use of DECT data is expected to increase accuracy of proton dose calculations. Overall the efficient and reliable generation of MR based synthetic CT images is an important prerequisite for realization of real-time MR-guided proton therapy in the future.

References

1 S. E. McGowan, N. G. Burnet, and A. J. Lomax, "Treatment planning optimisation in proton therapy.," Br. J. Radiol., vol. 86, no. 1021, p. 20120288, Jan. 2013.
2 A. J. Lomax, "Charged particle therapy: the physics of interaction.," Cancer J., vol. 15, no. 4, pp. 285–91, 2009.
3 J. M. Edmund and T. Nyholm, "A review of substitute CT generation for MRI-only radiation therapy," Radiat. Oncol., vol. 12, no. 1, p. 28, 2017.
4 H. Paganetti, "Range uncertainties in proton therapy and the role of Monte Carlo simulations," Phys. Med. Biol., vol. 57, no. 11, pp. R99–R117, Jun. 2012.
5 J. Kim et al., "Dosimetric evaluation of synthetic CT relative to bulk density assignment-based magnetic resonance-only approaches for prostate radiotherapy," Radiat. Oncol., vol. 10, p. 239, Nov. 2015.
6 E. Paradis, Y. Cao, T. S. Lawrence, C. Tsien, K. Vineberg, and J. M. Balter, "Assessing the dosimetric accuracy of MR-generated synthetic CT images for focal brain VMAT radiotherapy," Int. J. Radiat. Oncol. Biol. Phys., vol. 93, no. 5, pp. 1154–1161, Dec. 2015.
7 A. D. Vellet, W. Romano, D. B. Bach, R. B. Passi, D. H. Taves, and P. L. Munk, "Adenocarcinoma of the pancreatic ducts: comparative evaluation with CT and MR imaging at 1.5 T.," Radiology, vol. 183, no. 1, pp. 87–95, Apr. 1992.
8 Y. K. Lee et al., "Radiotherapy treatment planning of prostate cancer using magnetic resonance imaging alone.," Radiother. Oncol., vol. 66, no. 2, pp. 203–216, Feb. 2003.
9 D. Lu et al., "Comparison of intensity-modulated radiation therapies," Appl Rad Oncol., vol. 5, no. 4, pp. 20–27, 2016.
10 ICRP, "The 2007 Recommendations of the International Commission on Radiological Protection.," in ICRP Publication 103. Ann ICRP, vol. 37, no. (2-4), 2007.
11 B. Patyal, "Dosimetry Aspects of Proton Therapy," Technol. Cancer Res. Treat., vol. 6, no. 4_suppl, pp. 17–23, Aug. 2007.
12 H. Suit et al., "Proton vs carbon ion beams in the definitive radiation treatment of cancer patients," Radiother. Oncol., vol. 95, no. 1, pp. 3–22, 2010.
13 A. J. Lomax et al., "A treatment planning inter-comparison of proton and intensity modulated photon radiotherapy," Radiother. Oncol., vol. 51, no. 3, pp. 257–271, 1999.
14 J. A. Langendijk, P. Lambin, D. De Ruysscher, J. Widder, M. Bos, and M. Verheij, "Selection of patients for radiotherapy with protons aiming at reduction of side effects: the model-based approach.," Radiother. Oncol., vol. 107, no. 3, pp. 267–273, Jun. 2013.
15 R. Lin, E. B. Hug, R. A. Schaefer, D. W. Miller, J. M. Slater, and J. D. Slater, "Conformal proton radiation therapy of the posterior fossa: a study comparing protons with three-dimensional planned photons in limiting dose to auditory structures," Int. J. Radiat. Oncol., vol. 48, no. 4, pp. 1219–1226, 2000.
16 E. Johnstone et al., "Systematic Review of Synthetic Computed Tomography Generation Methodologies for Use in Magnetic Resonance Imaging–Only Radiation Therapy," Int. J. Radiat. Oncol., vol. 100, no. 1, pp. 199–217, 2018.
17 J. J. W. Lagendijk, B. W. Raaymakers, and M. van Vulpen, "The Magnetic Resonance Imaging–Linac System," Semin. Radiat. Oncol., vol. 24, no. 3, pp. 207–209, 2014.
18 A. J. den Dekker and J. Sijbers, "Data distributions in magnetic resonance images: A review," Phys. Medica, vol. 30, no. 7, pp. 725–741, 2014.
19 H. Wang, H. Chandarana, K. T. Block, T. Vahle, M. Fenchel, and I. J. Das, "Dosimetric evaluation of synthetic CT for magnetic resonance-only based radiotherapy planning of lung cancer," Radiat. Oncol., vol. 12, p. 108, Jun. 2017.
20 A. S. Soliman et al., "A realistic phantom for validating MRI-based synthetic CT images of the human skull," Med. Phys., vol. 44, no. 9, pp. 4687–4694, 2017.
21 X. Han, "MR-based synthetic CT generation using a deep convolutional neural network method.," Med. Phys., vol. 44, no. 4, pp. 1408–1419, Apr. 2017.
22 D. Andreasen, K. Van Leemput, R. H. Hansen, J. A. L. Andersen, and J. M. Edmund, "Patch-based generation of a pseudo CT from conventional MRI sequences for MRI-only radiotherapy of the brain," Med. Phys., vol. 42, no. 4, pp. 1596–1605, 2015.
23 S.-H. Hsu, Y. Cao, K. Huang, M. Feng, and J. M. Balter, "Investigation of a method for generating synthetic CT models from MRI scans of the head and neck for radiation therapy.," Phys. Med. Biol., vol. 58, no. 23, pp. 8419–8435, Dec. 2013.
24 M. S. R. Gudur, W. Hara, Q.-T. Le, L. Wang, L. Xing, and R. Li, "A unifying probabilistic Bayesian approach to derive electron density from MRI for radiation therapy treatment planning.," Phys. Med. Biol., vol. 59, no. 21, pp. 6595–6606, Nov. 2014.
25 F. Guerreiro et al., "Evaluation of a multi-atlas CT synthesis approach for MRI-only radiotherapy treatment planning.," Phys. Med., vol. 35, pp. 7–17, Mar. 2017.
26 T. Nyholm, M. Nyberg, M. G. Karlsson, and M. Karlsson, "Systematisation of spatial uncertainties for comparison between a MR and a CT-based radiotherapy workflow for prostate treatments," Radiat. Oncol., vol. 4, p. 54, Nov. 2009.
27 B. Demol, C. Boydev, J. Korhonen, and N. Reynaert, "Dosimetric characterization of MRI-only treatment planning for brain tumors in atlas-based pseudo-CT images generated from standard T1-weighted MR images," Med. Phys., vol. 43, no. 12, pp. 6557–6568, 2016.
28 J. H. Jonsson, A. Johansson, K. Soderstrom, T. Asklund, and T. Nyholm, "Treatment planning of intracranial targets on MRI derived substitute CT data.," Radiother. Oncol., vol. 108, no. 1, pp. 118–122, Jul. 2013.
29 P. Wohlfahrt et al., "Clinical Implementation of Dual-energy CT for Proton Treatment Planning on Pseudo-monoenergetic CT scans," Int. J. Radiat. Oncol., vol. 97, no. 2, pp. 427–434, 2017.

30 M. Yang et al., "Comprehensive analysis of proton range uncertainties related to patient stopping-power-ratio estimation using the stoichiometric calibration.," Phys. Med. Biol., vol. 57, no. 13, pp. 4095–4115, Jul. 2012.
31 D. Han, J. V Siebers, and J. F. Williamson, "A linear, separable two-parameter model for dual energy CT imaging of proton stopping power computation," Med. Phys., vol. 43, no. 1, pp. 600–612, 2016.
32 J. Zhu and S. N. Penfold, "Dosimetric comparison of stopping power calibration with dual-energy CT and single-energy CT in proton therapy treatment planning," Med. Phys., vol. 43, no. 6Part1, pp. 2845–2854, 2016.
33 V. T. Taasti, J. B. B. Petersen, L. P. Muren, J. Thygesen, and D. C. Hansen, "A robust empirical parametrization of proton stopping power using dual energy CT," Med. Phys., vol. 43, no. 10, pp. 5547–5560, 2016.
34 D. Andreasen, J. M. Edmund, V. Zografos, B. H. Menze, and K. Van Leemput, "Computed tomography synthesis from magnetic resonance images in the pelvis using multiple random forests and auto-context features," 2016, vol. 9784, no., pp. 978417–978418.
35 D. M. Grodzki, P. M. Jakob, and B. Heismann, "Ultrashort echo time imaging using pointwise encoding time reduction with radial acquisition (PETRA).," Magn. Reson. Med., vol. 67, no. 2, pp. 510–518, Feb. 2012.
36 R. Krug et al., "Ultrashort Echo Time Magnetic Resonance Imaging of Cortical Bone at 7 Tesla Field Strength: A Feasibility Study," J. Magn. Reson. Imaging, vol. 34, no. 3, pp. 691–695, Sep. 2011.
37 S.-H. Hsu et al., "Quantitative characterizations of ultrashort echo (UTE) images for supporting air-bone separation in the head.," Phys. Med. Biol., vol. 60, no. 7, pp. 2869–2880, Apr. 2015.
38 E. M. Kerkhof, J. M. Balter, K. Vineberg, and B. W. Raaymakers, "Treatment plan adaptation for MRI-guided radiotherapy using solely MRI data: a CT-based simulation study.," Phys. Med. Biol., vol. 55, no. 16, pp. N433-40, Aug. 2010.
39 L. Koivula, "Magnetic resonance imaging- based radiation therapy treatment planning," Master's Thesis, University of Helsinki, 2016.
40 J. Korhonen et al., "Feasibility of MRI-based reference images for image-guided radiotherapy of the pelvis with either cone-beam computed tomography or planar localization images.," Acta Oncol., vol. 54, no. 6, pp. 889–895, Jun. 2015.
41 L. Koivula, L. Wee, and J. Korhonen, "Feasibility of MRI-only treatment planning for proton therapy in brain and prostate cancers: Dose calculation accuracy in substitute CT images.," Med. Phys., vol. 43, no. 8, p. 4634, Aug. 2016.
42 M. Maspero et al., "Feasibility of MR-only proton dose calculations for prostate cancer radiotherapy using a commercial pseudo-CT generation method.," Phys. Med. Biol., vol. 62, no. 24, pp. 9159–9176, Nov. 2017.
43 S. Mutic and J. F. Dempsey, "The ViewRay System: Magnetic Resonance–Guided and Controlled Radiotherapy," Semin. Radiat. Oncol., vol. 24, no. 3, pp. 196–199, Jan. 2018.
44 C. Bert, C. Graeff, M. Riboldi, S. Nill, G. Baroni, and A.-C. Knopf, "Advances in 4D treatment planning for scanned particle beam therapy - report of dedicated workshops.," Technol. Cancer Res. Treat., vol. 13, no. 6, pp. 485–495, Dec. 2014.
45 S. Mori, S. Zenklusen, and A.-C. Knopf, "Current status and future prospects of multi-dimensional image-guided particle therapy.," Radiol. Phys. Technol., vol. 6, no. 2, pp. 249–272, Jul. 2013.
46 A. Knopf et al., "Challenges of radiotherapy: report on the 4D treatment planning workshop 2013.," Phys. Med., vol. 30, no. 7, pp. 809–815, Nov. 2014.
47 A.-C. Knopf et al., "Required transition from research to clinical application: Report on the 4D treatment planning workshops 2014 and 2015," Phys. Medica, vol. 32, no. 7, pp. 874–882, 2016.
48 E. P. Pappas et al., "MRI-Related Geometric Distortions in Stereotactic Radiotherapy Treatment Planning: Evaluation and Dosimetric Impact.," Technol. Cancer Res. Treat., vol. 16, no. 6, pp. 1120–1129, Dec. 2017.
49 R. P. Mallozzi, D. J. Blezek, J. L. Gunter, C. R. Jack, JR, and J. R. Levy, "Phantom-Based Evaluation of Gradient Nonlinearity for Quantitative Neurological MRI Studies," Proc. Intl. Soc. Mag. Reson. Med. 14, 2006.
50 M. Jafar, Y. Jafar, C. Dean, and M. Miquel, "Assessment of Geometric Distortion in Six Clinical Scanners Using a 3D-Printed Grid Phantom," J. Imaging, vol. 3, no. 3, p. 28, Jul. 2017.
51 M. Karlsson, M. G. Karlsson, T. Nyholm, C. Amies, and B. Zackrisson, "Dedicated magnetic resonance imaging in the radiotherapy clinic.," Int. J. Radiat. Oncol. Biol. Phys., vol. 74, no. 2, pp. 644–651, Jun. 2009.
52 D. Wang, W. Strugnell, G. Cowin, D. M. Doddrell, and R. Slaughter, "Geometric distortion in clinical MRI systems Part II: correction using a 3D phantom.," Magn. Reson. Imaging, vol. 22, no. 9, pp. 1223–1232, Nov. 2004.
53 G. P. Liney and M. A. Moerland, "Magnetic Resonance Imaging Acquisition Techniques for Radiotherapy Planning," Semin. Radiat. Oncol., vol. 24, no. 3, pp. 160–168, 2014.
54 M. Adjeiwaah, M. Bylund, J. A. Lundman, C. T. Karlsson, J. H. Jonsson, and T. Nyholm, "Quantifying the Effect of 3T Magnetic Resonance Imaging Residual System Distortions and Patient-Induced Susceptibility Distortions on Radiation Therapy Treatment Planning for Prostate Cancer," Int. J. Radiat. Oncol., vol. 100, no. 2, pp. 317–324, 2018.
55 A. Walker et al., "MRI geometric distortion: Impact on tangential whole-breast IMRT," J. Appl. Clin. Med. Phys., vol. 17, no. 5, pp. 1–13, Sep. 2016.
56 Government Office for Science, "Artificial Intelligence: oppertunities and implications for the future of decision making," 2016.
57 B. W. Raaymakers, A. J. E. Raaijmakers, and J. J. W. Lagendijk, "Feasibility of MRI guided proton therapy: magnetic field dose effects.," Phys. Med. Biol., vol. 53, no. 20, pp. 5615–5622, Oct. 2008.
58 M. Moteabbed, J. Schuemann, and H. Paganetti, "Dosimetric feasibility of real-time MRI-guided proton therapy.," Med. Phys., vol. 41, no. 11, p. 111713, Nov. 2014.
59 L. N. Baldwin, K. Wachowicz, and B. G. Fallone, "A two-step scheme for distortion rectification of magnetic resonance images.," Med. Phys., vol. 36, no. 9, pp. 3917–3926, Sep. 2009.
60 S. P. M. Crijns, B. W. Raaymakers, and J. J. W. Lagendijk, "Real-time correction of magnetic field inhomogeneity-induced image distortions for MRI-guided conventional and proton radiotherapy.," Phys. Med. Biol., vol. 56, no. 1, pp. 289–297, Jan. 2011.
61 Ding X, Li X, Zhang JM, Kabolizadeh P, Stevens C, Yan D, "Spot-Scanning Proton Arc (SPArc) Therapy: The First Robust and Delivery-Efficient Spot-Scanning Proton Arc Therapy," Int J Radiat Oncol Biol Phys. 2016 Dec 1;96(5):1107-1116. doi: 0.1016/j.ijrobp.2016.08.049. Epub 2016 Sep 7.

Contact

Ir. S.E.M. Huijsse
Medical Physicist, Ph.D. student
Department of Radiology,
Medical Imaging Center,
University Medical Center Groningen

PO Box 30 001
9700 RB Groningen
The Netherlands
s.e.m.huijsse@umcg.nl

Dr. R.J.H. Borra
M.D., Ph.D. – MR Research Lead
Department of Nuclear Medicine and Molecular Imaging, Medical Imaging Center,
University Medical Center Groningen

PO Box 30 001
9700 RB Groningen
The Netherlands
r.j.h.borra@umcg.nl

MR-simulation for radiotherapy treatment planning of head and neck cancer using 3T MAGNETOM Vida

Daniela Thorwarth[1]; Kerstin Zwirner[2]; René M. Winter[1]; Stefan Welz[2]; Daniel Zips[2]; Sergios Gatidis[3]; Jakob Weiß[3]; Konstantin Nikolaou[3]

[1] Section for Biomedical Physics, Department of Radiation Oncology, University of Tübingen, Germany
[2] Department of Radiation Oncology, University of Tübingen, Germany
[3] Department of Radiology, Diagnostic and Interventional Radiology, University of Tübingen, Germany

Abstract

Purpose
To explore the potential of the new 3T MAGNETOM Vida for magnetic resonance (MR)-based radiotherapy (RT) simulation and treatment planning in head and neck cancer (HNC) patients as well as for follow-up imaging during RT treatment.

Methods and materials
A set-up has been defined to position HNC patients in RT treatment position for MR examination using the MAGNETOM Vida system for anatomical and functional image data acquisition before and during RT. MR imaging was performed using a flexible 18-channel body coil (Body 18) to allow positioning of the patient using a thermoplastic mask for head and shoulder fixation as well as a flat table top. T1-weighted contrast-enhanced as well as T2-weighted images were acquired to assess anatomical information. Additionally, diffusion-weighted (DW) MR image sequences were used for assessing functional tissue information.

Results
Our first experience with the described setting showed that imaging with the MAGNETOM Vida system in RT treatment position using the flexible coil is possible. Anatomical and functional MR image data showed very high image quality. Furthermore, MR data could be easily fused to planning CTs of HNC patients and were used for more accurate target volume and organ at risk delineation.

Conclusion
MR imaging before and during RT in treatment position is possible in the MAGNETOM Vida system. With this set-up, high image quality can be achieved, which is essential for improved target volume delineation in MR-guided RT.

Introduction

Magnetic resonance (MR) guided radiotherapy (RT) approaches have gained a lot of attention in the last years [1]. MR offers high resolution imaging of anatomical and functional tissue properties. In contrast to computed tomography (CT), MR imaging provides high soft tissue contrast. Consequently, MR imaging data may be extremely valuable for target volume delineation in high precision RT and also for assessing anatomical and functional changes in the tumor region early during treatment [2, 3].

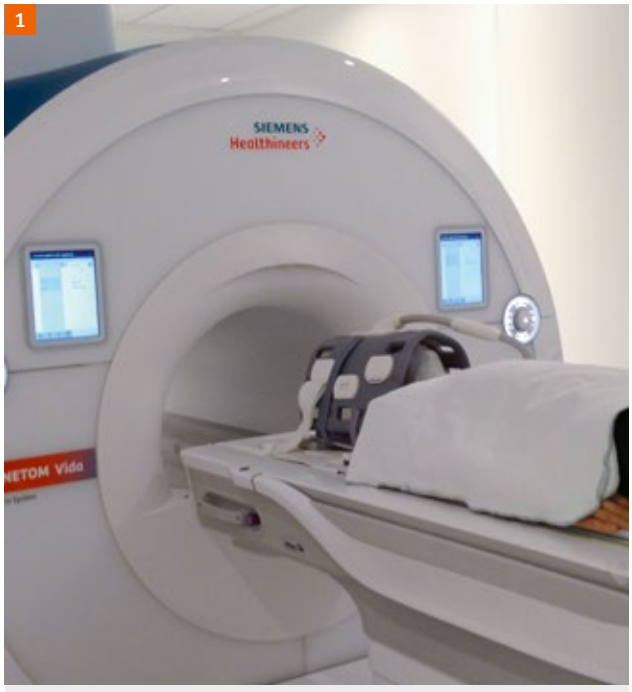

Figure 1:
Patient examination in radiotherapy specific position using a flat table top, a thermoplastic mask and a flexible body coil in the MAGNETOM Vida.

The new generation of MR scanners, such as the 3T MAGNETOM Vida, offer extremely fast and accurate imaging sequences to assess anatomical and functional characteristics of tumors and may thus be ideal tools for MR-based RT simulation and response assessment during treatment.

The aim of this project was to develop an imaging set-up on the MAGNETOM Vida system allowing for MR imaging of head and neck cancer (HNC) patients in RT treatment position, i.e. using a thermoplastic mask and a flat table top for integration into RT target delineation and treatment planning [4, 5].

Methods and materials

Imaging set-up

To allow MR imaging of HNC patients in RT treatment position using the MAGNETOM Vida system, a flat table top overlay (Qfix, Avondale, PA, USA) is positioned on top of the regular patient table. Patients are positioned on this flat table top using a thermoplastic mask (ITV, Innsbruck, Austria) which is fixed at the table top using an MR-compatible mask holder system.

For MR imaging, the flexible 18-channel body coil (Body 18) is positioned around the RT mask with a distance of approximately 2 cm (cf. Fig. 1) in addition to the integrated 72-channel spine coil.

Using this set-up, MR imaging is performed before the start of RT treatment and after approximately two weeks of treatment to analyse early treatment response.

Imaging protocol

The MR imaging protocol consists of the following sequences:

1. T2w anatomical MRI:
   A quiet T2w TSE anatomical sequence in transverse orientation is used for anatomical depiction of organ structures and oncologic findings using the following parameters: matrix 192 x 192, resolution 1.3 x 1.3 mm^2, slice thickness 4 mm, TE = 53 ms, TR = 8180 ms, STIR fat sat.
2. Diffusion-weighted imaging (DWI):
   DWI of the head/neck region is a challenge due to magnetic field inhomogeneities often resulting in image distortion, ghosting and signal loss which makes the use of DWI for RT planning difficult. The MAGNETOM Vida system offers technical solutions to overcome these limitations using readout-segmented (RESOLVE) echo-planar imaging (EPI) and slice specific shimming (SliceAdjust).

   DWI was thus performed using a RESOLVE sequence with SliceAdjust and eight different b-values (b = 0, 20, 40, 80, 120, 200, 500, 1000 s/mm^2) and the following parameters: matrix size 84 x 128, resolution 3 x 3 mm^2 (interpolated to 1.5 x 1.5 mm^2), slice thickness 5 mm, TE = 44 ms, TR = 10800 ms, with water-specific excitation.

   Subsequently, quantitative parameters are calculated including the apparent diffusion coefficient (ADC) but also perfusion parameters using multiple b-value images for intravoxel incoherent motion (IVIM) modelling. Thus detailed information about tissue perfusion and diffusion components can be obtained.
3. Dynamic contrast-enhanced imaging (DCE):
   DCE of the neck poses a challenge due to the necessity for high temporal resolution and the occurrence of involuntary pharyngeal and laryngeal motion. In order to overcome these challenges, the MAGNETOM Vida offers time-resolved radial imaging with compressed sensing reconstruction (GRASP). We implemented GRASP DCE of the neck region for quantitative analysis of tumor perfusion after injection of 0.1 mmol Gadobutrol/kg using the following parameters: matrix

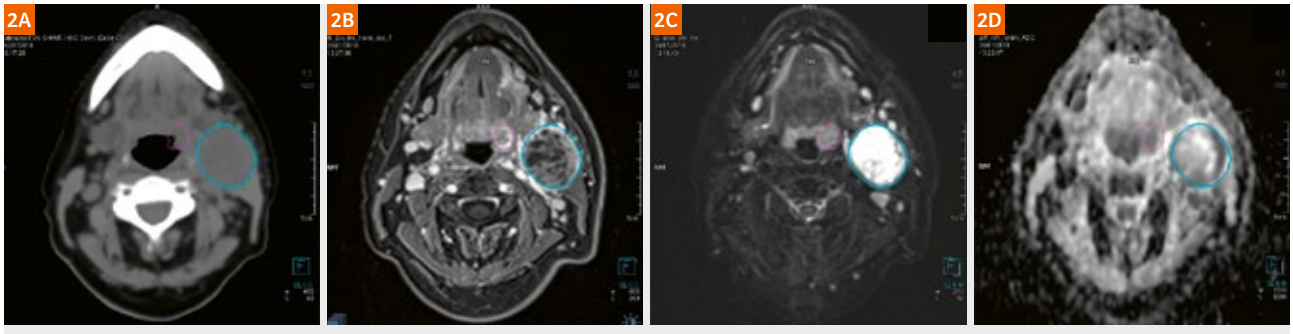

Figure 2:
CT and MR images for RT simulation in a patient with HNC. The primary tumor region is contoured in pink, a large lymph node metastasis in blue. Image data are shown in the following sequence: **(2A)** planning CT, **(2B)** T1w MR post contrast, **(2C)** T2w MR image (STIR) and **(2D)** ADC map.

size 224 x 224, resolution 1.1 x 1.1 mm^2, slice thickness 3 mm, TR = 4.14 ms, TE = 1.86 ms with spectral fat saturation. Dynamic frames were reconstructed with a time resolution of 4.3 s.

4. T1w post contrast:
   After DCE, a highly resolved isotropic T1-weighted contrast-enhanced VIBE sequence is performed for detailed anatomical depiction of the structures of interest using the following parameters: matrix size 270 x 320, resolution 1 x 1 x 1 mm^3, TR 6.56 ms, TEs 2.46 and 3.72 ms, with Dixon fat sat.

Axial, coronal and sagittal reformations are automatically performed within the *syngo* RT image suite.

Target volume delineation for radiotherapy treatment planning

After successful image acquisition, MR imaging data were transferred to the RT treatment planning system or a dedicated contouring system (RT image suite, Siemens Healthcare, Erlangen, Germany). Here, the MR data was registered to the RT planning computed tomography (CT) scan and used for target volume and organ at risk (OAR) delineation.

Results

First experience on five patients with this set-up showed MR images of high, diagnostic quality. In particular, we observed high image quality and anatomical accuracy of DWI using the RESOLVE sequence with slice adjust and of DCE using GRASP. An image example is provided in Figure 2.

Patients tolerated imaging in RT treatment position well, as the net imaging time for the RT simulation sequences was approximately 20 minutes. MR imaging data for each patient was transferred to the RT treatment planning system (Oncentra Masterplan, Elekta AB, Sweden) as well as to the *syngo*.via application RT image Suite for registration to the planning CT and tumor as well as OAR contouring. Rigid as well as deformable image registration with the planning CT worked very well due to the same patient positioning with flat table top and thermoplastic mask. Figure 2 presents an example of a patient examined with the 3T MAGNETOM Vida system for RT simulation.

In addition to anatomical information assessed from T1w and T2w MR sequences we aim for measuring functional properties of tumors using DW-MR imaging. IVIM data with eight different b-values were of very high quality in the first patients. Hence, quantitative ADC maps as well as information on perfusion and diffusion from a bi-exponential fit could be acquired.

Discussion

With the proposed set-up, consisting of a thermoplastic mask, a flat table top and a flexible body coil high quality anatomical and functional MR imaging in RT treatment position is possible for patients with HNC. Thus, this set-up constitutes an optimal tool for pre-treatment RT simulation in order to gain accuracy in target volume delineation as well as for the assessment of functional information in terms of ADC or IVIM data. Advanced MR sequence techniques such as RESOLVE DWI with slice adjust and GRASP together with the available hardware of the Vida System provide the necessary qualitative and quantitative image quality for precise RT planning.

Moreover, additional follow-up data can be acquired early during RT where this set-up may be beneficial to quantify radiation induced functional changes on a regional or even voxel level. Such quantitative and geometrically accurate data might be used in the future as a basis for individualized RT treatment interventions as e.g. dose painting.

Contact

Daniela Thorwarth
Section of Biomedical Physics
University Hospital for Radiation Oncology
University of Tübingen

Hoppe-Seyler-Strasse 3
72076 Tübingen
Germany
daniela.thorwarth@med.uni-tuebingen.de

References

1 Lagendijk JJW, Raaymakers BW, Van den Berg CAT, Moerland MA, Philippens ME, van Vulpen M. MR guidance in radiotherapy. Phys Med Biol 2014;59:R349-69.
2 Van der Heide UA, Houweling AC, Groenendaal G, Beets-Tran RGH, Lambin P. Functional MRI for radiotherapy dose painting. Magn Reson Imaging 2012;30:1216-23.
3 Baumann M, Krause M, Overgaard J, et al. Radiation oncology in the era of precision medicine. Nat Rev Cancer 2016;16:234-9.
4 Hanvey S, McJury M, Tho LM, et al. The influence of MRI scan position with oropharyngeal cancer undergoing radical radiotherapy. Radiat Oncol 2013;8:129.
5 Fortunati V, Verhaart RF, Verdujin GM, et al. MRI integration into treatment planning of head and neck tumors: Can patient immobilization be avoided? Radiother Oncol 2015;115:191-4.

Cine-magnetic resonance imaging for assessment of larynx motion in early glottic cancer radiotherapy

Houda Bahig, M.D.[1,2]; Phuc Félix Nguyen-Tan, M.D.[1,2]; Édith Filion, M.D.[1,2]; David Roberge, M.D.[1,2]; Pensavan Thanomsack[1]; Jacques de Guise, Ph.D.[2]; Danis Blais, M.Sc.[1]; Robert Doucet, M.Sc.[1]; Laurent Létourneau-Guillon, M.D.[2,3]; Louise Lambert, M.D.[1,2]

[1] Radiation Oncology Department, Centre Hospitalier de l'Université de Montréal, Montreal, QC, Canada
[2] CHUM Research Center, Montreal, QC, Canada
[3] Radiology Department, Centre Hospitalier de l'Université de Montréal, Montreal, QC, Canada

Introduction

Radiation therapy is an essential component of early glottic cancer treatment. Radical radiotherapy outcomes for early glottic cancer are excellent with reported 5-year local control (LC) rates reaching 95% and 85% for T1 and T2 lesions respectively, and 5-year overall survival (OS) exceeding 90% [1–5]. In recent years, increasing interest in reducing radiation treatment volumes has emerged, with the objective of reducing toxicity while maintaining LC. Although surgical approach involves the resection of tumor-bearing vocal cord, radiotherapy currently involves irradiation of the entire larynx. In an era of intensity modulated radiotherapy (IMRT) and image guided radiotherapy (IGRT), the rationale for this discrepancy becomes difficult to justify – it is therefore appealing to mirror surgical approaches and migrate towards partial larynx irradiation.

The group from Erasmus Medical Center Cancer Institute have previously reported feasibility [6] and, more recently, excellent LC outcomes from a retrospective analysis of 30 patients with T1aN0 glottic cancer treated with single vocal cord IMRT [7]. However, internal motion of the larynx is generally associated with fear of geographical miss with the use of IMRT and tighter treatment margins. Internal larynx motion includes swallowing, respiration as well as isolated, more sudden movements, attributed to tongue motion [9]. In the context of conventional radiotherapy using lateral opposed fields, previous studies have evaluated laryngeal motion and found a negligible dose reduction of 0.5% with swallowing [9, 10]. In the era of IMRT and partial larynx irradiation, it becomes crucial to adequately select planning margins. Use of cine magnetic resonance imaging (MRI) is an opportunity to capture the swallowing and breathing motion of the larynx of each patient. Cine-MRI can be acquired over a prolonged period of time at no radiation cost, it is therefore most representative of the natural motion that can occur in the larynx over a given duration of time.

Cine-MRI can be used to determine personalized internal target volume (ITV) margin based on individual motion. If cine-MRI cannot be obtained for each patient, populational internal target margin can be generated for use in the clinic. In this study, we use cine-MRI for assessment of larynx motion in a cohort of patients treated with IMRT for early glottic larynx cancer.

Material and methods

Study population

A total of 20 patients were prospectively enrolled in this study from August 2014 to January 2016. Eligibility criteria included:

1. histologically proven glottic cancer,
2. stage TisN0, T1a-bN0 or T2N0 as per the American Joint Committee on Cancer 7th edition,
3. Eastern Cooperative Oncology Group performance status 0–2.

Patients with prior radiation to the head and neck region were excluded.

The protocol and patient consent form were reviewed and approved by our institutional ethics committee.

Planning CT and MRI

All patients had a 1.5 mm slice thickness planning computed tomography (CT) scan (SOMATOM Definition Flash, Siemens Healthcare, Forchheim, Germany) from the vertex to the carina with and without intravenous contrast injection in supine position. Immobilisation device included a thermoplastic mask of the head and shoulder fixed to the treatment table. Patients were instructed not to swallow during acquisition of planning CT.

Patients underwent planning MRI on a RT-dedicated 1.5 Tesla system (MAGNETOM Aera, Siemens Healthcare, Erlangen, Germany). Transverse T2-weighted Turbo Spin Echo (TSE), T1-weighted TSE and post-gadolinium

T1-weighted fat saturated TSE sequences were obtained for planning purposes. Cine-MRI used for motion assessment consisted in sagittal non-enhanced true fast imaging with steady state precession (TrueFISP) sequences acquired using a rapid acquisition protocol (10 mm thickness extending cranio-caudally, temporal resolution of 3.8 images per second). These cine-MRI sequences were acquired pre-treatment as well as mid-treatment, to assess changes in motion over time. MRI sequences were acquired in treatment position, using a Spine matrix coil posteriorly and a large flex coil anteriorly (Siemens Healthcare, Erlangen, Germany). TrueFISP sequence parameters were as follow: TR = 262 ms, TE = 1.2 ms, field-of-view = 256 mm, and spatial resolution = 2 x 2 x 10 mm. To capture the natural frequency of swallowing and the impact of the treating team's instruction not to swallow, a first 2-minute acquisition with the patient given no particular instruction was followed by a 2-minute acquisition with the patient instructed not to swallow. Laryngeal motion analysis on cine-MRI was performed on a MimVista workstation (version 6.2, MimVista software Inc, Cleveland, OH, USA). In addition to extent of motion, cine-MRI was used to assess swallowing frequency and time (Fig. 1).

Results

Patient characteristics

In total, the study included 17 males (85%) and 3 females (15%) and the median age was 67 (51–77). Tumors were stage Tis, T1 and T2N0 in 3 (15%), 5 (25%) and 12 (60%) patients, respectively. 17 lesions (85%) were unilateral, 2 lesions (10%) were bilateral and 1 involved the anterior commissure. For the entire cohort, median gross tumor volume was 1 cm^3 (1–2). Median dose was 65.25 Gy in 29 fractions (63–65.25).

Dynamics of laryngeal motion

Swallowing frequency and time

On pre-treatment cine-MRI, mean swallowing frequency over 2-minutes was 1 (0–5) and was significantly reduced to 0 (0–1) when patients were instructed not to swallow ($p = 0.03$). This translated into a reduction in percentage of time spent swallowing from 2.3% (0–10%) with no instruction to 0.5% (0–2.5%) with instruction ($p = 0.06$.) Mid-treatment cine-MRI showed mean swallowing frequency of 0, with or without instruction not to swallow.

Detailed laryngeal motion dynamics

Mean amplitudes of swallowing motion in the superior, inferior, anterior and posterior directions on cine-MRI are presented in table 1. Greatest extent of motion was observed in the superior direction with a mean exceeding 20 mm, and in the anterior direction with a mean of 6 mm. Mean swallowing motion in the inferior and posterior directions were ≤ 1 mm (Table 1). In addition, when the larynx was in resting position, a mean respiratory motion of 4 mm (1–6) and 2 mm (1–2) in the supero-inferior (SI) and antero-posterior (AP) directions was demonstrated.

Discussion

Swallowing was associated with an important motion that was typically beyond 20 mm in the superior direction and within 6 mm in the anterior direction, consistent with previous studies [10–13]. Swallowing motion was typically minimal in both posterior and inferior directions. As was previously well shown in the context of conformational radiotherapy [9–12], our results demonstrate that swallowing motion is rapid, rare over a 2 minute period and further decreased with instruction not to swallow. Swallowing motion is therefore unlikely to be a concern in larynx irradiation. Whether patients were given instructions or not, swallowing frequency was significantly reduced mid-treatment compared to pre-treatment; possible explanations include increasing radiation-induced swallowing discomfort over time, or simply that patients may become more at ease with the treatment procedure over time. Similarly, in the context of opposed wedge fields, van Asselen et al. reported swallowing to occur over 0.45% of the total irradiation time (typically delivered over less

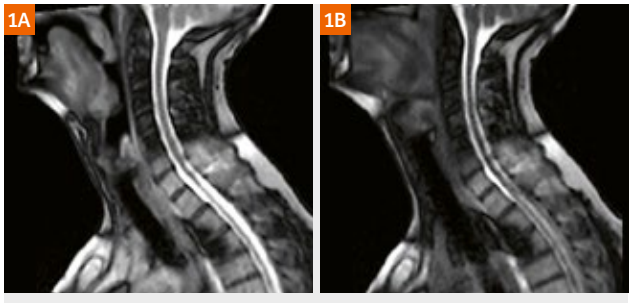

Figure 1:
Sagittal TrueFISP MRI sequences for assessment of laryngeal motion showing showing most inferior **(1A)** and most superior **(1B)** larynx position during swallowing.

	Swallowing		Resting	
Motion (mm)	Pre-Tx MRI	Mid-Tx MRI	Pre-Tx MRI	Mid-Tx MRI
Sup (M ± SD)	23 ± 5	22 ± 6	4 ± 2	3 ± 2
Inf (M ± SD)	1 ± 1	1 ± 1		
Ant (M ± SD)	6 ± 2	6 ± 2	2 ± 1	1 ± 1
Post (M ± SD)	1 ± 1	0 ± 1		

Table 1:
Summary of larynx motion dynamics on dynamic 2D MRI.

Pre-tx = Pre-treatment, Mid-tx = Mid-treatment, Sup = superior, Inf = inferior, Ant= anterior, Post = posterior, M = mean, N = number, SD = standard deviation

than 1 minute) [9] and Hamlet et al. [10] reported an average dose reduction of 0.5% due to swallowing.

If swallowing motion unlikely impacts dose delivery to the tumor in the context of partial larynx irradiation, respiratory larynx motion reaching 6 mm in the supero-inferior direction and 2 mm in the antero-posterior direction was observed in the context of this study. Van Asselen et al. previously reported non-swallowing motion to occur at varying frequency (reaching up 20 times per minute) and associated with displacement reaching 11 mm and 6 mm in SI and AP directions, respectively, attributed to respiration as well as occasional occurrence of isolated tongue motion [9]. Brady et al. [13] also described a respiratory larynx motion on dynamic MRI reaching 3 mm. Importantly, such intra-fraction motion cannot be addressed by means of daily image guidance. Although current margins used in whole larynx irradiation are largely sufficient to include respiratory motion, regular and consistent respiratory motion can be associated with a risk of marginal miss in partial larynx irradiation if not properly taken into account. In the context of partial larynx IMRT, it is therefore of crucial importance to include an internal motion margin that accounts for respiration. This margin can be personalized, using a cine-MRI for each patient at time of treatment planning. This would represent the best case scenario to minimize unnecessary irradiation in patients with minimal motion and ensure safe treatment delivery in patients with larger range of motion. Alternatively, as suggested by the results of our study, maximum respiratory motion observed was within 6 mm for all patients. In order to derive a safe population-based margin to be generalized to any patient, assessment of respiratory motion in a large sample of patients is currently on-going at our institution.

Conclusion

Although swallowing motion is associated with large larynx excursion reaching beyond 2 cm in the superior direction, swallowing motion was reported to be rare, rapid and easily suppressed by patients, and is therefore considered to have negligible impact on RT dose delivery.

Contact

Houda Bahig, M.D.
Radiation Oncologist
Centre Hospitalier de l'Université de Montréal

1560 Sherbrooke Street East
H2L 4M1
Montreal, QC
Canada
houda.bahig.chum@ssss.gouv.qc.ca

Houda Bahig

Louise Lambert

On the other hand, respiratory motion reaching 6 mm in the superior-inferior direction and 2 mm in the antero-posterior direction was revealed on cine-MRI studies. When considering partial larynx IMRT, an internal motion margin should be used to account for this respiratory motion. Cine-MRI can be used to derive a personalized margin based on observed larynx motion of individual patients. Assessment of respiratory motion in a large cohort of patients using cine-MRI is currently on-going, and will help determine safe generalizable internal motion margin in the absence of cine-MRI.

References

1 Mendenhall WM, Werning JW, Hinerman RW, Amdur RJ, Villaret DB. Management of T1-T2 glottic carcinomas. Cancer. 2004;100(9):1786-92.
2 Smee RI, Meagher NS, Williams JR, Broadley K, Bridger GP. Role of radiotherapy in early glottic carcinoma. Head & neck. 2010;32(7):850-9.
3 Cellai E, Frata P, Magrini SM, Paiar F, Barca R, Fondelli S, et al. Radical radiotherapy for early glottic cancer: Results in a series of 1087 patients from two Italian radiation oncology centers. I. The case of T1N0 disease. International journal of radiation oncology, biology, physics. 2005;63(5):1378-86.
4 Dinshaw KA, Sharma V, Agarwal JP, Ghosh S, Havaldar R. Radiation therapy in T1-T2 glottic carcinoma: influence of various treatment parameters on local control/complications. International journal of radiation oncology, biology, physics. 2000;48(3):723-35.
5 Le QT, Fu KK, Kroll S, Ryu JK, Quivey JM, Meyler TS, et al. Influence of fraction size, total dose, and overall time on local control of T1-T2 glottic carcinoma. International journal of radiation oncology, biology, physics. 1997;39(1):115-26.
6 Osman SO, Astreinidou E, Levendag PC, Heijmen BJ. Impact of geometric variations on delivered dose in highly focused single vocal cord IMRT. Acta Oncol. 2014;53(2):278-85.
7 Al-Mamgani A, Kwa SL, Tans L, Moring M, Fransen D, Mehilal R, et al. Single Vocal Cord Irradiation: Image Guided Intensity Modulated Hypofractionated Radiation Therapy for T1a Glottic Cancer: Early Clinical Results. International journal of radiation oncology, biology, physics. 2015;93(2):337-43.
8 Tiong AH, S.H.; O'Sullivan, B.; Mallick, I.; Kim J.; Dawson L.A.; Cho J.; Ringash J.; Bayley A.; Hope A.; Yu E.; Breen S.; McNiven A.; Gilbert R.; Xu W.; Waldron J. Outcome following IMRT for T2 glottic cancer: the potential impact of image-guidance protocols on local control. J Radiat Oncol. 2014(3):267–75
9 van Asselen B, Raaijmakers CP, Lagendijk JJ, Terhaard CH. Intrafraction motions of the larynx during radiotherapy. International journal of radiation oncology, biology, physics. 2003;56(2):384-90.
10 Hamlet S, Ezzell G, Aref A. Larynx motion associated with swallowing during radiation therapy. International journal of radiation oncology, biology, physics. 1994;28(2):467-70.
11 Leonard RJ, Kendall KA, McKenzie S, Goncalves MI, Walker A. Structural displacements in normal swallowing: a videofluoroscopic study. Dysphagia. 2000;15(3):146-52.
12 Dantas RO, Kern MK, Massey BT, Dodds WJ, Kahrilas PJ, Brasseur JG, et al. Effect of swallowed bolus variables on oral and pharyngeal phases of swallowing. The American journal of physiology. 1990;258(5 Pt 1):G675-81.
13 Bradley JA, Paulson ES, Ahunbay E, Schultz C, Li XA, Wang D. Dynamic MRI analysis of tumor and organ motion during rest and deglutition and margin assessment for radiotherapy of head-and-neck cancer. International journal of radiation oncology, biology, physics. 2011;81(5):e803-12.

Optimizing MRI sequences and images for MRI-based stereotactic radiosurgery treatment planning

Somayeh Taghizadeh, MS[1,2,4]; Cecille Labuda, Ph.D.[4]; Claus Chunli Yang, Ph.D.[1]; Bart Morris, MS[1]; Madhava R. Kanakamedala, M.D.[1]; Srinivasan Vijayakumar, M.D.[1]; Roberto Rey-Dios, M.D.[1,3]; William N. Duggar, M.S.[1]; Edward Florez, Ph.D.[2]; Ali Fatemi, Ph.D.[1,2]

[1] Department of Radiation Oncology, University of Mississippi Medical Center, Jackson, MS, USA
[2] Department of Radiology, University of Mississippi Medical Center, Jackson, MS, USA
[3] Department of Neurosurgery, University of Mississippi Medical Center, Jackson, MS, USA
[4] National Center for Physical Acoustics and Department of Physics and Astronomy, University of Mississippi, Jackson, MS, USA

Abstract

Aim
Development of MRI sequences and processing methods for the production of images appropriate for direct use in stereotactic radiosurgery (SRS) treatment planning.

Background
MRI is useful in SRS treatment planning, especially for patients with brain lesions or anatomical targets that are poorly distinguished by CT, but its use requires further refinement. This methodology seeks to optimize MRI sequences to generate distortion-free and clinically relevant MR images for MRI-only SRS treatment planning.

Materials and methods
We used commercially available SRS MRI-guided radiotherapy phantoms and eight patients to optimize sequences for patient imaging. Workflow involved choice of correct MRI sequence(s), optimization of the sequence parameters, evaluation of image quality (artifact free and clinically relevant), measurement of geometrical distortion, and evaluation of the accuracy of our offline correction algorithm.

Results
CT images showed a maximum deviation of 1.3 mm and minimum deviation of 0.4 mm from true fiducial position for SRS coordinate definition. Interestingly, uncorrected MR images showed maximum deviation of 1.2 mm and minimum of 0.4 mm, comparable to CT images used for SRS coordinate definition. After geometrical correction, we observed a maximum deviation of 1.1 mm and minimum deviation of only 0.3 mm.

Conclusion
Our optimized MRI pulse sequences and image correction technique show promising results; MR images produced under these conditions are appropriate for direct use in SRS treatment planning.

Introduction

Magnetic resonance imaging (MRI) is the imaging modality of choice for target definition for stereotactic radiotherapy due to its superior soft tissue resolution, not only in the brain but in extracranial sites as well. In cases of intracranial stereotactic radiotherapy, MRI can also be used for dosimetry planning as the brain is considered homogenous. The advantages of using MRI alone[1] in intracranial SRS include avoiding systematic errors that may occur due to CT-MRI registration, and the risks associated with ionizing radiation exposure from CT scans.

Although MR images have excellent soft-tissue contrast, allowing superior visualization of gross tumor volume

The concepts and information presented in this paper are based on research and are not commercially available.

[1] The product is not commercially available. Radiotherapy where MR data is the only imaging information is ongoing research. The concepts and information presented in this article are based on research and are not commercially available. Its future availability cannot be ensured. Not for clinical use.

(GTV) and organs at risk (OAR), the geometrical distortion of MR images is one of the main obstacles to their optimal use in SRS planning; therefore, CT is still commonly used to obtain geometrically accurate reference images. CT images also provide electron density data and can be registered with MR images for geometrical distortion correction [1].

One motivation for the solo use of MRI for SRS planning is most centers' use of Tissue Maximum Ratio (TMR) tables for SRS treatment planning; these tables do not account for brain tissue inhomogeneity. This technique is faster, simpler, and no information about tissue electron density is required; however, many groups are working on synthetic CT images which make use of MR images.

With the use of synthetic CT images derived from MR images, we still retain the option to use convolution/superposition algorithms in SRS treatment planning for more accurate dose calculation.

The geometrical accuracy of MR images can be compromised by both system- and patient-specific distortions. System related distortion is mainly caused by main magnetic field (B_0) inhomogeneity and gradient nonlinearity. These effects are reproducible for each scanner, but vary for different field strengths and vendors, and must be evaluated during the commissioning process. [2]

The B_0 of an MRI is measured in parts per million (ppm) over a diameter of spherical volume (DSV) extending out from the scanner isocenter. We expect a nominal homogeneity of 1.1 ppm across a 37 cm DSV for a 1.5T scanner; this corresponds to a frequency offset of 70.2 Hz. This offset resonance frequency along the frequency encoding direction creates discrepancies in signal location which manifest as image intensity variation and distortion.

Gradient coils localize the MRI signal within the body to visualize the anatomy. Many newly developed fast MRI pulse sequences have been used in the clinic to minimize artifacts due to motion and provide patient comfort. These sequences need strong gradients, but there is always a tradeoff between gradient strength and linearity. The gradient linearity error should be less than 2% of the gradient strength over a 40 cm diameter of spherical volume (DSV) [3].

Modern MRI scanners have homogenous magnetic fields; therefore, the main source of image distortion is gradient non-linearity. Most vendors provide post-processing offline correction algorithms, which are applied in two and three dimensions [4–6], but still there is a need to evaluate the efficiency of such corrections with periodic phantom measurements.

Patient-specific distortion originates from the effect of tissue magnetic susceptibility (χ) on the local magnetic field. These random distortions are not corrected by standard MRI post-processing correction algorithms and need careful consideration, especially when MR images are being used as a sole source for SRS planning. Patient-specific distortion may cause tumor and normal tissue dislocation, significant error in stereotactic coordinates definition, and MRI-CT co-registration difficulty, especially when targets in the brain are very close to air cavities, or away from the magnet isocenter.

Several methods have been suggested to correct patient-specific distortion. One is an increase in receiver bandwidth, but increasing the bandwidth leads to a reduction in the signal-to-noise ratio (SNR) [7, 8]. Another is to use manual and high-order shimming to render the magnetic field more locally homogenous by minimizing the effect of magnetic susceptibility, chemical shift and eddy current through the region of scan [9–11]. Finally, a B_0 field map, very commonly used in functional MRI (fMRI) studies, has been used to correct for geometrical distortions in echo planar imaging (EPI) images [12]. All of these methods have their own advantages and disadvantages, but for our purposes, to be used in the SRS clinic, their accuracy, clinical flow, and compatibility with SRS treatment planning system are vital factors [12].

Different MRI sequences (different contrasts) are being used for GTV and OAR contouring in SRS treatment planning systems. Depending on the clinical protocol implemented, CT and MRI images may initially define the stereotactic coordinates, and then CT image set is co-register rigidly to MR images to correct for any noticeable geometrical distortion. Importantly, to accurately correct MR images they must be registered deformably not rigidly with CT images which is not an option with the current SRS Gamma Knife treatment planning systems. Specifically, distortions are more noticeable when MR images are collected in 2D mode, with different slice thickness, in-plane or through-plane spatial resolution compared with CT, and in partial head scans in oblique mode.

In this paper, we describe our methodology to generate distortion-free and clinically relevant MR images for MRI-only SRS treatment planning. We tested our method first on commercial phantoms, and then on patients. Our methodology involves choosing the right MRI sequences, optimizing the sequence parameters, evaluating the image quality, determination of clinical relevance, correction for geometrical distortion, and finally, testing the accuracy of our offline correction algorithm.

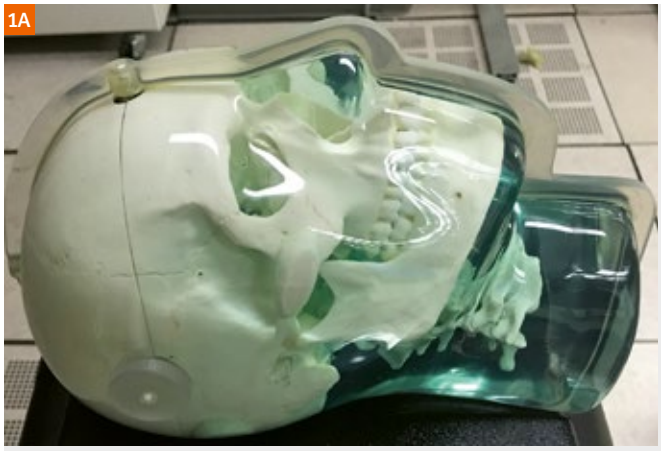

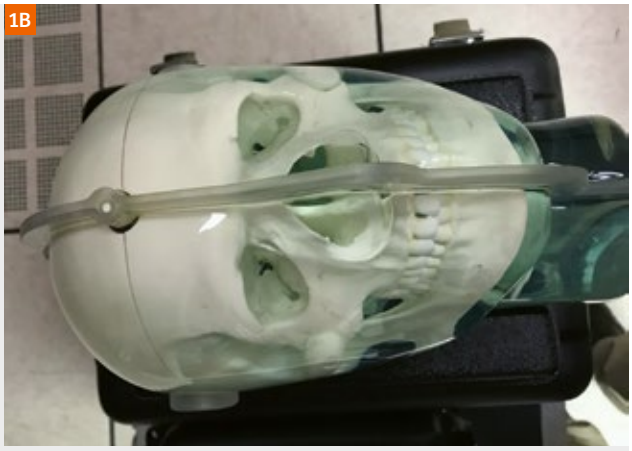

Figure 1:
CIRS Simulated MRI distortion head phantom.

Figure 2:
Quasar GRID^{3D} image distortion phantom: "small phantom".

Materials and methods

We have recently installed the new Leksell Gamma Knife® Icon™ stereotactic radiosurgery treatment unit[2] (Elekta AB, Stockholm, Sweden), and the MAGNETOM Aera 1.5T Radiotherapy (RT) edition (Siemens Healthcare, Erlangen, Germany) at our institute. The SRS committee consists of three physicists, one radiologist, two radiation oncologists, and one neurosurgeon; together, it is responsible for choosing the clinically relevant MRI pulse sequences for SRS treatment planning.

[2] The information shown herein refers to products of 3rd party manufacturer's and thus are in their regulatory responsibility. Please contact the 3rd party manufacturer for further information.

MR images are used for treatment of brain metastasis, pituitary/parasellar lesions, acoustic neuroma, trigeminal neuralgia, and arteriovenous malformation (AVM). The SRS committee look at specific MRI pulse sequences with unique contrast and resolution to be used for GTV and OAR contouring in a SRS treatment planning system (Gamma Plan, Version 11.0.3). Generally, the MRI sequences are mostly 3D, no slice gap for 2D sequences, and isotropic in spatial resolution. Immobilization devices are chosen to be MRI-compatible based on vendor report and the reports of other centers. Most importantly, the committee choses the optimal head RF coil(s) for high sensitivity, better SNR, less RF deposition (SAR effect), and retention of enough space to fit the SRS frame, MRI localizer, and RF head adaptor into the scanner.

We initially optimized MRI sequences to have high SNR and provide artifact-free images and then focused on correcting geometric distortion using two commercially available MRI compatible phantoms: a simulated head phantom (CIRS, MRI distortion phantom, Model 603A, Norfolk, VA, USA) (Fig. 1), and a Quasar GRID^{3D} (Modus Medical, London, ON, Canada) (Fig. 2). We then collected data from six SRS patients.

The MRI scanner was commissioned based on our proposed quality control procedure for SRS treatment planning using commercial and standard phantoms. As part of our commissioning process, we evaluated a system distortion map (B_0 inhomogeneity and gradient non-linearity) over a large field-of-view (37 cm) using body coil and Quasar MRID^{3D} (Modus medical, London, ON, Canada) geometrical distortion phantoms (Fig. 3).

We applied system- and patient-specific distortion correction along the frequency encoding direction. The system distortion map was derived using Quasar GRID^{3D}

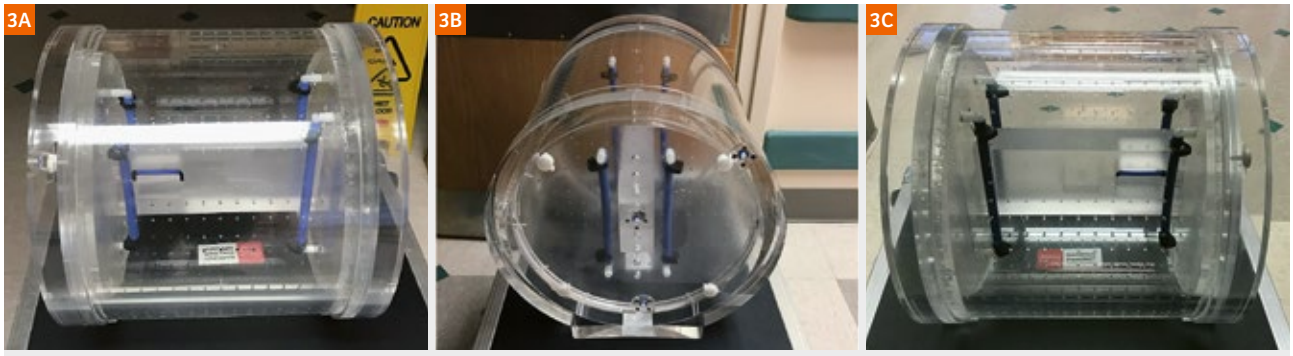

Figure 3:
Quasar MRID[3D] geometrical distortion phantom: "big phantom".

Sequence/contrast	Parameters	Disease
Axial 3D T1-weighted MPRAGE	< 1 ma 1 x 1 x 1 mm³, TR/TE = 2200/2.91 ms, FA = 15°, 300 Hz/pixel m	Brain metastasis, pituitary/parasellar lesions, acoustic neuroma/schwannoma, trigeminal neuralgia, AVM
Axial 3D T2-weighted SPACE	0.9 x 0.9 x 1 mm³, TR/TE = 1400/184 ms, FA = 120°, 345 Hz/pixel	Pituitary/parasellar lesions, acoustic neuroma/schwannoma, AVM
Axial 2D T2 TSE	0.9 x 0.9 x 1 mm³, TR/TE = 3990/89 ms, FA = 120°, 300 Hz/pixel	Pituitary/parasellar lesions, acoustic neuroma/schwannoma, trigeminal neuralgia

Table 1: MRI pulse sequences used in the phantom studies.

software and our in-house MATLAB code to obtain the "system displacement map". For patient-specific correction we used a field map technique using a multi-echo Gradient echo sequence to calculate the complex phase difference map with receiver bandwidth and isotropic resolution, close to other MRI sequences.

Phantom study

We scanned the commercial phantoms with SRS frames and localizers on our MRI unit and evaluated the quality of the acquired MR images for artifacts and geometrical fidelity for the purpose of SRS planning. Geometrical distortion was evaluated for different MRI sequences using the GRID[3D] phantom, and our offline geometrical distortion correction method was validated using phantoms both qualitatively and quantitatively.
The GRID[3D] MRI was scanned with all sequences and parameters summarized in Table 1. All MRI sequences were run with automated shimming over entire phantoms. The central frequency was adjusted manually, and the shimming currents set to apply the highest linear gradient field to each imaging axis. The bandwidths were chosen to be close to 330 Hz/pixel for all MRI sequences to minimize artifacts due to magnetic susceptibility and sub-optimal shimming.

Next, high-resolution magnitude and phase images were acquired to reconstruct the field maps after automated shimming over the entire head phantom volume (Multi-echo gradient echo, $TE_1/TE_2/TR$ = 2.46/11.98/12 ms, 335 Hz/pixels, approximately 1 mm³ isotropic sagittal, 3D acquisition, Rx/Tx RF head coil). The phase images were complex divided and unwrapped to produce field maps (in-house software, IDL 8.2, Boulder, CO, USA and Mathworks, Natick, MA, USA). The conversion of field map to displacement map was found using

$$d = \Delta\chi \cdot f_0 \cdot \frac{\left(\frac{b}{B_0}\right)}{\Delta f}$$

where $\Delta\chi$ is the pixel size, f is the Larmor frequency, Δf is the receiver bandwidth per pixel, B_0 is the magnetic field, and b is the magnetic distortion. The final displacement map was calculated based on the field map and machine displacement maps. The machine displacement map applied to all MRI images in all directions, and the field map applied only in the frequency encoding direction.

For this procedure to be consistent, MR images and displacement map should have the same spatial resolution

and pixel bandwidth, which was checked using an open-source AFNI software package. The region of interest measures 14 x 13 x 11 cm^3, and within it are 2002 vertex locations, the positions of which are known within 0.1 mm. The phantom accurately and reproducibly mounts securely to the Leksell Coordinate SRS Frame G at a known position, and fits within both the Leksell MR and CT boxes.

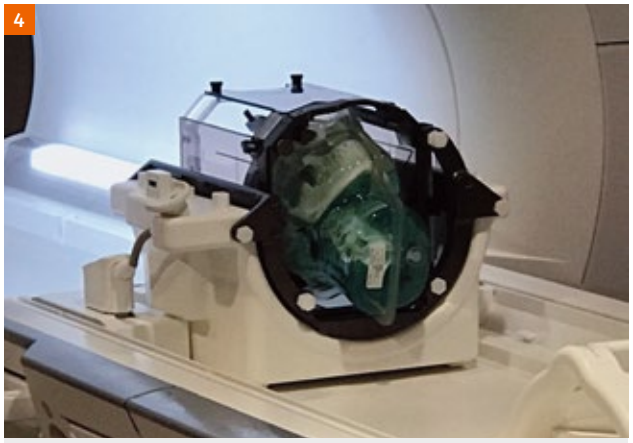

Figure 4:
CIRS head phantom with SRS frame and all localizer devices.

We evaluated geometrical distortion for each sequence using the phantom vendor's software. The software automatically finds the fiducials and locates each vertex within the phantom in 3D. The software determined the X, Y, Z, and dr (absolute distance from isocenter) deviations of the location of each vertex in the image. There after we corrected all the MR images using our offline correction and compare with non-corrected images.

Next, the CIRS phantom with SRS frame and localizer (Fig. 4) was scanned by MRI pulse sequences with parameters listed in (Table 1) and by CT (Siemens Healthcare, 120 kV, 462 mA, 512 x 512 x 306 mm^3, exposure time 615 ms).

We used MIM software (MIM software Inc., Cleveland, OH, USA) to evaluate MR corrected image quality for artifacts and geometrical accuracy compared with CT. The corrected MR images were rigidly fused with CT (Fig. 5). The geometrical accuracy of the corrected and non-corrected MR images was evaluated visually (checker board) and quantitatively by looking at the fusion matrix statistical parameters such as normalized mutual information (NMI), Pearson correction coefficient (PCC) and root mean square difference (RMSD).

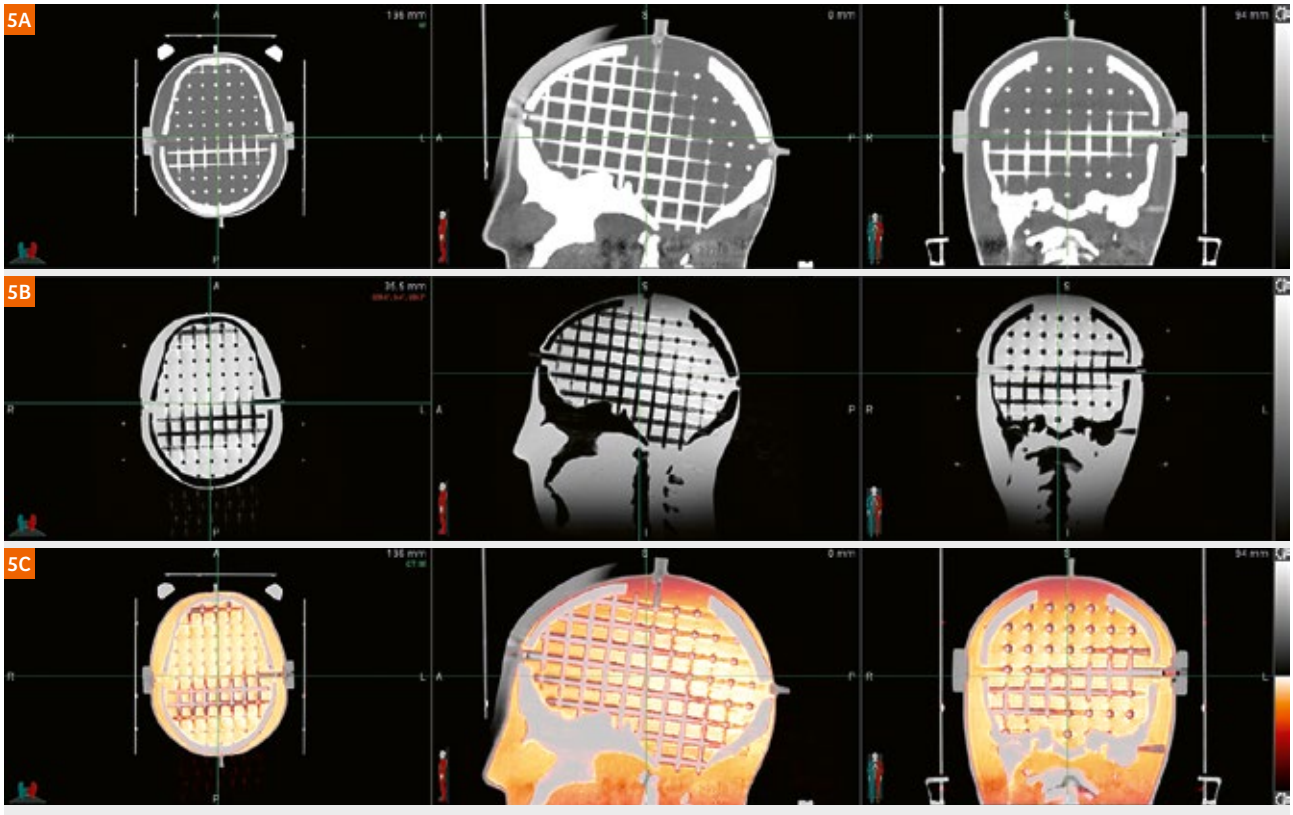

Figure 5:
Phantom corrected MRI images fused with CT images. **(5A)** CT image, **(5B)** corrected MRI images, **(5C)** fused MRI and CT images.

Patient study

Eight patients (four with a SRS frame and four with a mask) under an IRB-approved protocol were MRI and CT scanned for SRS treatment. For all patients, we used a 3D post-contrast axial MPRAGE MRI pulse sequence for stereotactic coordinate definition and tumor delineation because of its geometrical accuracy and high SNR. The other MRI sequence has been used for organ at risk (OAR) contouring. The MR images were presented to the radiologist, neurosurgeon and physicist for review of image quality, clinical relevance, and overall scanning time.

The geometrical distortion of MR images before and after correction has been validated qualitatively (checker board) in MIM software with respect to reference CT (Fig. 6). We also imported corrected and non-corrected MR images in GammaPlan and evaluated the stereotactic coordinates definition accuracy relative to CT.

Results

The data from the GRID^{3D} phantom indicate the best MRI geometrical accuracy was obtained with a 3D SPACE sequence. We measured maximum deviation on, (X, Y are in plane and Z along the magnet), (X-direction = 1.8 mm, Y-direction = 2.9 mm, Z-direction = 2.7 mm) and 0.7 mm on axial plane at 7.5 cm from isocenter in Z direction. We noticed significant artifacts at the boundary, which we speculate were due to magnetic susceptibility from the phantom, SRS frame and localizer. The 3D MPRAGE axial (the reference images) were superior in SNR, and appeared to be less prone to artifacts due to magnetic susceptibility, but showed higher distortion compared to 3D SPACE. We measured maximum deviation (X-direction = 1.9 mm, Y-direction = 2.8 mm, Z-direction = 3.4 mm) and 1.4 mm and 1.3 mm in axial plane beyond 5 cm from isocenter in Z direction. The 2D TSE sequence had an acceptable SNR and was free of artifacts, but as we expected from 2D sequences, the geometrical distortion is extreme, and we do not recommend its use for this application. We measured maximum deviation (X-direction = 2.2 mm, Y-direction = 4.1 mm, Z-direction = 7 mm) and average of 1.8 mm in axial plane beyond 2 cm from isocenter.

After geometrical correction was applied to all images, they were reevaluated. We observed overall improvement in both 3D MPRAGE and 3D SPACE images, but no significant improvement in images obtained using 2D TSE.

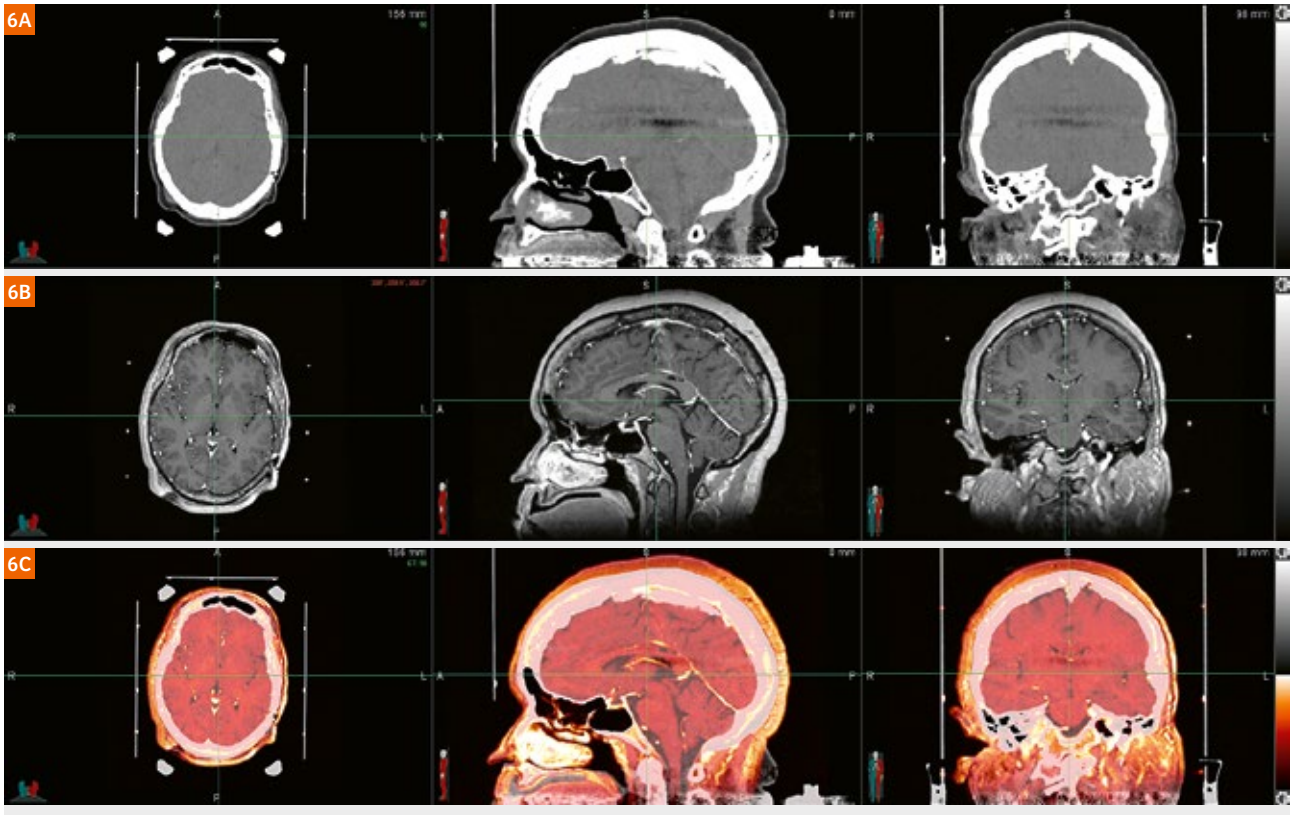

Figure 6:
Patient corrected MRI images fused with CT images. **(6A)** CT image, **(6B)** corrected MRI images, **(6C)** fused MRI and CT images.

For 3D MPRAGE the changes were minor, and there was improvement in axial plane from 0.8 mm to 0.7 mm for 3 cm and 4 cm from isocenter in Z-direction. 3D SPACE images showed significant improvement; overall 3% correction (average of 0.3 mm) for all points. The TSE images do not show significant improvement which proved that our correction algorithm need to be applied to each slice separately and re-evaluated.

After the MR images from CIRS phantom were reviewed by the SRS committee for image quality, the fusion matrix statistical parameters of fused geometrically corrected and non-corrected MRI and CT images were also examined, and are summarized in Table 2.

The patient MR images were reviewed by the SRS committee for image quality and clinical relevance for SRS treatment planning. All images were geometrically corrected based on the same algorithm used in the phantom studies; we evaluated our patient MRI geometrical accuracy qualitatively (Fig. 6) and quantitatively. First, MIM software was used to rigidly register MR-CT images, visually inspect the checker board display, and calculate the fusion matrix statistics (NMI, PCC and RMSD).

We observed maximum changes of 2% in RMSD for all images and no significant changes in the remaining parameters without significant change. SRS treatment planning software was then used to calculate the stereotactic coordinate accuracy, comparing corrected MR images to original non-corrected MR images and CT images. The CT images showed the maximum (1.3 mm) and minimum of (0.4 mm) deviation from true fiducial position for SRS coordinate definition. Interestingly the non-corrected MR images showed maximum (1.2 mm) and minimum of (0.4 mm) deviation which is comparable to using CT images for SRS coordinate definition. After geometrical correction we observed the maximum (1.1 mm) and minimum (0.3 mm) deviations.

Discussion

In this work, we demonstrated the methodology and clinical flow to optimize MRI sequences to generate images for MRI only SRS treatment planning. A 3D MPRAGE sequence with high bandwidth generated artifact-free images on both phantoms and patients with acceptable geometrical distortion even prior to offline geometrical correction. Therefore, this sequence is recommended as the main sequence for SRS planning purposes. The 3D axial T2 SPACE has shown significant artifacts in both phantom and patient studies, possibly a result of SRS frame magnetic susceptibility and some wrapping artifacts in the axial plane. In patient studies, we managed to correct for wrapping by putting 60% oversampling in a frequency encoding direction at the expense of increasing scanning time, or using 3D coronal T2 SPACE. Another alternative would be use of a 2D Turbo Spin Echo (TSE) sequence with zero gap.

CIRS Phantom	Non-corrected	Corrected
	T1 MPRAGE, BW = 300 Hz/pixel	
Normalized mutual information (NMI)	0.241	0.241
Pearson correction coefficient (PCC)	0.563	0.565
Root mean square difference (RMSD)	1133.192	1132.724
	T2 SPACE, 780 Pixel/Hz, axial	
Normalized mutual information (NMI)	0.171	0.171
Pearson correction coefficient (PCC)	0.486	0.488
Root mean square difference (RMSD)	824.748	824.719
	T2 TSE, axial, BW = 254	
Normalized mutual information (NMI)	0.563	0.563
Pearson correction coefficient (PCC)	0.563	0.563
Root mean square difference (RMSD)	0.563	0.563

Table 2: The statistical parameters for corrected and non-corrected MRI images fused with CT image.

One of the main obstacles to the direct use of MR images in treatment planning is their geometrical **distortion**[1]. In general, SRS treatment planning systems use rigid MRI-CT co-registration, which does not correct for any residual MR image distortion. This correction could be accomplished by using both deformable and rigid co-registration algorithms to create distortion-free MR images if CT images are used as a **reference**[3]. We propose offline MR images distortion correction be used with SRS treatment planning systems.

Our correction technique is based on communitive effects of system distortion and patient distortion (e.g. head geometry, tissue type, SRS frame material, localizer box). Although most of the literature on MR images distortion correction suggest visual checking, this method does not provide any quantitative information, especially when only a rigid co-registration algorithm is **used.**[6] Therefore, we proposed two methods to evaluate the MR images distortion quantitatively reporting

1. co-registration accuracy statistics between corrected MR and CT images using, normalized mutual information (NMI), Pearson correction coefficient (PCC) and root mean square difference (RMSD) and
2. the stereotactic coordinate definition accuracy in SRS treatment planning system for corrected MR images compared with original non-corrected MR and CT images for both phantom and patient studies. We propose to speed up the correction process by using 3D T1 post MPRAGE images as reference, and then registering these images with those acquired using other sequences. These images can then be used for SRS treatment planning.

The two main sources of MRI geometrical distortion (systematic and induced magnetic susceptibility) [12, 13] have been evaluated in a head-sized region by using a commercial MRGRID^{3D} phantom. After applying the vendor's post processing correction for gradient non-linearity, the images' geometrical distortion is within expectations, especially at the central region of magnet (head size), with an average of 0.7 mm – 0.8 mm for 3D SPACE and 3D MPRAGE respectively. To achieve a sub-millimeter accuracy for SRS planning the residual gradient nonlinearity and patient specific distortions (tissue and frame induce magnetic susceptibility) still need to be corrected [14–15].

Patient-specific geometrical distortions have been corrected using a field map technique with the receiver bandwidth close to our MRI pulse sequences to avoid or minimize the inherited distortion in our field maps.

MR images were acquired with high receiver bandwidth, high readout gradient and optimized SNR. Auto shimming was applied for the entire head volume to avoid any distortion due to microscopic gradients, especially if manual shimming was applied for smaller volumes (air cavities and sinuses). There are many studies indicating that susceptibility-induced displacements are most noticeable in **air cavities**[15], and our results from displacement mapping confirmed this statement. Based on our parameters, which we used for SRS MRI sequences (close to 350 Hz/pixel, approximately 1 mm^3 isotropic voxels), for axial 3D MPRAGE the maximum displacement was calculated as up to 1.4 mm.

For our next study, we will investigate the geometrical and dosimetric accuracy of MRI-only SRS planning compared to the combined MR/CT image-based planning. There are also opportunities to use corrected MRI-derived CT images (synthetic CT) for MRI-only SRS planning. This opens up the potential to benefit from both soft tissue contrast and inhomogeneity correction using convolution-based dose calculation algorithms for accurate SRS treatment planning accounting for heterogeneity in patient anatomy. Such research projects have implications beyond SRS treatment planning; this methodology could have potential applications in focal brain external beam radiotherapy (IMRT) using synthetic CT images. We strongly believe that the benefits of superior soft tissue contrast from MRI will affect the course of highly conformal image-guided radiotherapy.

Conclusions

In conclusion, our optimized MRI pulse sequences and corrected images show promising results, producing MR images appropriate for direct use for SRS treatment planning. These results highlight the urgency of design and implementation of commercial image processing software compatible with SRS treatment planning systems for MRI distortion correction, and more importantly, multi-modality image registration and post-response tumor evaluation. The commonplace presence of an MRI expert to optimize MRI sequences and establish MRI QA programs in departments of radiation oncology is an inevitable outcome. These findings have implications for SRS planning and MR-guided radiotherapy in general.

Acknowledgments

The authors would like to thank Siemens Healthineers and especially all members of the MRI service crew for fruitful discussions.

References

1 Schmidt MA, Payne GS. Radiotherapy planning using MRI. Phys Med Biol 2015; 60:R323–61.
2 Baldwin LN, Wachowicz K, Thomas SD, Rivest R, Fallone BG. Characterization, prediction, and correction of geometric distortion in 3 T MR images. Med Phys 2007; 34:388–99.
3 Jezzard P. The physical basis of spatial distortions in magnetic resonance images. In: Bankman IN, editor. Handbook of medical image processing and analysis, 2nd ed. Amsterdam: Elsevier; 2009, p. 499–514.
4 Walker A, Liney G, Metcalfe P, Holloway L. MRI distortion: considerations for MRI based radiotherapy treatment planning. Australas Phys Eng Sci Med 2014; 37:103–13.
5 Wang D, Doddrell DM, Cowin G. A novel phantom and method for comprehensive 3-dimensional measurement and correction of geometric distortion in magnetic resonance imaging. Magn Reson Imaging 2004; 22:529–42.
6 Doran SJ, Charles-Edwards L, Reinsberg SA, Leach MO: A complete distortion correction for MR images: I. gradient warp correction. Phys Med Biol 2005; 50:1343–61.
7 Reinsberg SA, Doran SJ, Charles-Edwards EM, Leach MO. A complete distortion correction for MR images: II. rectification of static-field inhomogeneities by similarity-based profile mapping. Phys Med Biol 2005; 50:2651–61.
8 Jezzard P, Balaban RS. Correction for geometric distortion in echo planar images from B0 field variations. Magn Reson Med 1995; 34:65–73.
9 Reber PJ, Wong EC, Buxton RB, Frank LR. Correction of off resonance related distortion in echo planar imaging using EPI based field maps. Magn Reson Med 1998; 39:328–30.
10 Robson MD, Gore JC, Constable RT. Measurement of the point spread function in MRI using constant time imaging. Magn Reson Med 1997; 38:733–40.
11 Zeng H, Constable RT. Image distortion correction in EPI: comparison of field mapping with point spread function mapping. Magn Reson Med 2002; 48:137–46.
12 Harris R, Wesbey G. Artifacts in magnetic resonance imaging. In Kressel HY editor. Magnetic Resonance Annual 1988, New York: Raven Press; 1988, p. 71–112.
13 Heilbrun MP: Image-guided stereotactic surgery: Adjunct technical advances. In Wilkins RH, Rengachary SS editors. Neurosurgery Update II. New York: McGraw-Hill; 1991, p. 373–78.
14 Kondziolka D, Dolan EJ, Tasker RR: Functional stereotactic surgery and stereotactic biopsy using a magnetic resonance imaging directed system: Results and comparisons to CT guidance. Stereotact Funct Neurosurg 1990; 54/55:237 (Abstract)
15 Matakos A, Balter J, Cao Y. Estimation of geometrically undistorted B0 inhomogeneity maps. Phys Med Biol 2014; 59:4945–59.

Contact

Ali Fatemi, Ph.D., MCCPM
Senior physicist, Director of MR Guided Radiotherapy Lab, Assistant professor
Departments of Radiology and Radiation Oncology
University of Mississippi Medical Center

2500 North State Street
Jackson, Mississippi 39216
USA
Phone: +1 (601)345-0135
afatemi@umc.edu

TREATMENT: Improved therapy response assessment in metastatic brain tumors

Endre Grøvik, Ph.D.; Ingrid Digernes, M.Sc.; Line Nilsen, Ph.D.; Kyrre Eeg Emblem, Ph.D.

Oslo University Hospital, Department for Diagnostic Physics, Oslo, Norway

TREATMENT is an observational study addressing the need for knowledge and adequate diagnostic biomarkers in the response assessment of patients with brain metastasis. Reliable response assessment will be highly relevant in the coming years given the introduction of next-generation cancer drugs, including immunotherapy. This project uses advanced Magnetic Resonance Imaging (MRI) and Vessel Architecture Imaging (VAI) to better understand the response to traditional stereotactic radiosurgery (SRS) and immunotherapy.

Attributed in large by advances in treatment of primary tumors, there has been an explosive growth in patients with metastatic cancer over the last decades. Metastatic cancers, primary cancer that spread to another place in the body, are usually observed in bone, liver, lung and brain. The prognoses of patients with metastases to the brain are dismal with an overall survival from first diagnosis ranging from months up to a few years. The primary goal of treatment is to control tumor growth and standard-of-care usually includes chemotherapy, radiotherapy and surgery, depending on diagnosis and extent of disease. These treatments have been somewhat successful in the sense that treated patients live longer than untreated, but at the cost of clinical and neurological deficits. To this end, patients with metastatic disease represent an increasing demand on health care resources, especially for repeated therapeutic interventions and diagnostic work-up. The associated diagnostic methods for assessing treatment response follow the criteria formulated by the Response Assessment in Neuro-Oncology (RANO) working group, and are based on measuring the size of the enhancing lesion on contrast-enhanced T1-weighted MRI. Here, a complete or partial response requires a complete or ≥ 50% reduction in the enhancing target lesion for a minimum of 4 weeks with stable or reduced levels of vasogenic edema on MRI and sustained or reduced use of corticosteroids. Unfortunately, these criteria are challenged by high heterogeneity within-, and between, metastatic subtypes for both treatment response and time to progression.

The introduction of immunotherapy is widely viewed as the greatest advancement in cancer treatment in the last decade. Immunotherapy is the collective term of multiple treatment methods that uses the body's own immune system to help fight cancer. This is a highly promising therapy option that is now finally coming of age with some astonishing results of prolonged patient survival, especially for malignant melanomas. Unlike traditional cancer treatment, where the criteria for response assessment are given by RANO, the criteria for assessing treatment response after immunotherapy are not yet established.

Current diagnostic methods have been proven insufficient because the response to immunotherapy does not necessarily result in a simple reduction of tumor size. This treatment method, and even stereotactic radiosurgery (SRS) may, however, induce a temporary inflammatory reaction that manifest as increased contrast-enhancement and enlarged tumor volume on MRI. Figure 1 illustrates this problem after treatment by the means of SRS, but a similar response may also occur following immunotherapy.

The TREATMENT project will address the growing need for targeted biomarkers and gain important new knowledge on the diagnosis and the underlying response mechanisms following cancer treatment, thus paving the way for a more reliable response assessments. The study includes two patient cohorts, with brain metastasis from non-small-cell lung cancer (NSCLC) and malignant

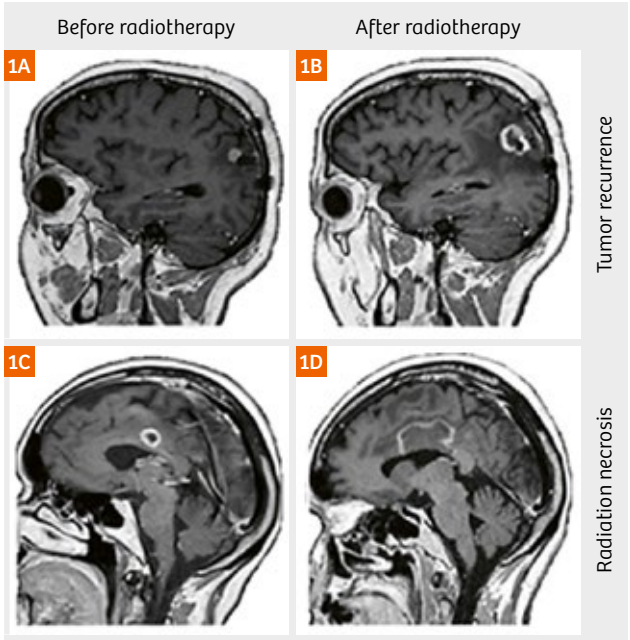

Figure 1: Radiation necrosis vs. true progression. Conventional MRI data from OUH showing a patient with a brain metastasis from breast cancer before treatment **(1A)** and with histologically confirmed tumor progression at 12 months **(1B)**. In contrast, MRI data of a patient with a non-small cell lung cancer metastasis **(1C)** show radiation necrosis at 15 months **(1D)** that eventually disappear. With dismal survival prognosis, biomarkers of early response are critical to differentiate patients responding to therapy from those patients who only suffer the side effects.

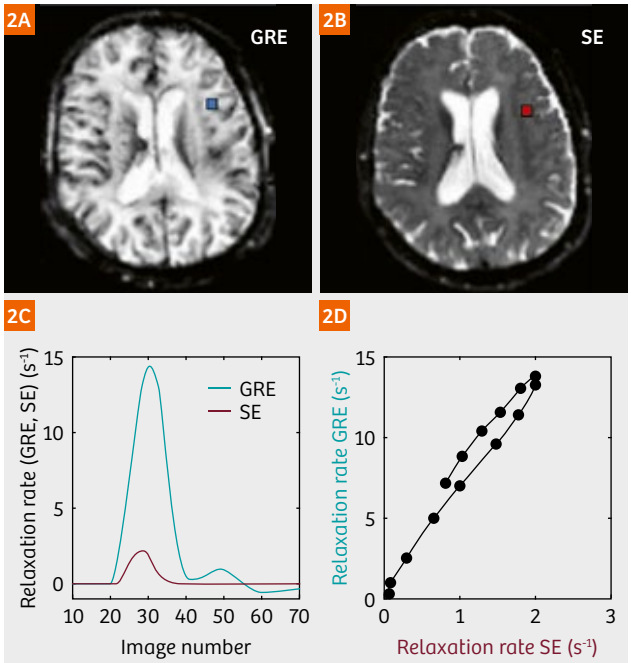

Figure 2: Vessel Architectural Imaging (VAI). The VAI-method is based on repeated acquisition of pair-wise gradient-echo (GRE) and spin-echo (SE) data. The acquisition are done simultaneously, thus yielding the corresponding relaxation rates from GRE (**2C**, blue curve) and SE (**2C**, red curve) following a single injection of contrast agent. The resulting vortex **(2D)** is characterized by its size, shape and direction, and reflects the underlying vascular properties in the target tissue.

melanomas (mal.mel). A unique diagnostic pipeline has been established at the Norwegian sites contributing to the project, in which targeted monitoring of patients with brain metastases receiving SRS and immunotherapy, are performed with repeated MRI every third month or until the patients is deemed unfit for continued imaging. Included in the MRI protocol is the new paradigm in cancer diagnostics; *Vessel Architecture Imaging* (VAI), developed by group leader Emblem and his associates at Massachusetts General Hospital [1]. This method uses repeated acquisition of pair-wise gradient-echo (GRE) and spin-echo (SE) data (Fig. 2). The GRE- and SE-data are acquired independently and simultaneously after the administration of a contrast agent by using Echo Planar Imaging (EPI) with the following key parameters: TR = 1500 ms, TE_{GE}(NSCLC/mal.mel) = 13/30 ms and TE_{SE} = 104 ms. The acquired matrix size was 120 x 90 over a 240 x 180 (NSCLC) and 260 x 195 field of view with a scan time of 2 minutes and 36 seconds. The VAI-data are acquired pending a routine post-contrast T1-weigted image-series, thus utilizing this interim period without increasing the total scan time.

The general principle behind the VAI-method is based on the observation that GRE and SE signal-response following the administration of contrast agents depend on the microvascular properties of the tissue. By plotting the par-wise GRE- and SE-data, the resulting parametric curve forms a vortex. This vortex is then characterized by its size, shape and direction, which are further used to obtain measurements of the vessel size or caliber, vessel type and oxygen saturation (ΔSO_2). Consequently, these novel measurements reveal new information regarding blood vessel types, vascular function and supply not obtainable by conventional dynamic MRI methods. The VAI-method has previously shown that anti-angiogenic treatment can improve microcirculation and oxygen saturation, as well as reduce vessel caliber in patients with primary brain tumors. Consequently, the TREATMENT study aim to investigate whether VAI may help identify patients benefiting from SRS and immunotherapy, as well as reveal underlying mechanisms that can contribute to new insights, and thus advancing response assessment. Given that the presence of sufficient oxygen is an important factor for achieving a good response to SRS

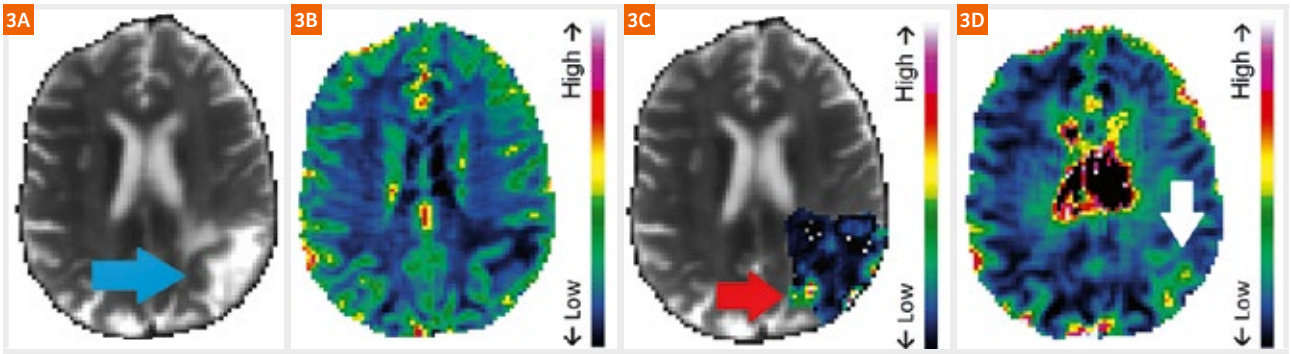

Figure 3: Advanced pre-therapy MRI data of a brain metastasis from non-small-cell lung cancer.
Based on conventional **(3A)** and even traditional perfusion MRI **(3B)**, it is difficult to depict tissue heterogeneity within the tumor region (blue arrow). In contrast, distinct regions of pathologic vasculature (**3C**; red arrow) and vessel calibers (**3D**; white arrow) are observed using VAI.

(and immunotherapy), it is hypothesized that VAI can identify patients with tumor profiles susceptible to such treatment (Fig. 3).

The two patient cohorts are further separated into different subgroups, depending on whether they receive SRS with or without combined immunotherapy. The goal is to include 100 patients with up to three-year follow-up. The initial finding suggests that immunotherapy directly affects the blood vessels and vascular function in the tumors, indicating that the new and advanced MRI methods may provide new insight into biological mechanisms relevant for response assessments.

As of today, clinicians face the challenge of insufficient and unreliable response assessment, and the criteria for identifying the correct response at an early stage in the treatment process is not obvious in many cancer patients. Consequently, there is an urgent need to improve the monitoring and management of cancer, especially with the introduction of new treatment methods. Hence, the radiological response criteria should not solely be based on the change in tumor size, but also reflect vascular and metabolic changes. The research group at OUH hopes that the TREATMENT project may aid overcome these challenges in the years to come.

References

1 Emblem et al. Vessel architectural imaging identifies cancer patient responders to anti-angiogenic therapy. Nat. Med. 19:1178–1183 (2013).

Contact

Kyrre Eeg Emblem, Ph.D.
Oslo University Hospital

Sognsvannsveien 20
0372 Oslo
Norway
kemblem@ous-hf.no

The TREATMENT project (2016–2019) is led by Kyrre Eeg Emblem, Ph.D., at the Department for Diagnostic Physics, Oslo University Hospital (OUH), Norway, who has established a research group including oncologists, radiologists, radiographers, study nurses and physicists from OUH. In addition to being a national venture with contributors from OUH, Sørlandet Hospital Kristiansand (Birger Breivik, MD), Østfold Kalnes Hospital (Dag Ottar Sætre, MD) and St. Olav Hospital / Norwegian University of Science and Technology (NTNU) (Asta Håberg, MD), the project also collaborates with Massachusetts General Hospital and Dana-Farber Cancer Institute in Boston, MA, USA, both affiliated with Harvard Medical School, as well as the UT Southwestern Medical Centre in Dallas, TX, USA, and the University Medical Centre in Groningen, The Netherland. Managed by Emblem and his group at OUH, the researchers aim to acquire new knowledge that may help improve the current response assessment of traditional therapy and next-generation cancer drugs.

Spectroscopic MRI for dose-escalated radiation therapy

Saumya S. Gurbani, MS[1,2]; Eric Mellon, M.D., Ph.D.[3]; Brent Weinberg, M.D., Ph.D.[4]; Eduard Schreibmann, Ph.D.[1]; Andrew A. Maudsley, Ph.D.[5]; Lee A. D. Cooper, Ph.D.[2,6]; Hui-Kuo G. Shu, M.D., Ph.D.[1]; Hyunsuk Shim, Ph.D.[1,2,4]

[1] Department of Radiation Oncology, Winship Cancer Institute of Emory University, Atlanta, GA, USA
[2] Department of Biomedical Engineering, Emory University and Georgia Institute of Technology, Atlanta, GA, USA
[3] Department of Radiation Oncology, University of Miami Miller School of Medicine, Miami, FL, USA
[4] Department of Radiology and Imaging Sciences, Emory University School of Medicine, Atlanta, GA, USA
[5] Department of Radiology, University of Miami Miller School of Medicine, Miami, FL, USA
[6] Department of Biomedical Informatics, Emory University School of Medicine, Atlanta, GA, USA

Glioblastoma is the most common primary adult brain tumor in the US, with over 10,000 cases diagnosed each year [1]. The current standard of care for these patients is the removal of as much tumor as possible via neurosurgery followed by radiation therapy (RT) and concurrent chemotherapy (typically with temozolomide) [2–5]. Two radiation doses are commonly used. High dose radiation (60 Gy) is targeted to the post-surgical cavity and residual disease defined by areas of enhancement on T1-weighted gadolinium contrast-enhanced (CE-T1w) MRI, which represents highly aggressive tumor which has broken through the blood-brain barrier. A lower dose of radiation (51–54 Gy) is targeted towards areas of hyperintensity on T2-weighted fluid-attenuation inversion recovery (FLAIR) MRI [6], which corresponds to a combination of tumor and non-tumor pathologies, including inflammation and edema [7]. The enhancing regions on CE-T1w are also the target for surgical resection, and with advancements in neurosurgical methods, there is often little enhancement left; thus, much of the high dose radiation ends up treating the empty cavity.

Despite aggressive treatment, glioblastomas continue to progress and recur – sometimes inside the initial 60 Gy isodose cloud but often times outside it – within months of treatment, and median survival remains poor at 15 months [8, 9]. Two conclusions can be drawn from this poor prognosis. First, radiation doses higher than 60Gy may be needed for long-term control of disease. Second, we are unable to fully identify all at high risk for tumor recurrence at the time of treatment. Currently, the NRG Oncology cooperative group is evaluating the

The concepts and information presented in this paper are based on research and are not commercially available.

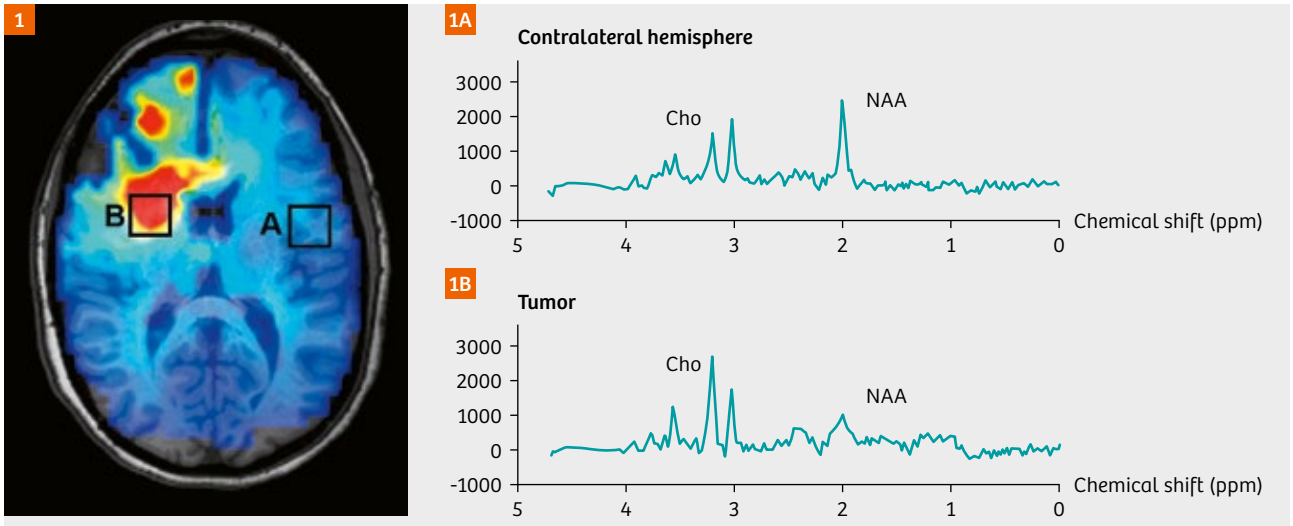

Figure 1: sMRI identifies metabolic changes in glioblastoma in vivo.
Spectroscopic MRI (sMRI) is a quantitative modality that measures whole-brain endogenous metabolism in vivo. In patients with glioblastoma, the ratio of choline to N-acetylaspartate (Cho/NAA) differentiates healthy tissue **(1A)** from tumor **(1B)** due to a simultaneous increase in choline and a decrease in N-acetylaspartate.

risks and benefits of dose escalating radiation to 75 Gy in conjunction with standard concurrent and adjuvant temozolomide [10], but using conventional targeting with much of the boosted dose going to the resection cavity. Therefore, even if successful locally, there are concerns that conventionally targeted doses will fail to control regions at high risk for recurrence elsewhere in the brain – after all, we can't treat what we can't identify. Thus, better approaches are needed for targeting both enhancing and non-enhancing tumor to maximize the benefits of high dose radiation.

Proton spectroscopic magnetic resonance imaging (sMRI) is an advanced imaging modality that enables in vivo acquisition of 3D whole-brain volumes of metabolic activity [11, 12] (Fig. 1). Two metabolites are of particular interest in patients with glioblastoma. Choline-containing compounds (Cho), the building blocks of the cell membrane, increase in proliferating tumor cells; N-acetylaspartate (NAA), a biomarker found in healthy neurons, diminishes due to neuronal displacement and death due to glial infiltration [11, 13]. It has been previously shown via histological correlation that the ratio of Cho to NAA is significantly elevated in glioblastoma due to the opposing changes in these metabolites. In particular, a two-fold increase in Cho/NAA compared to normal-appearing tissue in contralateral white matter was able to correctly identify tumor in 100% of cases, even when tissue samples were biopsied from regions outside of contrast-enhancement per CE-T1w or even FLAIR hyperintensity [14]. This indicates that conventional MRI targeting does not identify all of the areas of tumor at high risk of recurrence. Further, a simulation study of patients with newly-diagnosed glioblastoma identified that two-fold elevated Cho/NAA in addition to CE-T1w identified future sites of disease recurrence in nine out of eleven patients [15].

However, using sMRI data in clinical care requires specialized software, a local MR spectroscopist with years of expertise, and many hours of manual imaging processing. This has been a barrier to the clinical validation and implementation of sMRI. To address this need, we have developed a software package which seeks to automate these tasks and facilitate the use of sMRI to target RT in a multisite clinical study. The Brain Imaging Collaboration Suite (BrICS) is a web-based software designed specifically to integrate sMRI with clinical imaging, enabling physicians to evaluate metabolic activity, review underlying spectra on a voxel-basis, and delineate target volumes for RT planning [16]. BrICS consists of two components: a central server which performs computationally intensive image processing, and a lightweight browser client that can run on any modern computer or tablet. Users can also co-register sMRI volumes with other clinical imaging via a DICOM importer, and edit contours manually similar to standard software, with the advantage that all data are stored centrally and readily shared to other users. A demo is available for public use at our group's website at **https://brainimaging.emory.edu.**

To assess the feasibility of sMRI-guided radiation therapy across institutions in a group setting, a multisite clinical study has begun at Emory University, the Johns Hopkins University, and the University of Miami, with the goal of enrolling a total of 30 patients with glioblastoma. In this trial, patients will first undergo surgical resection of their tumor. Next, prior to RT, patients will receive a sMRI scan on a Siemens Healthineers 3T scanner (either a MAGNETOM Prisma with a 32-channel head coil, or a MAGNETOM Skyra with a 20-channel head coil) using a 15 minute echo planar spectroscopic imaging (EPSI) pulse sequence. Shimming is performed using the built-in auto shim capability of the Siemens Healthineers scanners. Raw EPSI data is transformed into a 3D spatial

2

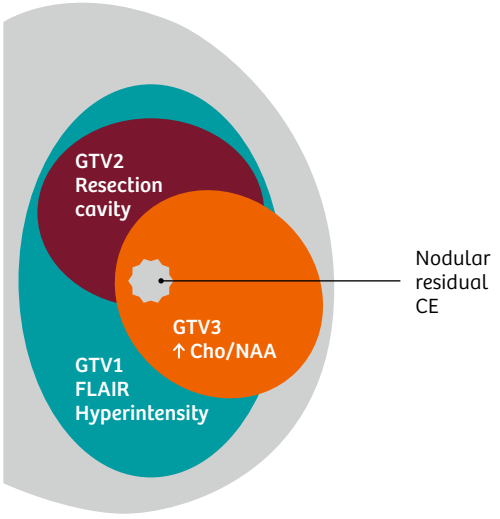

Target	Definition	Dose
GTV3	Cho/NAA ≥ 2x normal white matter + residual contrast enhancement; no margin added	75 Gy
GTV2	Contrast enhancing tissue + resection cavity, per standard of care; 5 mm margin added	60 Gy
GTV1	Hyperintensity on FLAIR MRI, per standard of care; 5 mm margin added	51 Gy

Figure 2: Clinical study schematic.
In this clinical study, patients with glioblastoma will receive standard of care treatment (GTV1 and GTV2), plus an additional boost to regions of metabolic activity and to any residual contrast-enhancing lesions that could not be surgically resected (GTV3).

volume and metabolite concentrations are calculated via spectral fitting using the MIDAS software suite, developed by Dr. Maudsley's team at the University of Miami [17, 18].

Patients in this multisite study will also receive standard-of-care imaging in the clinic, including CE-T1w and FLAIR MRI; these volumes are then imported into BrICS where all volumes are co-registered into the same image space. Contours including areas of brain with a two-fold increase in Cho/NAA and residual contrast enhancement are generated as target volumes. MR spectroscopists from at least two institutions review the underlying spectra within the contours to ensure data are of good enough quality to use. A neuroradiologist then reviews and edits the contours to ensure accuracy. Finally, the Cho/NAA and contrast-enhancing contours are merged to form a single target volume, and two radiation oncologists make final edits based on anatomy and dose safety concerns (i.e. removing voxels near organs-at-risk), and validate the volume. The final contour is exported from BrICS into the radiation therapy planning system by a board-certified medical physicist at the treating institution, and is targeted for an escalated dose of 75 Gy. The remainder of the brain is treated per the standard of care – 60 Gy to the surgical cavity and 51 Gy to areas of FLAIR hyperintensity (Fig. 2). All doses are delivered over 30 fractions (five days per week x six weeks, same as standard of care). We present in Figure 3 the contours from our first patient, who underwent our dose escalated protocol in late 2017. As can be seen, there was only a small, nodular residual contrast-enhancing island on the surgical cavity, but the Cho/NAA abnormality expanded much further out, including regions that crossed the midline of the brain, which is not apparent even in the FLAIR volume.

In addition to RT planning, sMRI can also be used to monitor the metabolic response to treatment. Traditional monitoring modalities, such as FLAIR and DWI, are sensitive to physiologic changes arising from radiation and chemotherapy, e.g. hyperintensity in FLAIR due to an inflammatory response to treatment. sMRI, however, is robust to these other physiologic changes and remains specific in the detection of proliferative disease. For this reason, we acquire a second sMRI two weeks into RT to evaluate whether sMRI could be an early marker of treatment response enabling adaptations of RT during the therapy course.

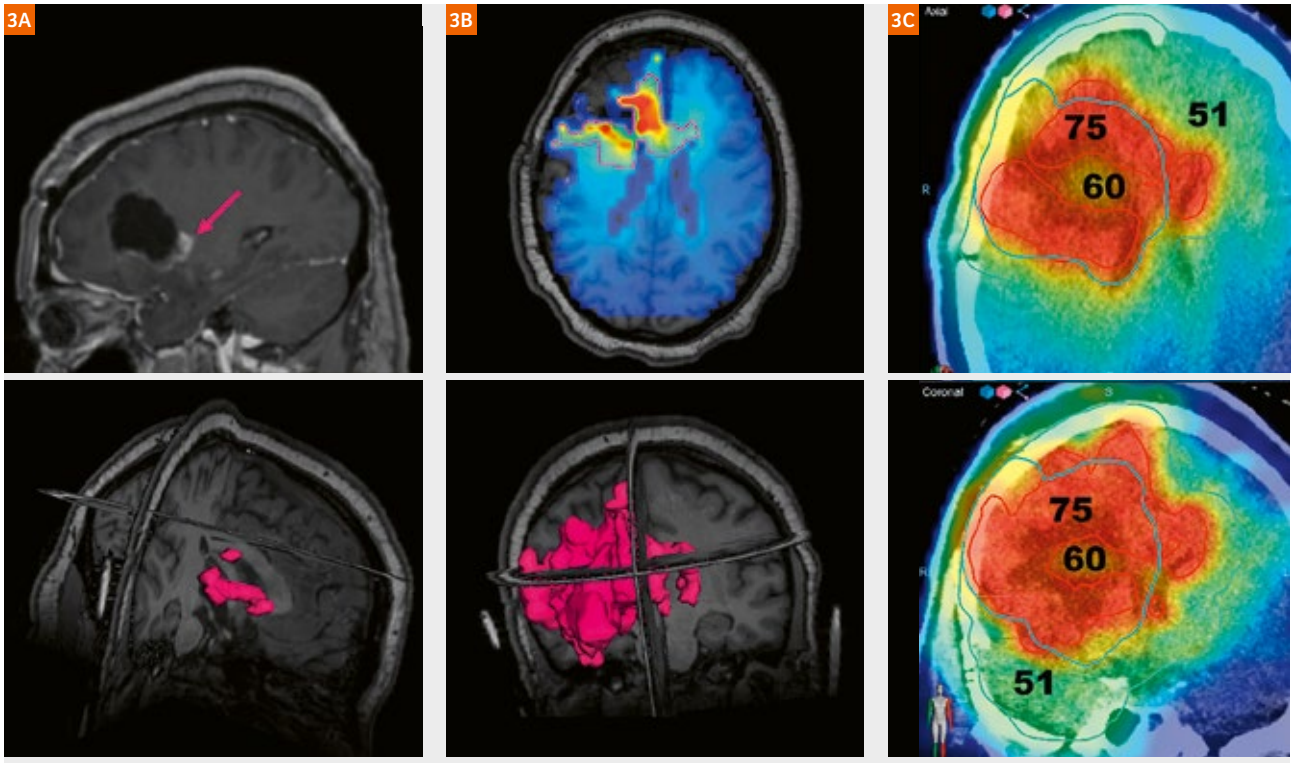

Figure 3: Sample patient.
The first patient enrolled in this trial was a young, 21-year-old female, who underwent surgical removal of her glioblastoma. **(3A)** While only a small nodule of contrast-enhancing tumor remains, **(3B)** sMRI identifies a much larger region of metabolically active tumor which should be targeted for high dose radiation. **(3C)** The escalated dose RT plan was successfully carried out on a standard linear accelerator setup.

In this project, we are able to bring together the multi-institutional team via a web app to collectively manage a patient's RT plan. This is normally very difficult to do (just try getting multiple physicians in the same room on a busy clinic day, let alone from different cities!), but with the BrICS infrastructure, we are able to accomplish the entire pipeline, from scanner to final treatment plan, in less than two days per patient. Furthermore, the addition of the EPSI sequence is only 15 minutes, and data processing is as fast as other modalities such as PET; the majority of the two days comes from treatment planning. In the past, sMRI has been shown to be a useful modality in identifying metabolically active tumor, but has thus far been difficult to incorporate into clinical practice due to the complexity of integrating its information with clinical volumes and the necessity of having spectroscopy experts available locally. BrICS solves these issues, enabling clinicians from multiple institutions to use sMRI for treating patients. Through our initial ongoing clinical study, we seek to validate the feasibility of sMRI guidance for radiation therapy, and to pave the way for a future consortium-level trial to ultimately assess the benefits of targeting high-risk, metabolically active tumor.

In conclusion, we seek to develop sMRI technology to improve radiation therapy guidance in patients with glioblastoma. Our hope is that by making whole brain sMRI more accessible for clinical decision-making and treatment decisions through an easy-to-use, collaborative web application, we can improve patient outcomes and drive future of state-of-the-art glioblastoma care.

References

1 Ostrom QT, Gittleman H, Liao P, Rouse C, Chen Y, Dowling J, et al. CBTRUS Statistical Report: Primary Brain and Central Nervous System Tumors Diagnosed in the United States in 2007–2011. Neuro Oncol. 2014;16(suppl_4):iv1-iv63. doi: 10.1093/neuonc/nou223.

2 Wen PY, Macdonald DR, Reardon DA. Updated response assessment criteria for high-grade gliomas: response assessment in neuro-oncology working group. Journal of Clinical Oncology. 2010. doi: 10.1200/JCO.2009.26.3541.

3 Stupp R, Hegi ME, Gilbert MR. Chemoradiotherapy in malignant glioma: standard of care and future directions. Journal of Clinical Oncology. 2007. doi: 10.1200/JCO.2007.11.8554.

4 Stupp R, Hegi ME, Mason WP, van den Bent MJ. Effects of radiotherapy with concomitant and adjuvant temozolomide versus radiotherapy alone on survival in glioblastoma in a randomised phase III study: 5-year analysis of the EORTC-NCIC trial. The lancet oncology. 2009.

5 Stupp R, Mason WP, Bent VMJ. Radiotherapy plus concomitant and adjuvant temozolomide for glioblastoma. N Engl J Med. 2005 Mar 10;352(10):987-96. doi: 10.1056/NEJMoa043330.

6 Wernicke AG, Smith AW, Taube S, Mehta MP. Glioblastoma: Radiation treatment margins, how small is large enough? Practical radiation oncology. 2016;6(5):298-305.

7 Tsuchiya K, Mizutani Y. Preliminary evaluation of fluid-attenuated inversion-recovery MR in the diagnosis of intracranial tumors. AJNR Am J Neuroradiol. 1996 Jun-Jul;17(6):1081-6.

8 Stupp R, Hegi ME, Gilbert MR, Chakravarti A. Chemoradiotherapy in malignant glioma: standard of care and future directions. J Clin Oncol. 2007;25(26):4127-36. doi: 10.1200/JCO.2007.11.8554.

9 Stupp R, Hegi ME, Mason WP, van den Bent MJ, Taphoorn MJB, Janzer RC, et al. Effects of radiotherapy with concomitant and adjuvant temozolomide versus radiotherapy alone on survival in glioblastoma in a randomised phase III study: 5-year analysis of the EORTC-NCIC trial. Lancet Oncol. 2009;10(5):459-66. doi: 10.1016/S1470-2045(09)70025-7.

10 RTOG. Randomized Phase II Trial of Hypofractionated Dose-Escalated Photon IMRT or Proton Beam Therapy Versus Conventional Photon Irradiation With Concomitant and Adjuvant Temozolomide in Patients With Newly Diagnosed Glioblastoma. Radiat Ther Oncol Gr NRG-BN001 Protoc Inf. 2014.

11 Law M. MR spectroscopy of brain tumors. Topics in Magnetic Resonance Imaging. 2004;15(5):291-313. doi: 10.1097/00002142-200410000-00003.

12 Maudsley AA, Domenig C, Sheriff S. Reproducibility of serial whole-brain MR Spectroscopic Imaging. NMR in Biomedicine. 2010. doi: 10.1002/nbm.1445.

13 Law M, Cha S, Knopp EA, Johnson G, Arnett J, Litt AW. High-grade gliomas and solitary metastases: differentiation by using perfusion and proton spectroscopic MR imaging. Radiology. 2002;222(3):715-21. doi: 10.1148/radiol.2223010558.

14 Cordova JS, Shu H-KG, Liang Z, Gurbani SS, Cooper LAD, Holder CA, et al. Whole-brain spectroscopic MRI biomarkers identify infiltrating margins in glioblastoma patients. Neuro Oncol. 2016;18(8):1180-9. doi: 10.1093/neuonc/now036.

15 Cordova JS, Kandula S, Gurbani S, Zhong J, Tejani M, Kayode O, et al. Simulating the Effect of Spectroscopic MRI as a Metric for Radiation Therapy Planning in Patients with Glioblastoma. Tomography : a journal for imaging research. 2016;2(4):366-73. doi: 10.18383/j.tom.2016.00187. PubMed PMID: PMC5241103.

16 Gurbani SS, Schreibmann E, Sheriff S, Cooper LAD, Shu HKG, Holder CA, et al. A Software Platform for Collaborative Radiation Therapy Planning Using Spectroscopic MRI. International Journal of Radiation Oncology • Biology • Physics. 2017;99(2):E667. doi: 10.1016/j.ijrobp.2017.06.2209.

17 Maudsley AA, Domenig C, Govind V, Darkazanli A, Studholme C, Arheart K, et al. Mapping of brain metabolite distributions by volumetric proton MR spectroscopic imaging (MRSI). Magn Reson Med. 2009;61(3):548-59. doi: 10.1002/mrm.21875.

18 Sabati M, Sheriff S, Gu M, Wei J, Zhu H, Barker PB, et al. Multivendor implementation and comparison of volumetric whole-brain echo-planar MR spectroscopic imaging. Magn Reson Med. 2015;74(5):1209-20. doi: 10.1002/mrm.25510.

Contact

Hyunsuk Shim, Ph.D.
Department of Radiation Oncology
Winship Cancer Institute of Emory University

1701 Uppergate Drive
Atlanta, GA 30322, USA
hshim@emory.edu

From the left: Hui-Kuo Shu, MD, PhD (Radiation Oncologist); Saumya Gurbani, MS (MD/PhD student); Hyunsuk Shim, PhD; Brent Weinberg, MD, PhD (Neuroradiologist); Eduard Schreibmann, PhD (Medical Physicist).

MyoMap quantification of myocardial toxicity following concurrent chemoradiotherapy for esophageal carcinoma

Simon Tang[1,2,3]; Eng-Siew Koh[1,2,3]; Robba Rai[1,2,3]; James Otton[4]; Mark Lee[2,3]; David Tran[4]; Lois Holloway[1,2,3,5]; Liza Thomas[3,5]; Benjamin Schmitt[6]; Gary Liney[1,2,3]

[1.] Ingham Institute of Applied Medical Research, Liverpool, NSW, Australia
[2.] Cancer Therapy Centre, Liverpool Hospital, NSW, Australia
[3.] University of New South Wales, NSW, Australia
[4.] Department of Cardiology, Liverpool Hospital, NSW, Australia
[5.] University of Sydney, NSW, Australia
[6.] Siemens Healthineers, Sydney, Australia

Introduction

Crude rates of symptomatic cardiac toxicity in esophageal carcinoma are reportedly 10.8% [1]. Cardiac manifestations including clinical findings such as pericardial effusion, arrhythmia, ischemia and cardiomyopathy, typically occur between 4 to 24 months following thoracic radiation [2, 3]. Subclinical manifestations including declines in mean ejection fraction [4] and perfusion abnormalities and wall ischemia [5] have also been noted at shorter time scales between 1–3 months. Hatakenaka *et al.* [6], using cardiac MRI, have demonstrated focal wall motion abnormalities in conjunction with changes in heart rate, stroke volume and left ventricular (LV) end-diastolic volume index following concurrent chemoradiation.

In-house quantification of longitudinal and cross sectional reproducibility *in vivo* has shown variation of 3.9% for T1 measurements, and a 15.2% variation in T2 measurements [7].

This paper presents the case of a patient treated with concurrent chemoradiation for esophageal cancer, where cardiac tissue properties were assessed by cardiac mapping (MyoMaps) longitudinally prior to, 6 weeks following, and 12 months following treatment.

Patient case

This 67-year-old male patient was diagnosed with a Stage IB T2N0M0 squamous cell carcinoma of the lower esophagus, following investigations for unexplained dysphagia and weight loss. He was otherwise fit and well, with the cardiac risk factors of hypercholesterolaemia and a smoking history.

The concepts and information presented in this paper are based on research and are not commercially available.

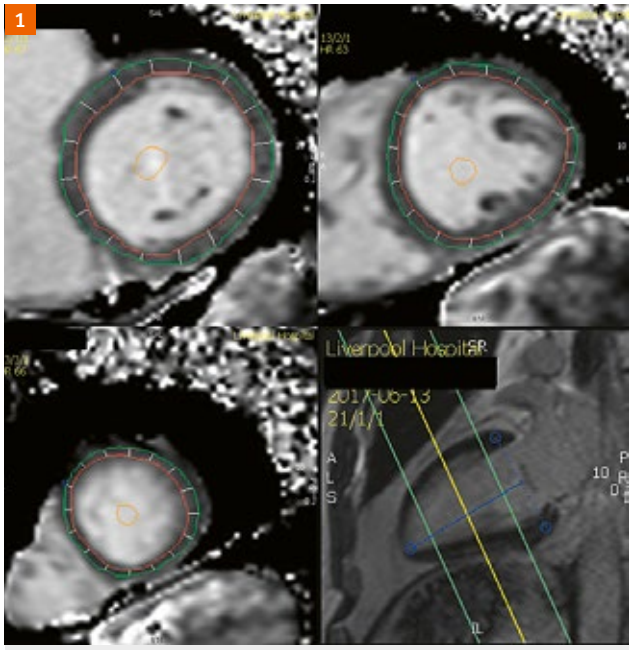

Figure 1:
Native T1 MyoMap with myocardium contoured at the basal, mid, and apical levels.

T1 Relaxation: Measure of longitudinal signal recovery. This is elevated in the presence of edema or fibrosis.

T2 Relaxation: Measure of transverse signal decay. This is elevated in the presence of edema.

ECV: Is a measure of myocardial extracellular volume. It is elevated in myocardial fibrosis.

Table 1: Definitions.

He subsequently underwent chemoradiation 50 Gy / 25 fractions using a 3D conformal technique, with concurrent carboplatin/paclitaxel chemotherapy. He experienced no cardiac symptoms during or following his treatment.

Image acquisition

The patient underwent three separate cardiac MRI scans, one prior to, 6 weeks, and 12 months following completion of his chemoradiation. A clinical modified look locker inversion (MOLLI) sequence[1] was used to generate myocardial short axis T1 maps (MyoMaps, Siemens Healthcare, Erlangen, Germany), pre- and 15 minutes post-administration of a gadolinium-based contrast agent, as well as T2 maps (MyoMaps) at 3 Tesla. T1, T1 post-contrast and T2 relaxation times of the LV were acquired with MRI mapping software (cvi42, v4.5, Circle Software). Extracellular volume (ECV) was derived from the myocardial portioning coefficient (λ), adjusting for hematocrit. Values were recorded in the American Heart Association (AHA) 17 segment model [8]. Figure 1 illustrates the delineation of the left ventricle on a native T1 map. Definitions and possible significance of various MRI sequences are outlined in Table 1.

Radiotherapy dose calculations

Corresponding RT doses to the AHA LV segments were determined from contours outlined in the cardiac axes on reformatted planning CT images in Oncentra Brach Treatment Planning v4.5.2 (Elekta AB, Stockholm, Sweden), before being imported into Mim v6.77 (Mim Software, Beachwood, OH, USA) for dosimetric readout. Mean heart dose, mean LV dose, and mean segmental doses were reported, with mean heart doses having known associations with radiation induced cardiac toxicity [9].

Results

The mean heart dose was 28.82 Gy. The mean LV dose was 14.16 Gy. Mean dose delivered to the left ventricular segments was heterogeneous, with segments 3 and 4 receiving 30 Gy or more, segments 2 and 5 receiving 20 Gy or more, and segments 6, 10, and 11 receiving 10 Gy or more. Figure 2 reports the dose delivered in a bulls-eye format.

Changes in the T1, T2, and ECV values are as illustrated in Figures 3–5, with the changes depicted on the MyoMaps represented in Figures 6 and 7. Visually there appears to be an increase in native T1 values post chemoradiation, most prominently 12 months following treatment, which is occurring most prominently in segments 3, 4, and 5, which correspondingly received the highest radiation doses. A 12 month increase in T2 relaxation time values was also seen, although occurring more globally throughout the left ventricle. The ECV percentage transiently increased 6 weeks following chemoradiation.

[1] WIP, the product is currently under development and is not for sale in the US and in other countries. Its future availability cannot be ensured.

2

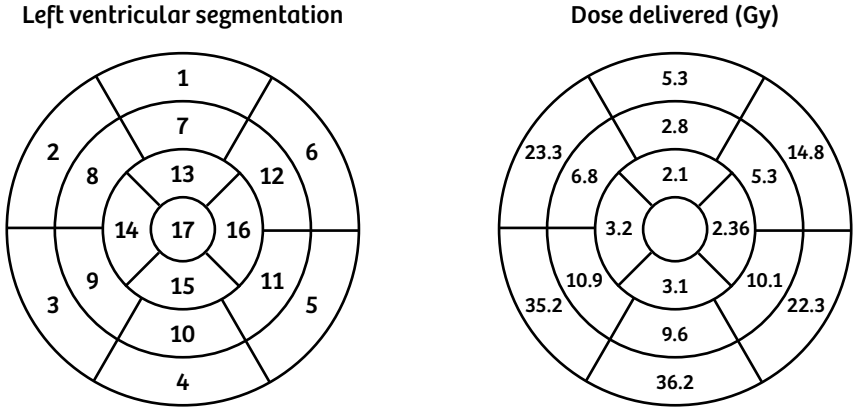

1. basal anterior
2. basal anteroseptal
3. basal inferoseptal
4. basal inferior
5. basal inferolateral
6. basal anterolateral
7. mid anterior
8. mid anteroseptal
9. mid inferoseptal
10. mid inferior
11. mid inferolateral
12. mid anterolateral
13. apical anterior
14. apical septal
15. apical inferior
16. apical lateral
17. apex

Figure 2: Dose delivered to the left ventricular segments represented in a bulls-eye format.

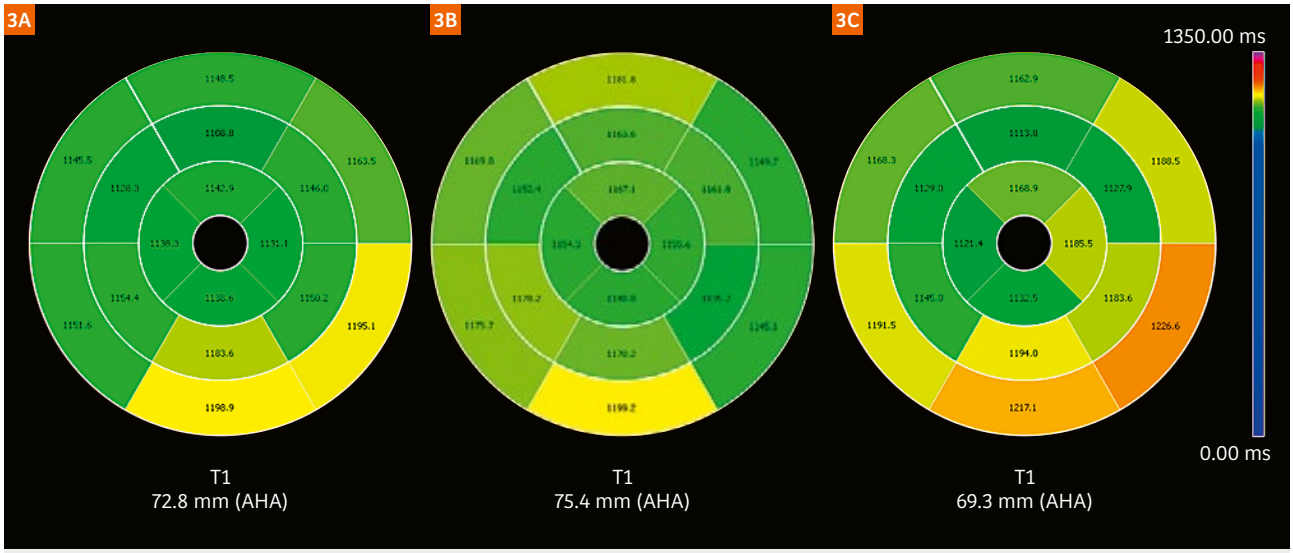

Figure 3: T1 values

(3A) Pre-treatment
(3B) 6 week post-treatment
(3C) 12 months post treatment time points respectively

Elevation of T1 values were most pronounced at 12 months in the basal segments.

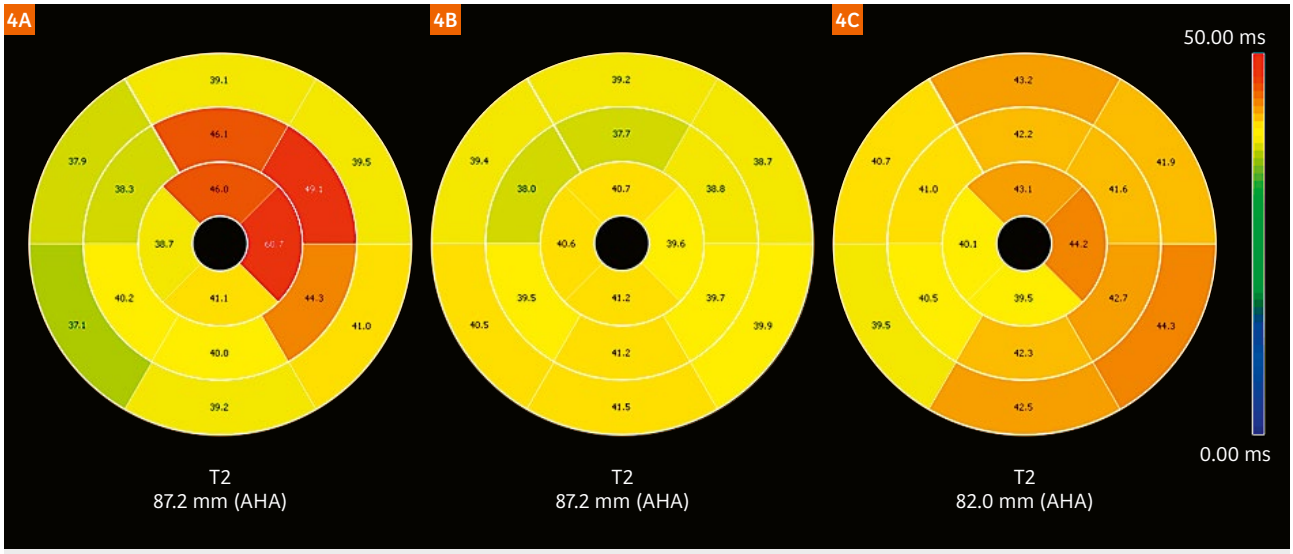

Figure 4: T2 values

(4A) Pre-treatment
(4B) 6 week post-treatment
(4C) 12 months post treatment time points respectively

Elevation of the segments 7, 11, 12, 13, and 16 in 4A are artefactual from errors in motion correction. An increase in T2 values in predominantly the basal segments was seen after 12 months.

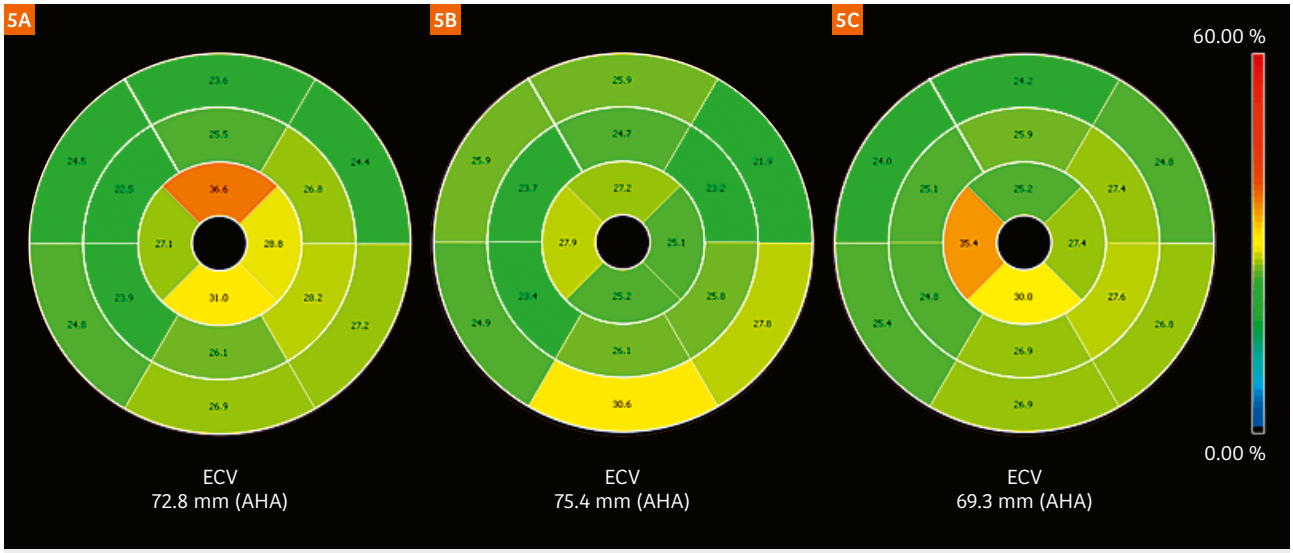

Figure 5: ECV values

(5A) Pre-treatment
(5B) 6 week post-treatment
(5C) 12 months post treatment time points respectively

A subtle increase in ECV is seen the basal segments following treatment, however returns to baseline at 12 months.

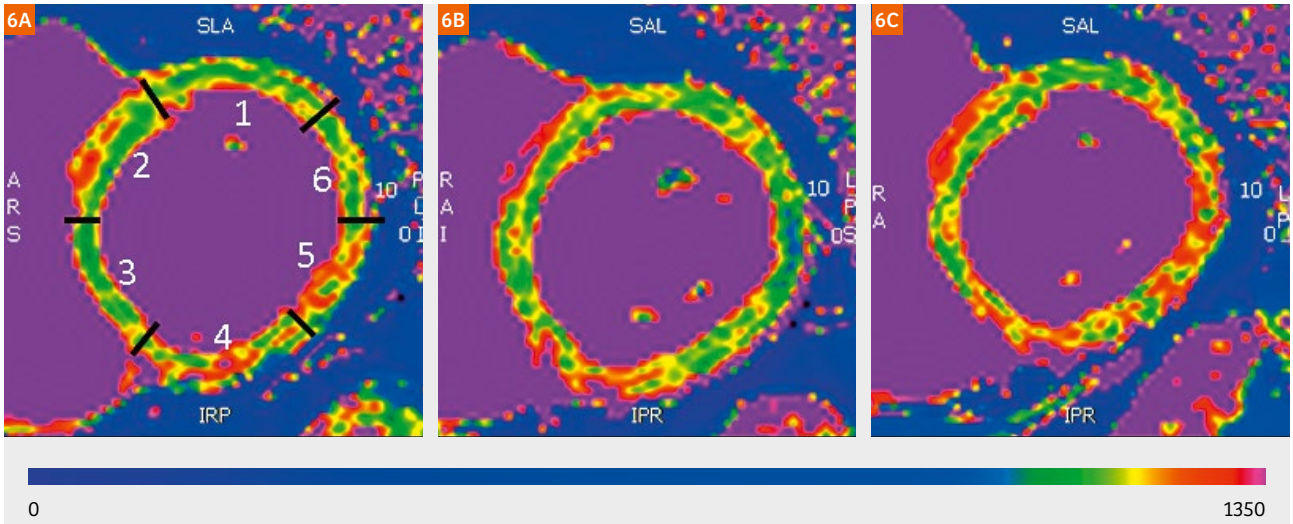

Figure 6: Basal slice through left ventricle – T1 maps

(6A) MyoMaps through the basal segments pre-treatment, individual segments being labelled from one to six
(6B) 6 weeks post
(6C) 12 months post treatment respectively

A qualitative change (increase in relaxation time) can be seen affecting the myocardium in segments 3, 4, 5, and 6 which may indicate myocardial inflammation or fibrosis.

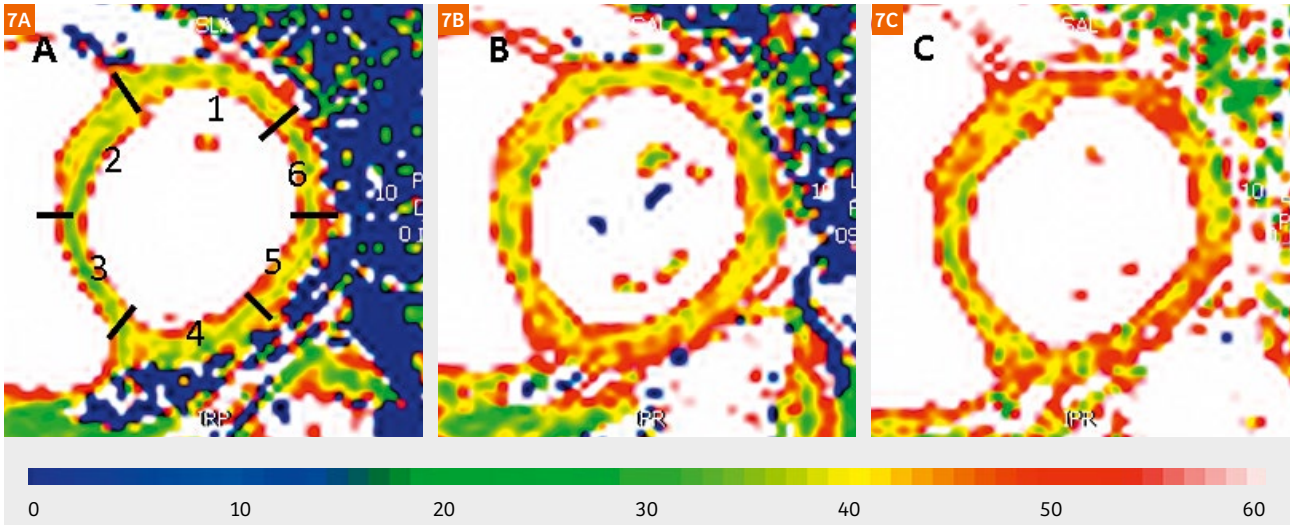

Figure 7: Basal slice through left ventricle – T2 maps

(7A) MyoMaps through the basal segments pre-treatment, individual segments being labelled from one to six
(7B) 6 weeks post
(7C) 12 months post treatment respectively

A qualitative change (increase in relaxation time) can be seen affecting the myocardium in segments 1, 4, 5, and 6 which may indicate myocardial edema.

Conclusion

The use of MyoMaps for quantitative assessment of the myocardium following cancer therapy treatment shows promise, and experience with this patient has demonstrated feasibility. In this single case study, there was an elevation of T1 and T2 relaxation times occurring 12 months following treatment, which is preceded by an increase in ECV percentage immediately following chemoradiation. These results must be placed in the context of inherent variability in T1/T2 measurements. Further studies will be required in order to determine if the findings reported in this case are significant.

The use of cardiac MRI mapping however may provide novel information regarding acute to sub-acute myocardial changes following radiation therapy.

Contact

Associate Professor Gary Liney (UNSW)
Hon. Principal Fellow, University of Wollongong Ingham Institute for Applied Medical Research & Radiation Oncology
Liverpool Hospital

1 Campbell Street
Liverpool NSW 2170
Australia
Tel.: +61 2 8738 9221
gary.liney@sswahs.nsw.gov.au

References

1 Beukema, J.C., et al., Is cardiac toxicity a relevant issue in the radiation treatment of esophageal cancer? Radiotherapy and Oncology, 2015. 114(1): p. 85–90.
2 Shirai, K., et al., Volume Histogram Parameters and Clinical Factors Associated With Pleural Effusion After Chemoradiotherapy in Esophageal Cancer Patients. International Journal of Radiation Oncology • Biology • Physics. 80(4): p. 1002–1007.
3 Kumekawa, Y., et al., Late toxicity in complete response cases after definitive chemoradiotherapy for esophageal squamous cell carcinoma. Journal of Gastroenterology, 2006. 41(5): p. 425–432.
4 Mukherjee, S., et al., The significance of cardiac doses received during chemoradiation of oesophageal and gastro-oesophageal junctional cancers. Clin Oncol (R Coll Radiol), 2003. 15(3): p. 115–20.
5 Gayed, I., et al., The clinical implications of myocardial perfusion abnormalities in patients with esophageal or lung cancer after chemoradiation therapy. The International Journal of Cardiovascular Imaging, 2009. 25(5): p. 487–495.
6 Hatakenaka, M., et al., Acute cardiac impairment associated with concurrent chemoradiotherapy for esophageal cancer: magnetic resonance evaluation. Int J Radiat Oncol Biol Phys, 2012. 83(1): p. e67–73.
7 Wijesekera, D., et al., Longitudinal Accuracy and Reproducibility of Quantitative Cardiac MRI Mapping. Journal of Medical Imaging and Radiation Oncology, 2016. 60: p. 41–95.
8 Cerqueira, M.D., et al., Standardized Myocardial Segmentation and Nomenclature for Tomographic Imaging of the Heart. A Statement for Healthcare Professionals From the Cardiac Imaging Committee of the Council on Clinical Cardiology of the American Heart Association, 2002. 105(4): p. 539–542.
9 Taylor, C.W., et al., Exposure of the Heart in Breast Cancer Radiation Therapy: A Systematic Review of Heart Doses Published During 2003 to 2013. Int J Radiat Oncol Biol Phys, 2015. 93(4): p. 845–53.

Strategic Partners for Radiation Therapy

VARIAN medical systems

SIEMENS Healthineers

HyperArc™ High Definition Radiotherapy*

MAGNETOM RT Pro edition

"The partnership between Siemens Healthineers and Varian provides access to the latest innovative technology and helps the medical community to increase the benefits for patients."

Ernesto Roesler, MD
Hospital Real Portugues, Recife, Brazil

Mission: EnVision better cancer care with intracranial HD Radiotherapy

Varian and Siemens Healthineers work together as strategic partners. Siemens' advanced diagnostic imaging capabilities coupled with Varian's powerful delivery systems and treatment planning tools give even more of an edge in the pursuit of our common goal: to EnVision better cancer care. Together we offer more personalized treatment and expanded care options that aid you in making the best possible decisions for your patients – with confidence. By gathering our strengths, we have the energy and vision to better help healthcare professionals detect, diagnose and treat cancer while paving the way for the future of cancer care.

Our partnership not only brings us together, it helps shape the future of cancer care.

* Not all products are available for sale in all markets and are subject to change. Courtesy of Varian Medical Systems

The statements by Siemens' customers presented here are based on results that were achieved in the customer's unique setting. Since there is no 'typical' hospital and many variables exist (e.g., hospital size, case mix, level of IT adoption), there can be no guarantee that other customers will achieve the same results.

First experience of 4D-MRI for abdominal radiotherapy planning

Andrew Oar[1,2]; Gary Liney[1,2,3,4]; Robba Rai[1,2,3]; Shrikant Deshpande[1,3,4]; Li Pan[5]; Meredith Johnston[1]; Michael Jameson[1,2,3,4]; Shivani Kumar[1]; Mark Lee[1,2]

[1] Liverpool and Macarthur Cancer Therapy Centre, Sydney, Australia
[2] South West Sydney Clinical School, University of New South Wales, Sydney, Australia
[3] Ingham Institute for Applied Medical Research, Sydney, Australia
[4] Centre for Medical Radiation Physics, University of Wollongong, NSW, Australia
[5] Siemens Healthineers, Baltimore, MD, USA

Introduction

Four-dimensional (4D) computed tomography (CT) is widely used in radiation therapy (RT) and remains the current standard for motion evaluation during RT planning. The use of 4D-CT allows the delineation of an internal target volume (ITV)[ICRU RPT62]. Unfortunately, 4D-CT uses additional radiation exposure to the 3D planning CT, and has limitations in soft tissue contrast. Magnetic resonance imaging (MRI) offers superior soft tissue definition to CT and therefore has potential significant advantages when implemented during the radiotherapy process. The integration of MRI into the radiotherapy planning and treatment pathway has been rapid with developments in MRI-simulation [1] and real-time MR guidance [2].

Attempts to replace 4D-CT with an MRI counterpart have been made for over a decade. Until recently, imaging physiological motion using MRI has involved unacceptable trade-offs between spatial and temporal resolution [3]. The majority of published literature has utilized 2D cine [4] sequences, which have been acquired in two orthogonal planes or in combination with a 3D volume as a surrogate for real-time 3D acquisition. Nonetheless efforts have been made utilizing 2D cine for adaptive radiotherapy planning [5]. Respiratory based sorting is another method with variable success [6]. Poor respiratory correlation can be problematic and incomplete binning can lead to gaps in data, which can be overcome by increasing scan time or utilizing a two-pass method [4, 7]. A combination of 2D-MRI and phase binning has yielded conflicting results [8] with noticeable phase mismatch and significant cycle-to-cycle motion variation. Both tumor deformation and motion out of plane is problematic with these methods. A much better approach is to acquire time-resolved 3D volume acquisitions, and this is now possible with sufficient resolution and image quality to be of clinical interest.

Here we present our initial findings using a prototype 4D-MRI technique based on a T1-weighted (T1w) 3D gradient echo (VIBE) sequence[1]. This uses a continuous radial acquisition and retrospective binning of respiratory phases, to generate 3D high-resolution images from different parts of the respiratory cycle (Siemens Healthcare, Erlangen, Germany). 4D-MRI combined with the recent interest in replicating dosimetry calculations in MRI may further abrogate the need for CT-simulation.

[1] WIP, the product is currently under development and is not for sale in the US and in other countries. Its future availability cannot be ensured.

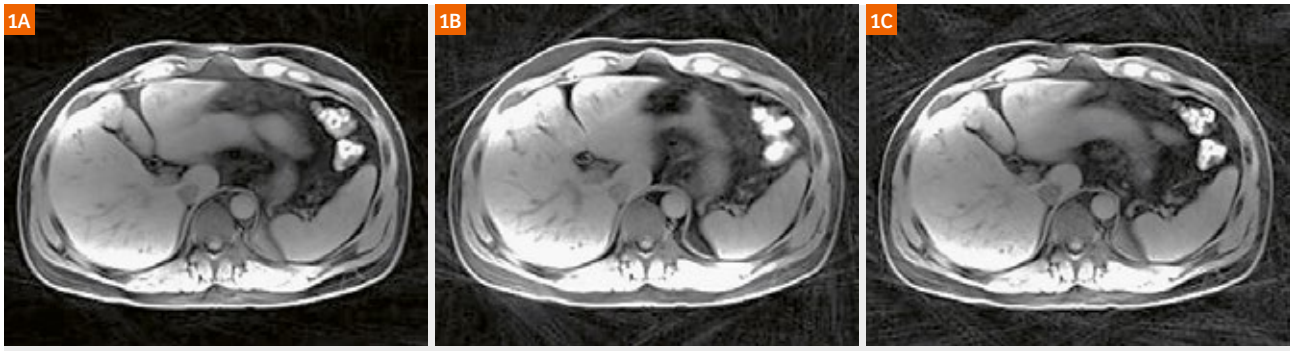

Figure 1:
The radial streak artifact seen with three **(1A)**, five **(1B)** and ten **(1C)** bins. All images using 2000 radial views.

Initial experience

MRI was performed utilizing a customized vacuum bag (BlueBAG, Elekta, Stockholm, Sweden) for immobilization and a flat wing board (MTWB09 Wingboard, CIVCO Medical Solutions, Orange City, IA, USA) with arms above the head. All MR imaging was performed on the departmental radiotherapy dedicated 3T wide-bore MRI (MAGNETOM Skyra, Siemens Healthcare, Erlangen, Germany) on a flat-bed insert (CIVCO Medical Solutions, Orange City, IA, USA) with a 32-channel posterior in-table coil and 18-channel flexible array coil. Sequences included T2 HASTE gated with phase navigation, breath-hold T1 VIBE and multiphasic (arterial, venous and transitional phases) breath-hold T1 VIBE enhanced with 0.1 ml/kg Gadobutrol (Gadovist, Bayer, Leverkusen, Germany). Additionally all volunteers and patients underwent the prototype T1-3D gradient echo with radial self-gating (Siemens Healthcare, Erlangen, Germany) 4D-MRI sequence. *k*-space sampling is performed using a stack-of-stars trajectory with golden angle increment [9]. The sequence uses data from the centre of *k*-space to extract a surrogate respiration trace, which permits self-gating.

The sequence was first optimized on two healthy volunteers to qualitatively compare image quality of the liver and evaluate the trade-off between acquisition time and artifacts. Changes in protocol were investigated to examine the effects on image quality including number of radial views (1500, 2000 and 3300) and uniform bins (3, 5 and 10). Image quality was assessed by two radiation oncologists and an experienced MRI radiographer (ML, AO, RR). When comparing the number of uniform bins, it was observed that for three bins there were fewer radial streak artefacts with overall good image quality, however the degree of motion of the liver was not completely captured. In contrast, ten bins captured a greater degree of motion but suffered from a greater degree of radial streak artefacts that impacted the ability to delineate organ borders for RT planning (see Fig. 1). However, five respiratory bins reproduced the liver motion whilst maintaining optimal image quality for contouring, and therefore five bins was selected for patient image acquisition. Two thousand radial views provided the best trade-off between time and radial streak artifacts. The acquisition time using these parameters was approximately five minutes. Increasing the number of radial views beyond this increased the acquisition time, which is not ideal for this patient cohort, without demonstrable benefits in image quality.

The efficacy of 4D-MRI with and without abdominal compression has been tested in ten volunteers (see Fig. 2).

2

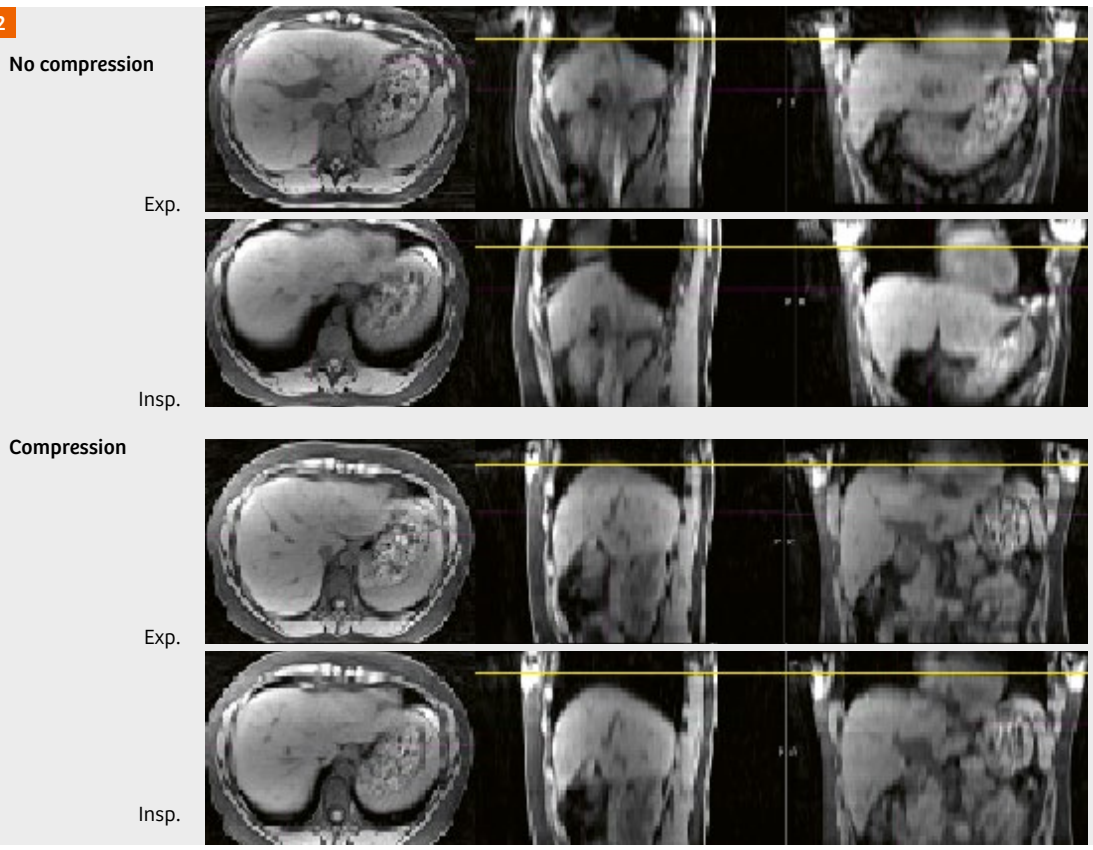

Figure 2: Feasibility of 4D-MRI and abdominal compression has been shown in ten healthy volunteers.

Exp.: Expiration

Insp.: Inspiration

Level of diaphragm in expiration is represented by yellow line. These images were acquired in axial plane.

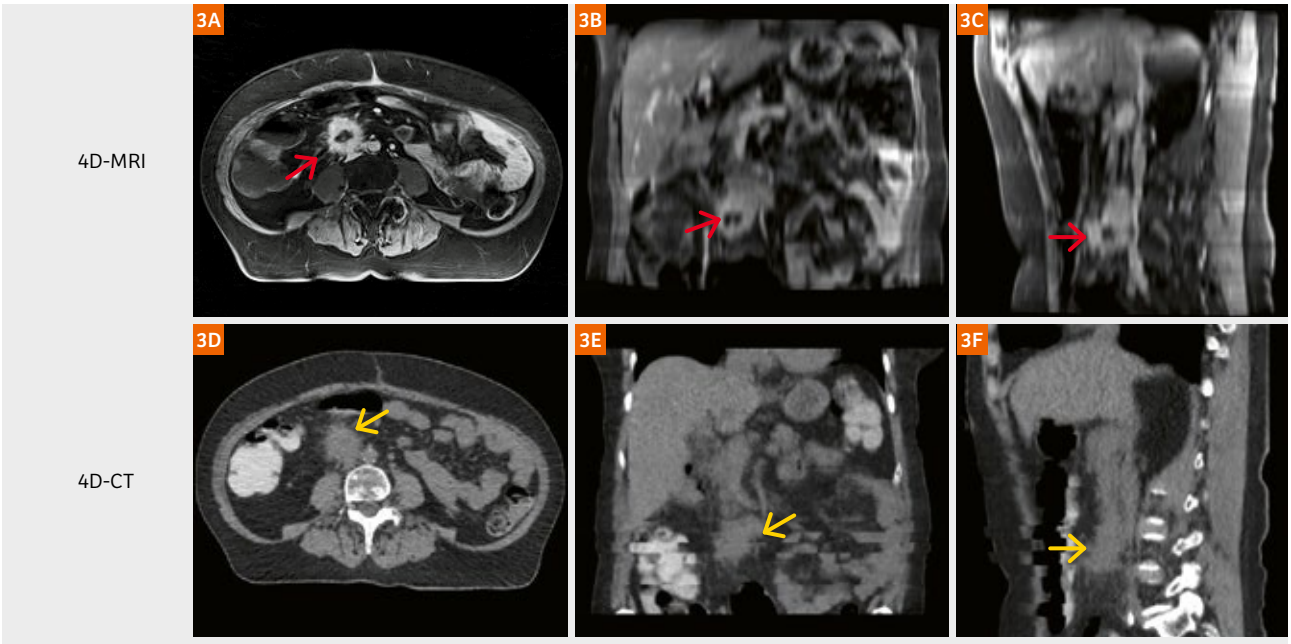

Figure 3:
Comparison of 4D-MRI and 4D-CT in a patient with solitary nodal recurrence of colorectal cancer receiving high dose radiotherapy. In this case 4D-CT failed due to step artifacts (yellow arrows) over the area of interest. Gadolinium enhanced 4D-MRI provided excellent soft tissue delineation (red arrows) and accurate motion visualization.

Figure 2 demonstrates that a high image quality can be maintained whilst obtaining physiological motion information both with and without abdominal compression. For the volunteer study, the amplitude of movement of liver and volume of lung below the T10 vertebral level has been recorded for both compression and no compression. Volunteer study results are pending for publication.

This prototype 4D-MRI sequence has demonstrated encouraging results and as a self-gating technique it is very promising. Superior soft tissue delineation and reduced radiation exposure may mean 4D-MRI is a suitable replacement for 4D-CT. Figure 3 demonstrates a sample case where 4D-CT suffered from artifacts due to inconsistent breathing rate throughout image acquisition and poor signal from the respiratory trace. In this case the step artifacts impacted the delineation of the tumor volume, introducing uncertainty for treatment. 4D-MRI in comparison provided greater soft tissue contrast (Fig. 3A) with minimal artifacts allowing greater confidence in contouring the tumor volume. The clinical outcome of the first ten patients is pending for presentation and publication.

Future direction

Local area health research and ethics board approval has been obtained for direct comparison of 4D-CT to 4D-MRI in patients receiving upper abdominal radiotherapy. Recruitment to this study is ongoing with ten patients recruited to date. 4D-CT will be directly compared to 4D-MRI in parameters such as amplitude of movement and image quality. Artifact, noise, and tumor edge detection will be graded on a four-point scale as seen in Table 1 for both 4D-CT and 4D-MRI. This scoring system has been utilized previously [10]. Tumors will be contoured on maximal inspiratory and expiratory images and directly compared to 4D-CT. Clinical data from this research project will be presented in April 2018 at ESTRO 37.

Gadoxetate sodium (Primovist, Bayer, Leverkusen, Germany) has shown exceptional diagnostic potential in patients with both primary and metastatic liver tumors [11, 12]. The slow excretion of Primovist by hepatocytes is likely to facilitate superior contrast information during 4D-MRI scanning. We intend to explore Primovist in patients with primary and secondary liver tumors during 4D-MRI and we hypothesise that despite the longer acquisition time of 4D-MRI, the benefits of contrast can be maintained.

Score	1	2	3	4
Tumor edge detection	Tumor edge clearly defined	Tumor edge slightly blurred, not impairing definition of tumor boundary	Considerable blurring of tumor edge impacting on accurate definition of tumor boundary	Significant blurring of tumor edge, definition of tumor boundary not achievable
Artifacts	No artifacts	Little artifact not impairing image quality	Considerable artifact impacting evaluation of anatomical structures	Extreme artifacts obscuring delineation of anatomical structures
Image noise	Minimal noise	Little noise not impairing diagnostic image quality	Considerable noise impacts the evaluation of anatomical structures	Extreme noise obscuring delineation of anatomical structures.
Overall image quality	Very good image quality	Fair image quality not impairing the delineation of structures	Impaired image quality that may lead to incorrect delineation	Structures not definable

Table 1: Scoring system for tumor edge detection, artifact, image noise and overall image quality.

MRI linear accelerators are likely to play an increasing role within the radiotherapy treatment paradigm. Adaptive 4D-MR guidance is now clinically achievable [5, 13]. As the quality of 4D-MR imaging improves, and the integration of MR into radiotherapy delivery systems is refined, clinician's confidence regarding real-time tumor position and movement may be further enhanced. Those patients where volumetric acquired 4D-MRI at simulation is seen to accurately represent movement of the region of interest may be the greatest beneficiaries of an MRI linear accelerator. With further refinement and rapidly growing MRI linear accelerator interest, online volumetric acquired 4D-MRI is clinically feasible. Volumetric 4D-MRI will significantly alter radiotherapy treatment delivery in liver, bowel, pancreas, heart, lymph node and prostate where real-time accuracy of soft tissues is pivotal.

Acknowledgements

The authors wish to thank Dr. Benjamin Schmitt at Siemens Healthineers for the development of this volumetric acquired 4D-MRI sequence (Siemens Healthcare, Erlangen, Germany) and ongoing input into this research project.

The statements by Siemens' customers presented here are based on results that were achieved in the customer's unique setting. Since there is no 'typical' hospital and many variables exist (e.g., hospital size, case mix, level of IT adoption), there can be no guarantee that other customers will achieve the same results.

References

1 Liney, G.P. and M.A. Moerland. Magnetic resonance imaging acquisition techniques for radiotherapy planning. in Seminars in radiation oncology. 2014. Elsevier.
2 Raaymakers, B., et al., First patients treated with a 1.5T MRI-Linac: clinical proof of concept of a high-precision, high-field MRI guided radiotherapy treatment. Physics in Medicine & Biology, 2017. 62(23): p. L41.
3 von Siebenthal, M., et al., 4D MR imaging of respiratory organ motion and its variability. Physics in medicine and biology, 2007. 52(6): p. 1547.
4 Tryggestad, E., et al., Respiration-based sorting of dynamic MRI to derive representative 4D-MRI for radiotherapy planning. Medical Physics, 2013. 40(5): p. 051909-n/a.
5 Kontaxis, C., et al., Towards fast online intrafraction replanning for free-breathing stereotactic body radiation therapy with the MR-linac. Phys Med Biol, 2017. 62(18): p. 7233-7248.
6 Du, D., et al., High-quality T2-weighted 4-dimensional magnetic resonance imaging for radiation therapy applications. International Journal of Radiation Oncology* Biology* Physics, 2015. 92(2): p. 430-437.
7 Liu, Y., et al., T2-weighted four dimensional magnetic resonance imaging with result-driven phase sorting. Medical physics, 2015. 42(8): p. 4460-4471.
8 Park, S., et al., Simultaneous tumor and surrogate motion tracking with dynamic MRI for radiation therapy planning. Phys Med Biol, 2017.
9 Winkelmann, S., et al., An optimal radial profile order based on the Golden Ratio for time-resolved MRI. IEEE transactions on medical imaging, 2007. 26(1): p. 68-76.
10 Kumar, S., et al., Feasibility of free breathing Lung MRI for Radiotherapy using non-Cartesian *k*-space acquisition schemes. The British journal of radiology, 2017. 90(1080): p. 20170037.
11 Hammerstingl, R., et al., Diagnostic efficacy of gadoxetic acid (Primovist)-enhanced MRI and spiral CT for a therapeutic strategy: comparison with intraoperative and histopathologic findings in focal liver lesions. European radiology, 2008. 18(3): p. 457.
12 Ichikawa, T., et al., Detection and characterization of focal liver lesions: a Japanese phase III, multicenter comparison between gadoxetic acid disodium-enhanced magnetic resonance imaging and contrast-enhanced computed tomography predominantly in patients with hepatocellular carcinoma and chronic liver disease. Investigative radiology, 2010. 45(3): p. 133-141.
13 PRNewswire, Early Clinical Data Suggests Nearly 2X Prolonged Median Survival for Inoperable, Locally Advanced Pancreatic Cancer with MRIdian MR-Guided Radiation Therapy. 2017.

Contact Dr. Andrew J. Oar
Liverpool Cancer Therapy Centre

Locked Bag 7103
Liverpool BC 1871, NSW, Australia
andrew.oar@health.nsw.gov.au

4D-MRI sequence for radiotherapy application: validation of a retrospective method on a motion phantom

Soléakhéna Ken[1]; Tatiana Nemtanu[1]; Zarko Celicanin[2]; Oliver Bieri[2]; Philippe Cattin[3]; Karen Mkhitaryan[4]; Laure Parent[1]

[1] Institut Universitaire du Cancer de Toulouse Oncopôle, Engineering and medical physics department, Toulouse, France
[2] Department of Radiology, Division of Radiological Physics, University of Basel Hospital, Basel, Switzerland.
[3] Center for medical Image Analysis & Navigation (CIAN), Brigham and Women's Hospital Harvard Medical School, Boston, USA; Medical Image Analysis Center, University of Basel, Basel, Switzerland
[4] Siemens Healthineers, Magnetic Resonance Division, Aix-en-Provence, France

Introduction

Abdominal motion imaging is challenging due to breathing artifacts. A widely used technique for organ motion management in radiotherapy (RT) is 4D-CT. It consists of acquiring a breathing signal thanks to an external surrogate at the same time as repeated acquisitions of images and the sorting of the images according to the respiratory cycle obtained from the breathing signal. However, CT scans present poor contrast for soft tissue, such that the lesions are difficult to observe even when a contrast agent is used. To overcome this limitation, MR images are acquired for precise tumor delineation and in our institute, motion is managed with acquisitions triggered on exhale phase [1]. Both CT and MR images are registered on exhale phase, as these are more reproducible [2]. In this configuration, only the exhale phase of the respiratory cycle is registered, and therefore the dynamic behavior and the organ deformation during free breathing are not captured.

4D-MRI is a promising method for imaging respiratory movements. Besides excellent soft tissue contrast, the method exhibits great flexibility in selecting image plane orientations. Different strategies have been developed for organ movement consideration [3–5]. These methods are limited by the temporal resolution, as well as image quality. A novel retrospective gating approach for dynamic MR imaging during free breathing was developed by von Siebenthal et al. [3] and further improved by Celicanin et al. [6]. In this work, the innovative 4D-MRI approach has been evaluated and validated for RT application using a motion phantom.

Figure 1:
The Quasar™ MRI4D motion phantom placed in the 1.5T MAGNETOM Aera bore.

Motion phantom

The Quasar™ MRI4D motion phantom[1] (Modus QA, London, ON, Canada) consists of an oval hollow body, in which two cylindrical inserts may be positioned (Fig. 1). The MRI contrast gel used in this study, which is a prototype based on a gellan gum gel, containing manganese chloride as a contrast agent (0.3 mM for the high-contrast tumor sphere and 0.15 mM for the surrounding medium) was supplied by Modus QA. Different motion waveforms were tested. The sinusoidal mode allows the adjustment of the frequency and the amplitude of the motion. On Figure 2A, an example of a 5 s respiratory cycle (12 breaths/min) with 20 mm peak-to-peak amplitude is presented. In addition, MRI measurements were realized for respiratory cycles with duration of 4 s and 6 s with 10 and 30 mm amplitude peak-to-peak (not shown). Real respiratory cycle from patient data was also acquired (Fig. 2B).

[1] The information shown herein refers to products of 3rd party manufacturer's and thus are in their regulatory responsibility. Please contact the 3rd party manufacturer for further information.

2A

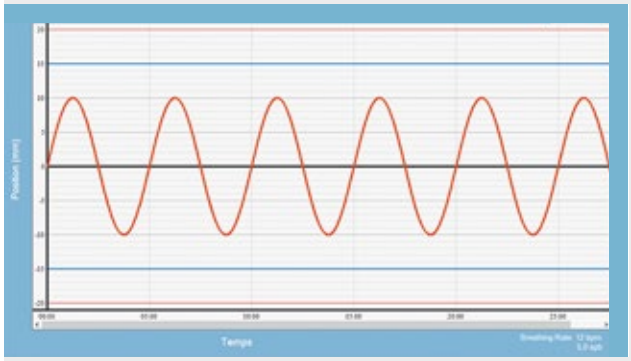

2B

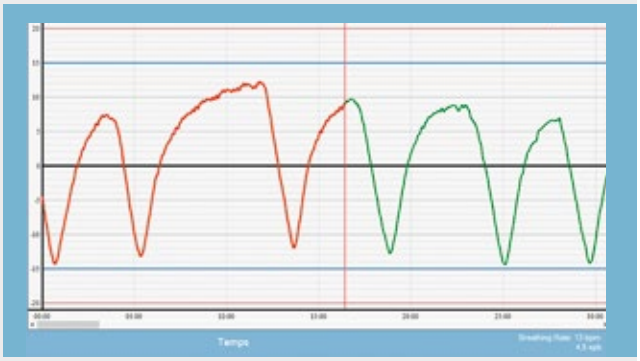

Figure 2:
Examples of 5 s respiratory cycles with 20 mm peak-to-peak amplitude **(2A)** and real respiratory signal from patient recording **(2B)** are given as motion waveforms to the phantom.

3

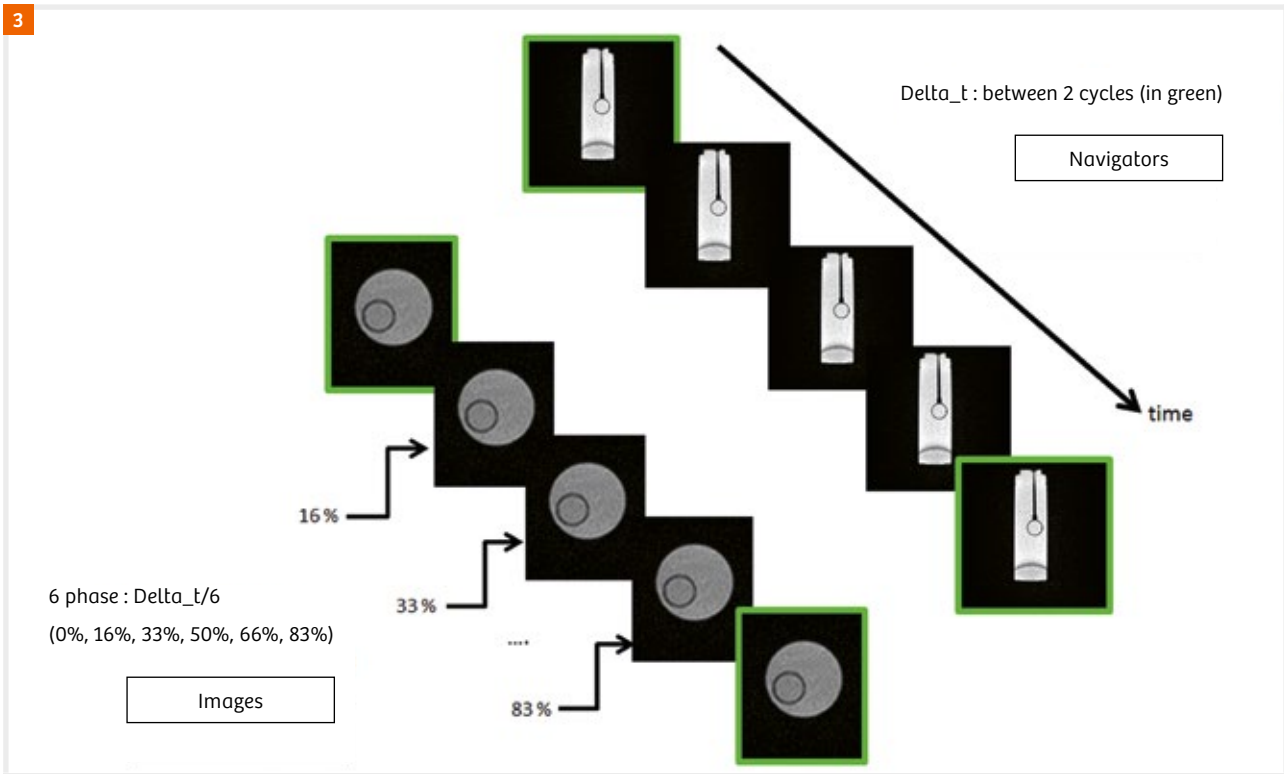

Figure 3:
Representation of 4D-MR images sorting according to 6 respiratory phases. Respiratory phases are defined identically as for the 4D-CT by the time interval between two navigators acquired at the same position.

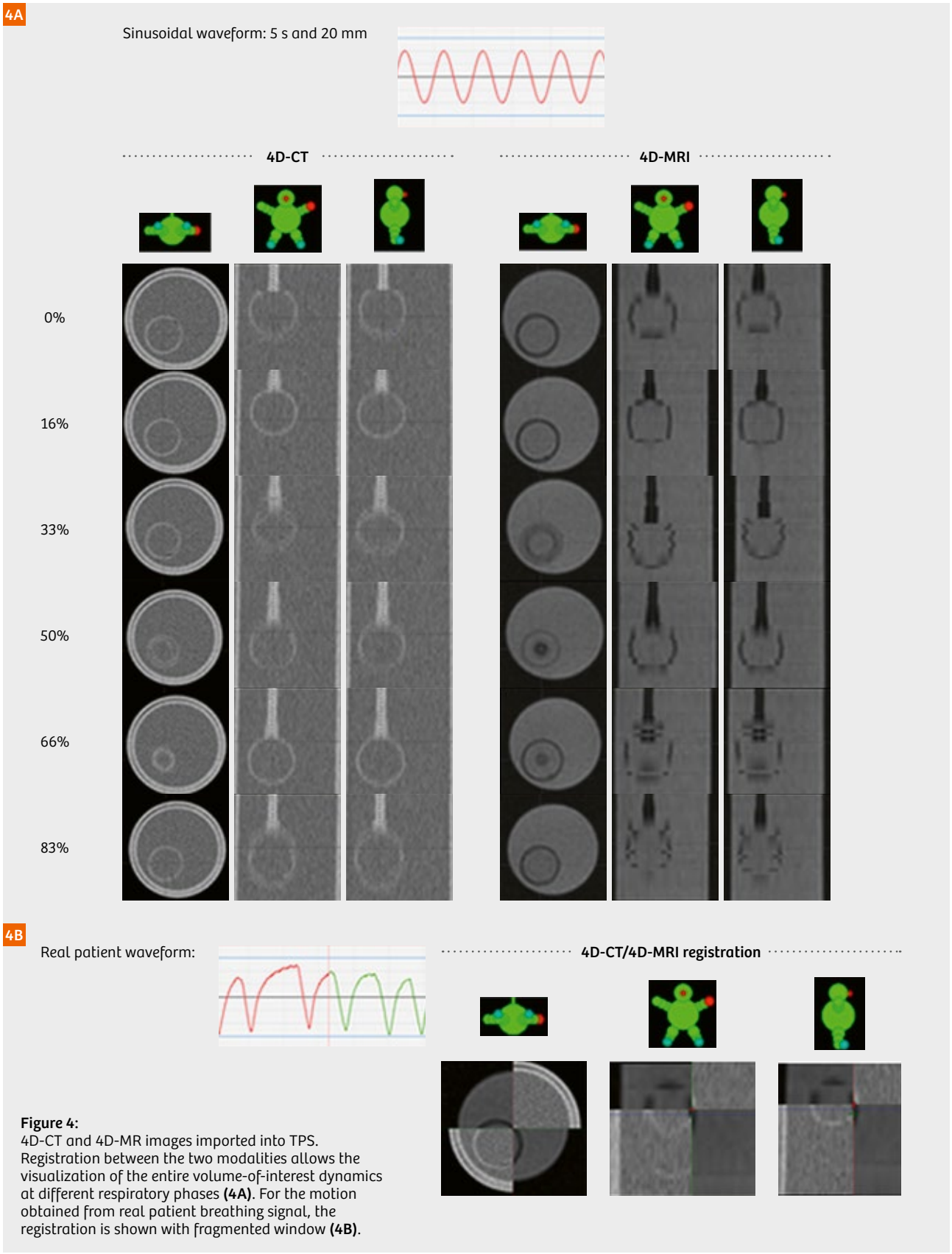

Figure 4:
4D-CT and 4D-MR images imported into TPS. Registration between the two modalities allows the visualization of the entire volume-of-interest dynamics at different respiratory phases **(4A)**. For the motion obtained from real patient breathing signal, the registration is shown with fragmented window **(4B)**.

MRI acquisitions

The data were acquired using a MAGNETOM Aera 1.5T whole body scanner (Siemens Healthcare, Erlangen, Germany), using an 18-channel design body flex coil. The 4D-MRI sequence is based on a modified balanced Steady State Free Precession (bSSFP) sequence [6] and consists of an interleaved acquisition of 2D data slices and navigators. The navigators were acquired at a fixed position in sagittal orientation and were used to determine the motion position during breathing. Contrary to navigators, the image slice position changed in order to cover the entire volume-of-interest in axial direction. 4D-MR images were acquired over 40 slices with a thickness of 2.5 mm, acquisition matrix of 272 x 288, FOV 299 x 299 mm^2 and with the following parameters Flip Angle (FA) = 70°, TE/TR = 2.43 ms / 440.75 ms, slice-time-resolution 0.44 ms. The sequence was repeated 10 times to cover the entire respiratory cycle. Total acquisition time for 10 repetitions was less than 6 min.

4D-MRI data reconstruction

The period of the respiratory cycle was divided in 6 bins, similarly to 4D-CT, which corresponds to 0%, 16%, 33%, 50%, 66% and 83% of the respiratory phase. The 2D-MR image slices where arranged by the respiratory phases and stacked in 3D-volumes thanks to the position and acquisition time of the navigators (Fig. 3). The data slices with the same slice location were grouped, offering the visualization of the entire volume-of-interest.

4D-CT/4D-MRI registration

4D-CT images of the Quasar™ MRI4D motion phantom with the same motion waveforms as for the 4D-MRI were acquired and integrated in our Treatment Planning System (Eclipse Aria v13.7; Varian Medical Systems, Palo Alto, CA, USA). On Figure 4A, 4D-MR and 4D-CT scan registration for the sinusoidal waveform with 12 breaths/min and 20 mm peak-to-peak amplitude is shown. All respiratory phases were successfully reconstructed. The movement amplitude is well captured. 0%, 16%, 50% and 66% phases of the sinusoidal waveform are well defined both on 4D-MRI and 4D-CT images. Movement artifacts are clearly visible on both modalities on 33% and 83% phases during which the movement is the fastest. Registration of 4D-CT and 4D-MRI acquired from waveform of patient real respiratory signal is shown on Figure 4B.

Conclusion

4D-MRI sequence for RT application was validated on motion phantom with several evaluations of different motion signals. Acquisition time is compatible with clinical routine. Future work will consist of performing measurements on patients to assess whether the sequence is optimized to visualize the gold fiducials and the lesion for liver stereotactic body RT application.

Acknowledgements

The authors are thankful to the MODUS QA team for their collaboration work with the motion phantom.

References

1 S. Ken et al., "Benefits of Time-Correlated and Breath-Triggered MR Acquisition in Treatment Position for Accurate Liver Lesion Contouring in Stereotactic Body Radiotherapy," MReadings: MR in RT, Second Extended Edition, pp. 86–89, 2016.
2 Y. Seppenwoolde et al., "Precise and Real-Time Measurement of 3D Tumor Motion in Lung Due To Breathing and Heartbeat, Measured During Radiotherapy," Int. J. Radiat. Oncol. Biol. Phys., vol. 53, no. 4, pp. 822–834, 2002.
3 M. von Siebenthal, et al., "4D MR imaging of respiratory organ motion and its variability.," Phys. Med. Biol., vol. 52, no. 6, pp. 1547–64, 2007.
4 J. Tokuda et al., "Adaptive 4D MR imaging using navigator-based respiratory signal for MRI-guided therapy," Magn. Reson. Med., vol. 59, no. 5, pp. 1051–1061, 2008.
5 J. Cai, et al., "Four-dimensional magnetic resonance imaging (4D-MRI) using image-based respiratory surrogate: A feasibility study," Med. Phys., vol. 38, no. 12, p. 6384, 2011.
6 Z. Celicanin, et al., "Simultaneous acquisition of image and navigator slices using CAIPIRINHA for 4D MRI," Magn. Reson. Med., vol. 73, no. 2, pp. 669–676, 2015.

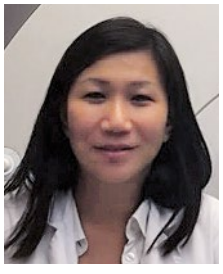

Contact

Soléakhéna Ken
Research Engineer
Institut Universitaire du Cancer Toulouse – Oncopôle

1 avenue Irène Joliot-Curie
31059 Toulouse Cedex 9
France
Phone: +33 5 31 15 54 80
ken.soleakhena@iuct-oncopole.fr

Quantitative WB-MRI with ADC histogram analysis for response assessment in diffuse bone disease

Danoob Dalili[1]; Anwar R. Padhani[2]; Robert Grimm[3]

[1] Imperial College Healthcare NHS Trust, St Mary's Hospital, London, United Kingdom
[2] Paul Strickland Scanner Centre, Mount Vernon Cancer Centre, Northwood, Middlesex, United Kingdom
[3] Siemens Healthineers, Erlangen, Germany

Introduction

Tumor heterogeneity occurs at multiple levels with marked differences in cell mix, size and arrangements. Heterogeneity also exists in microenvironmental factors (including oxygenation, pH, interstitial pressure, blood flow), metabolism and gene expression. This profound heterogeneity is extremely important for prognosis, therapy planning, drug delivery, ultimately affecting patient outcomes. There are numerous ways of investigating tumor heterogeneity, which include using functional and molecular imaging, some of which can be applied to clinical data [1].

Quantitative assessment of tissue water diffusivity using ADC values allows tissue microstructure at a µm–mm scale to be evaluated, thus reflecting tissue cellularity, organisation and blood flow. Most studies investigating

Continued on page 61.

Figure 1: Morphological images and 3D DWI MIPs (inverted scale).

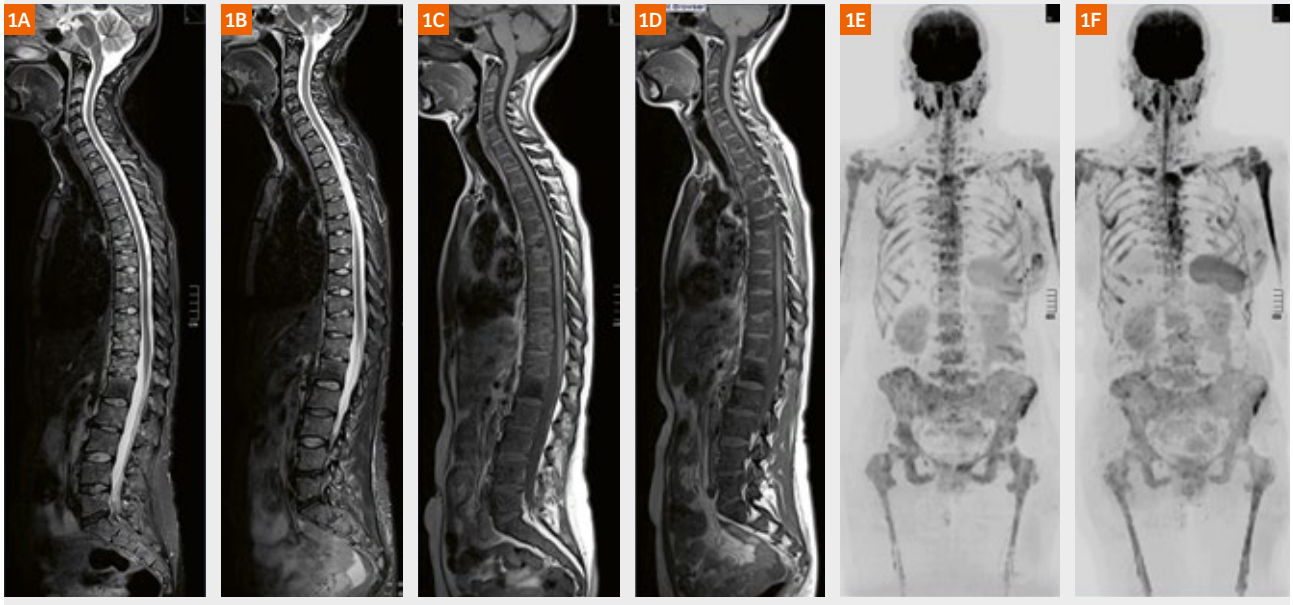

Left 2-columns: Whole-spine sagittal STIR sequences show diffuse bone marrow infiltration at baseline **(1A)** with no interval changes following hormonal therapy **(1B)**. Middle 2-columns: Whole-spine sagittal T1-weighted images show diffuse bone marrow infiltration with no appreciable return of bone marrow fat after therapy **(1D)**.

Right 2-columns: Whole-body b900 3D MIP (inverted scale). The bone marrow is diffusely involved with diffuse regions of high-signal intensity in the axial skeleton and in the proximal limb bones prior to therapy. A minor global reduction in the b900 signal intensity of bone marrow can be seen but this is not very convincing **(1F)**.

Figure 2: Morphologic and diffusion-weighted axial sequences with axial bone window CT images of the L3 vertebral body and sacrum before and on hormonal therapy with bisphosphonates.

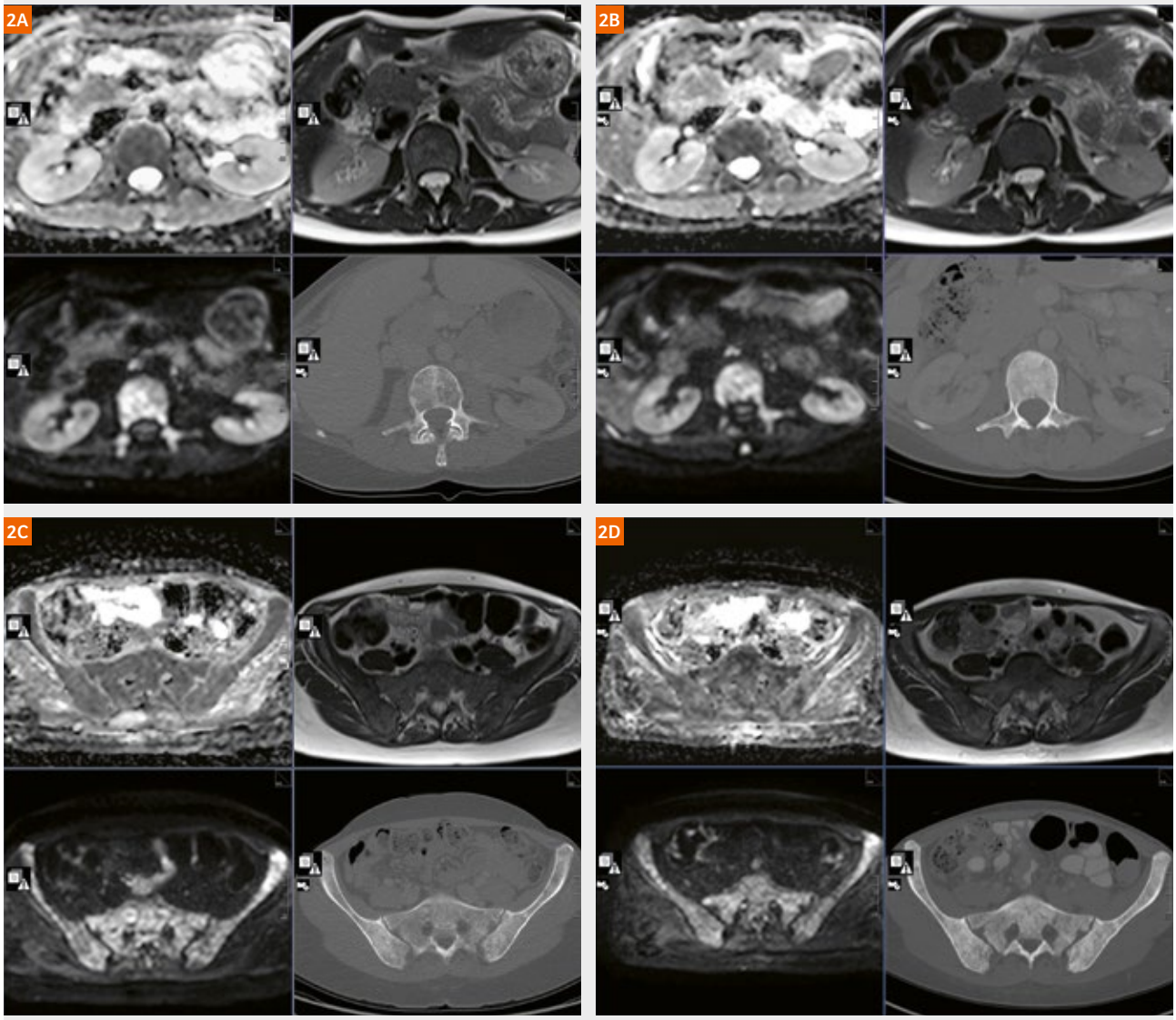

Axial ADC, T2w-HASTE, b900 and axial bone window CT scan images before and during therapy through the L3 vertebral body **(2A, B)** and sacrum **(2C, D)**.

Figures 2A and 2B: the L3 vertebral body marrow shows no change in ADC values but there is some decrease in the b900 signal intensity. A uniform increase in CT density with 'milky appearance' of the bone is consistent with responding disease (CT density 300 HU before therapy and 550 HU after therapy). However, the persistent elevated signal intensity on the b900 images suggests the ongoing presence of active disease.

Figures 2C and 2D: the CT scan shows a uniform increase in bone density (CT density 315 HU before therapy and 530 HU after therapy). Again the CT density change is not high enough to be confident regarding response. However, the ADC maps show intermixing of high and low ADC value voxels resulting in a textural change.

Figure 3: Whole-body tumor load analysis.

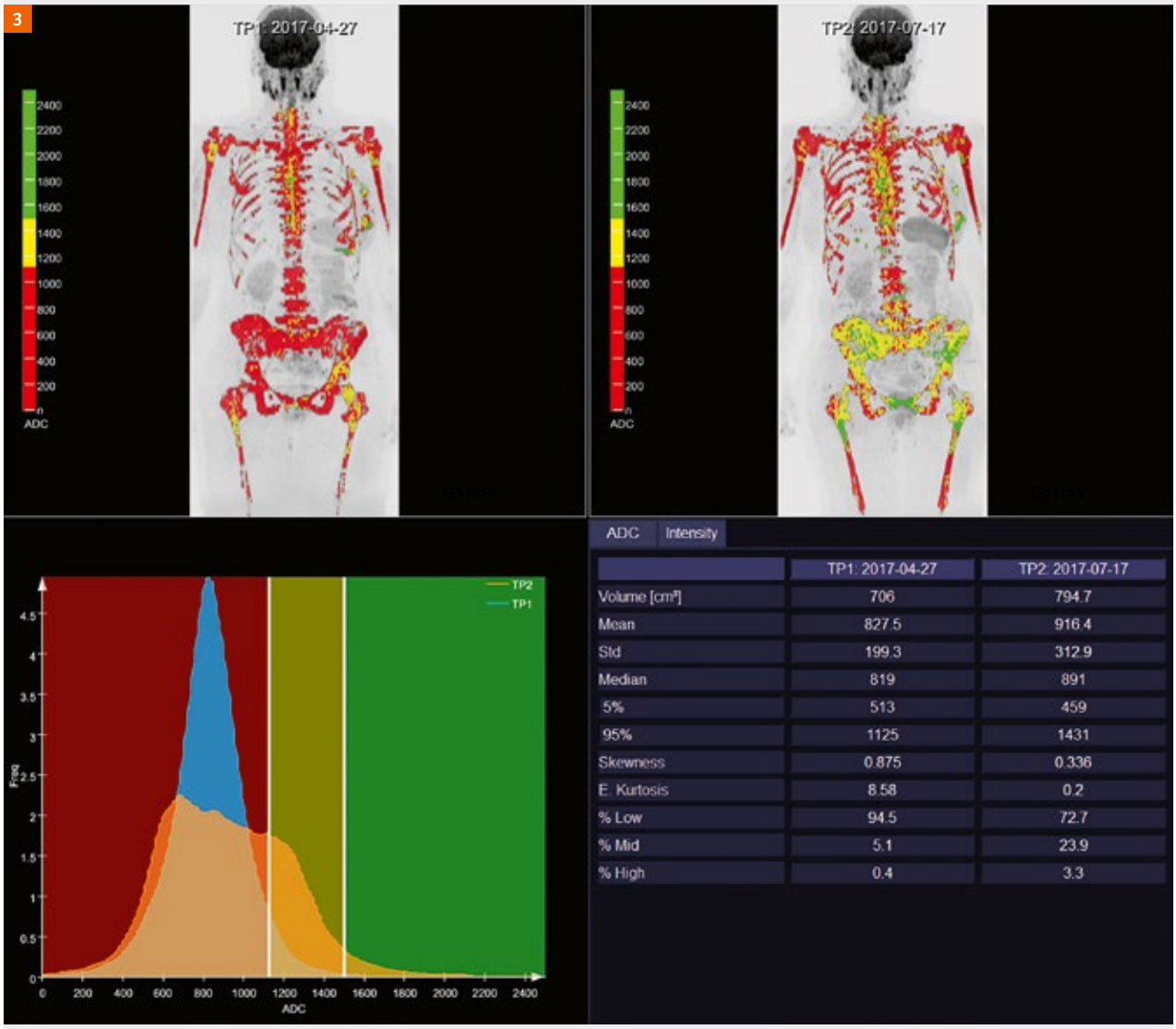

	TP1: 2017-04-27	TP2: 2017-07-17
Volume [cm³]	706	794.7
Mean	827.5	916.4
Std	199.3	312.9
Median	819	891
5%	513	459
95%	1125	1431
Skewness	0.875	0.336
E. Kurtosis	8.58	0.2
% Low	94.5	72.7
% Mid	5.1	23.9
% High	0.4	3.3

WB-tumor load segmentations were undertaken on *syngo*.via Frontier MR Total Tumor Load software[1]. The whole-body b900 images were segmented using computed b-value images of 900–1000 s/mm², setting a signal intensity threshold of 100 AU. Extraneous signals (such as the brain, kidneys, spleen and bowel) were removed, to leave only recognizable bone disease sites. The b900 MIP images are overlaid with ADC value classes using the 95th centile value of the pre-treatment histogram (1125 µm²/s) and 1500 µm²/s.

Red colored voxels represent untreated disease or those with no-detectable response.

Green colored voxels have ADC values ≥1500 µm²/s (representing voxels that are 'highly likely' to be responding).

The yellow voxels lie between the 95th centile value of the pre-treatment histogram (1125 µm²/s) and 1500 µm²/s.
Thus, yellow voxels represent regions 'likely' to be responding.

706 mL of bone marrow was segmented before therapy and 795 mL after therapy. Note that there is no significant increase in median ADC values (819 µm²/s and 891 µm²/s respectively), but a decrease in excess kurtosis (8.6 and 0.2 respectively), and broadening of ADC histogram and an increase in the standard deviation (199 and 313 µm²/s respectively) can be seen on the corresponding relative frequency histograms. There is a unimodal distribution of ADC values at baseline (TP1) and a plateau distribution of the post-treatment (TP2) histogram.

The whole-body ADC color projections focusing on response (ADC maximum intensity projections) for both time points are shown.
A spatial discordant response pattern is visible with responding increasing yellow and green voxels in the pelvis and proximal femora.

[1] *syngo*.via Frontier is for research only, not a medical device. *syngo*.via Frontier MR Total Tumor Load is a released research prototype.

the usefulness of diffusion imaging for disease characterization, prognostication and therapy response use region-of-interest (ROI) approaches deriving mean values of ADC (unit: $\mu m^2/s$). This averaging method can be used to assess heterogeneity between ROIs or between patients, but fundamentally, ignores the heterogeneity within the ROI.

The characterization of tissues can be improved using histogram-based assessments of the distribution of ADC values. Histogram approaches have multiple advantages, including volume-of-interest (VOI) assessments, thus avoiding the subjectivity that is inherent with ROI placements. Importantly, histograms can provide additional metrics that reflect the texture of lesions, thereby allowing heterogeneity of ADC distribution within tissue to be assessed.

Histogram-based ADC analyses have mostly been undertaken in the context of neuroimaging showing added value for brain tumor grading, prognosis and therapy response [2–4]. However, this approach is increasing being applied to extracranial tissues, including evaluations of cervix and breast cancers [5–7], liver fibrosis [8], peritoneal malignancy [9] and bone metastases [10, 11]. These and other studies, have shown the potential of ADC histogram descriptors to improve the characterization of tissues, as well as to serve as prognostic and response biomarkers.

In this report, we describe a patient with breast cancer metastasising to the bone marrow, who underwent hormonal treatment. CT scans, morphologic MR images and ROI derived ADC assessments were confusing when trying to gauge the success of therapy. Volume based assessments of whole-body tumor load and ADC histograms, enabled an accurate assessment of the clinical status allowing therapy to be continued.

Case study

A 37-year-old woman presenting with a 2-year history of lower back pain was found to have diffuse metastatic bone infiltration following an MRI of her lumbar spine. A bone marrow trephine biopsy and core biopsy of an asymptomatic left breast mass showed the presence of metastatic ER-positive, HER2 2+ (FISH-negative), grade 2 invasive ductal carcinoma of the breast. She was commenced on systemic anticancer hormonal therapy with Tamoxifen and Goserelin as well as with Zoledronic acid infusions.

She underwent baseline and 3 month follow-up whole-body MRI scans with diffusion-weighted sequences using a 1.5T MAGNETOM Avanto scanner using a published protocol [12]. The baseline scan demonstrated extensive metastatic bone only disease (Figs. 1, 2) that does not change appreciably on morphological T1w, T2w and STIR images of the spine. CT scans undertaken at the corresponding time points, show uniform increases in bone density with a 'milky texture' which are difficult to interpret regarding the activity of the underlying disease. It's only when CT density increases to >850 HU that it is possible to be confident about the likelihood of inactive disease [13]. There was minimal reduction in b900 signal intensity.

The diffusion-weighted images for both timepoints were analysed using the threshold-based segmentation, *syngio*.via Frontier MR Total Tumor Load software[1] [14]. The pre-treatment ADC histogram has a unimodal distribution of ADC values with high excess kurtosis (Fig. 3). After 3 months of hormonal therapy, a plateau distribution of ADC values can be seen with little change in the mean ADC but a greater spread in ADC values can be appreciated. Responding voxels (yellow/green voxels) are mostly seen in the pelvis and proximal femora on the ADC color projections focusing on response. These ADC histograms are consistent with a favorable therapy response, because of which treatment was continued.

Discussion

There are a variety of approaches for objectively displaying and analyzing ADC images in response assessment settings. Most studies report mean values from single/multiple ROIs placed on high b-value images, which are then copied on ADC maps for quantitate ADC value readouts. Recently, studies have begun to report on central tendency measures (mean, median, mode values) of ADC histograms on volumes of interest (VOIs). Because bone metastases are heterogeneous in their spatial ADC distributions, these simpler, first order measures have limited abilities to detect treatment-related changes, particularly if there are both increases and decreases in ADC in response to treatment (for example, when ADC values increase due to tumor cell kill and decrease due to bone marrow renormalization, fibrosis and dehydration) [15]. As a result, the net mean/median ADC change may be minimal. Furthermore, if large cystic or necrotic areas are present, then the ability to detect therapy response induced changes may be blunted.

More complex changes in ADC values can be evaluated by assessing the spread of the ADC data (variance, standard deviation, range (maximum-minimum difference), centile ranges, histogram entropy). The spread of ADC data allows estimates of the proportions of responding or non-responding tumor volume to be determined by the application of threshold cut-off values. So, in this case,

[1] *syngo*.via Frontier is for research only, not a medical device. *syngo*.via Frontier MR Total Tumor Load is a released research prototype.

the proportion of voxels in the active range (ADC-low voxels below 1125 $\mu m^2/s$) is 95% and 73% respectively at the two time-points.

Other higher order descriptors of histograms such as skewness (a measure of the degree of asymmetry of a distribution) and kurtosis (which is the degree of peakedness of a distribution) can also be helpful for evaluating therapy response. Comparison of relative frequency histograms to normal distributions allows quantitative values to be assigned to histogram kurtosis; positive excess kurtosis values >0 (leptokurtic shape) indicates a higher peak than for a normal distribution (normal distribution shape is described as mesokurtic with an excess kurtosis value = 0). After therapy, excess kurtosis decreases often reaching values <0 (platykurtic).

Readers should also be aware that both measurement (e.g. poor SNR) and analysis methods (e.g., two-point fitting for generating ADC values) can alter the skewness of histograms independent of therapy induced effects, because of which the quality of ADC maps images should be critically assessed, before higher order histogram descriptors such as maximum and minimum values, range and skewness are used to infer biologic significance.

ADC histogram analysis for assessing bone metastases

ADC histograms of untreated bone metastases are often positively skewed (tail to the right) with positive excess kurtosis. For our data acquisition protocol that uses b50, b600 and b900 mm^2/s diffusion-sensitizing gradients, the majority of tumor ADC pixel values usually lie in the 650–1500 $\mu m^2/s$ range for untreated disease. Positive excess kurtosis is often maintained in the setting of tumor progression or in stable disease, although mean/median values may change depending on the relative extent of tumor infiltration and fat content in the bone marrow. If tumors are necrotic before treatment or if there has been a response to prior treatments, then more complex histogram shapes can be seen.

When tumors respond successfully to therapy, kurtosis values generally decrease and the standard deviation/variance increases. Negative skewness (tail to the left) often develops if the histogram retains a unimodal shape. Thus, the transformation of a positive kurtosis, positively skewed unimodal ADC distribution into a plateau shape in response to a therapy indicates likely response even in the absence of a significant change in mean/median ADC values. Where successful response is accompanied by regeneration of the normal bone marrow as part of the healing process, a distinct second ADC peak below the tumor peak can be observed which is illustrated in two accompanying cases within this issue of MAGNETOM Flash [15, 16].

Radiologists often enquire when there is an absolute need to use ADC histograms in "daily clinical practice"? Generally, we find ADC analyses are most useful in the presence of extensive, diffuse metastatic disease on WB-DWI or when there has been an apparent mixed/heterogeneous response to therapy. In these patients, visual inspections of morphological and diffusion-weighted images can be problematic and applying the MET-RADS response criteria [12] can be challenging due to the high volume of disease present. In these cases, we find histogram analyses indispensable because of the ability to observe changes in the spread, skewness and kurtosis of the ADC data.

References

1 Just N. Improving tumour heterogeneity MRI assessment with histograms. British journal of cancer. 2014 Dec 9;111(12):2205-13.
2. Song YS, Choi SH, Park CK, Yi KS, Lee WJ, Yun TJ, Kim TM, Lee SH, Kim JH, Sohn CH, Park SH. True progression versus pseudoprogression in the treatment of glioblastomas: a comparison study of normalized cerebral blood volume and apparent diffusion coefficient by histogram analysis. Korean journal of radiology. 2013 Aug 1;14(4):662-72.
3. Gutierrez DR, Awwad A, Meijer L, Manita M, Jaspan T, Dineen RA, Grundy RG, Auer DP. Metrics and textural features of MRI diffusion to improve classification of pediatric posterior fossa tumors. American Journal of Neuroradiology. 2014 May 1;35(5):1009-15.
4. Tozer DJ, Jäger HR, Danchaivijitr N, Benton CE, Tofts PS, Rees JH, Waldman AD. Apparent diffusion coefficient histograms may predict low-grade glioma subtype. NMR in biomedicine. 2007 Feb 1;20(1):49-57.
5. Rosenkrantz AB. Histogram-based apparent diffusion coefficient analysis: an emerging tool for cervical cancer characterization?. American Journal of Roentgenology. 2013 Feb;200(2):311-3.
6. Downey K, Riches SF, Morgan VA, Giles SL, Attygalle AD, Ind TE, Barton DP, Shepherd JH, deSouza NM. Relationship between imaging biomarkers of stage I cervical cancer and poor-prognosis histologic features: quantitative histogram analysis of diffusion-weighted MR images. American Journal of Roentgenology. 2013 Feb;200(2):314-20.
7. Johansen R, Jensen LR, Rydland J, Goa PE, Kvistad KA, Bathen TF, Axelson DE, Lundgren S, Gribbestad IS. Predicting survival and early clinical response to primary chemotherapy for patients with locally advanced breast cancer using DCE-MRI. Journal of Magnetic Resonance Imaging. 2009 Jun 1;29(6):1300-7.
8. Fujimoto K, Tonan T, Azuma S, Kage M, Nakashima O, Johkoh T, Hayabuchi N, Okuda K, Kawaguchi T, Sata M, Qayyum A. Evaluation of the mean and entropy of apparent diffusion coefficient values in chronic hepatitis C: correlation with pathologic fibrosis stage and inflammatory activity grade. Radiology. 2011 Mar;258(3):739-48.
9. Kyriazi S, Collins DJ, Messiou C, Pennert K, Davidson RL, Giles SL, Kaye SB, deSouza NM. Metastatic ovarian and primary peritoneal cancer: assessing chemotherapy response with diffusion-weighted MR imaging—value of histogram analysis of apparent diffusion coefficients. Radiology. 2011 Oct;261(1):182-92.
10. Blackledge MD, Collins DJ, Tunariu N, Orton MR, Padhani AR, Leach MO, Koh DM. Assessment of treatment response by total tumor volume and global apparent diffusion coefficient using diffusion-weighted MRI in patients with metastatic bone disease: a feasibility study. PLoS One. 2014 Apr 7;9(4):e91779.

11. Perez-Lopez R, Mateo J, Mossop H, Blackledge MD, Collins DJ, Rata M, Morgan VA, Macdonald A, Sandhu S, Lorente D, Rescigno P. Diffusion-weighted imaging as a treatment response biomarker for evaluating bone metastases in prostate cancer: a pilot study. Radiology. 2016 Nov 22;283(1):168-77.
12. Padhani AR, Lecouvet FE, Tunariu N, Koh DM, De Keyzer F, Collins DJ, Sala E, Schlemmer HP, Petralia G, Vargas HA, Fanti S. METastasis Reporting and Data System for Prostate Cancer: practical guidelines for acquisition, interpretation, and reporting of whole-body magnetic resonance imaging-based evaluations of multiorgan involvement in advanced prostate cancer. European urology. 2017 Jan 31;71(1):81-92.
13. Beheshti M, Vali R, Waldenberger P, Fitz F, Nader M, Hammer J, Loidl W, Pirich C, Fogelman I, Langsteger W. The use of F-18 choline PET in the assessment of bone metastases in prostate cancer: correlation with morphological changes on CT. Molecular imaging and biology. 2010 Feb 1;12(1):98-107.
14. Grimm R, Padhani AR. Whole-body Diffusion-weighted MR Image Analysis with *syngo*.via Frontier MR Total Tumor Load. MAGNETOM Flash (68) 2/2017, 73-75.
15. Dalili D, Joshi P, Grimm R, Padhani AR. Evolution of the malignant bone marrow with successful therapy – quantitative analysis with whole body diffusion MRI. MAGNETOM Flash (69) 3/2017, 47–52.
16. Dalili D, Padhani AR, Grimm R. Quantitative WB-MRI with ADC histogram analysis for demonstrating complex response of bone marrow metastatic disease. MAGNETOM Flash 2017; 69(3): 38–42.

Contact

Dr. Danoob Dalili
Specialist Registrar Clinical Radiology
Imperial College Healthcare NHS Trust
St Mary's Hospital
Praed St
London W2 1NY
United Kingdom
Phone: +44 (0) 20 3312 6666
Dalili@doctors.org.uk

Prof. Anwar R. Padhani
Consultant Radiologist and
Professor of Cancer Imaging
Paul Strickland Scanner Centre
Mount Vernon Cancer Centre
Rickmansworth Road
Northwood, Middlesex HA6 2RN
United Kingdom
Phone (PA): +44-(0) 1923-844751
Fax: ++44-(0) 1923-844600
anwar.padhani@stricklandscanner.org.uk

Whole-body MRI at 1.5T – a How-to Guide, .exar1 protocol file and a video

Whole-body MRI has been used at Paul Strickland Scanner Centre (Northwood, UK) for over 10 years. In that time over 4000 examinations have been performed using a protocol designed to enable the detection and surveillance of metastatic bone and soft tissue disease.

Will McGuire, Deputy Superintendent MRI Radiographer, shares his protocol along with a video demonstrating the use of this protocol.

Visit **www.siemens.com/wb-mri** to download the material.

Whole-body MRI at 1.5T – step-by-step

Will McGuire; Linda Culver; Anwar R. Padhani

Paul Strickland Scanner Centre, Mount Vernon Hospital, Northwood, Middlesex, UK

Whole-body MRI (WB-MRI) is a hot topic – you may have had enquiries from colleagues asking you if or when you might be able to offer the service. You may not know where to start or what is involved. The purpose of this article and the accompanying video tutorial is to introduce and guide you through the implementation for successful completion of a MET-RADS compliant WB-MRI protocol [1].

WB-MRI has been used as a clinical tool at Paul Strickland Scanner Centre for over 10 years. In that time over 6,500 patients have been examined using a protocol designed to enable the detection and surveillance of metastatic bone and soft tissue disease. Treatment regimens are routinely being altered based on serial qualitative and quantitative measurements produced by this technique [2].

To enable the serial analysis of quantitative ADC measurements we must reduce acquisition variables as far as practicable. Clearly it is not possible to fully control all patient variables between visits. The patient's condition may change, requiring a different coil set-up.

Adjusting scan parameters at a visit-by-visit basis adversely affects the reproducibility of both the qualitative and quantitative results. For the majority of sequences described below it is advised that the parameters are not adjusted by operators after initial protocol set-up. The sequences should be designed and saved to accommodate your largest (A>P and R>L) and tallest (H>F) patients by default, and ranges should not be reduced (e.g. phase FOV) even when this may normally prove advantageous. Those parameters which may be altered on a per-patient basis will be mentioned. Any changes made should remain constant between visits in the same patient where practicable.

Let's look at the equipment, preparation and steps required to successfully execute a WB-MRI protocol suitable for quantitative analysis.

You can find a video tutorial demonstrating the use of this protocol on the website at **www.siemens.com/wb-mri**. The video begins at the acquisition stage.

Sequence / stations	Core, comprehensive or both	TR (ms)	TE (ms)	FOV (mm)	Phase FOV (%)	Slices	Slices (mm)	Gap (%)	Matrix	Phase enc. direction	iPAT	b-values	Averages	TA (mins)
FastView	Both	3.31	2.19	480 x 1250	87.5	1	5	100	96	A>P	n/a		n/a	0:35
STIR spine sag (x2)	Both	5110	69	380	100	15	4	20	384	H>F (over-sampled)	2		2	2:30 (x2)
T1 spine sag (x2)	Both	200	9.6	380	100	15	4	20	256	H>F (over-sampled)	2		2	1:07 (x2)
T1 Dixon TimCT ax	Both	130	2.38 4.76	430 x 1015	81.3	12	5	0	256	A>P	2		1	3:45 + BHs
DWI (x4) ax	Core (Comprehensive)	7370	66	430	90.6	55	5	0	128	A>P	2	50, (600,) 900	2, (5,) 6	3:04 (4:55)
T1 Dixon CAIPI VIBE cor (x3)	Both	6.64	2.39 4.77	450	94.4	144	2	min	288	R>L (over-sampled)	5		1	0:19
T2 HASTE TimCT	Comprehensive	1000	81	430 x 1035	81.3	16	5	0	256	A>P	3		1	3:44
													Total examination time	**24:47**
													Comprehensive acquisition time	**35:55**

Table 1: Sequence parameters for MET-RADS compliant sequences for both core and comprehensive protocols at 1.5T [1].

Coil requirements

- Standard posterior spine coil
- Standard head & neck coil
- 2x anterior Body 18 coils (Fig. 1) as required for coverage to mid-thigh (3x recommended)

Number your Body coils and routinely positioning them in the same order will limit any sensitivity variability and also make coil troubleshooting much more straightforward.

It is important to note that the range required for MET-RADS compliant protocols is from vertex to mid-thigh (Fig. 2). Although not always required, access to 3x Body 18 coils is optimal and should accommodate even the tallest patients.

As such it's not necessary to use a peripheral coil for this protocol. If full imaging of the lower limbs is required it is advised to perform imaging separately and feet-first, allowing a bio-break for the patient.

As this technique will be used to generate quantitative ADC measurements it is especially important to ensure that the coils are working well. A coil QA program should be implemented with increased frequency of testing for the regularly used coils.

Product options and software compatibility

Product options used for this protocol are TimCT, Inline Composing and the Tim Planning Suite (set'n'go).

At **www.siemens.com/wb-mri** you can find a downloadable .exar1 file which was exported from an Avanto^{fit} running *syngo* MR E11C software.

If you are unable to import this file, please see the full protocol in Table 1 or the full protocol .pdf file which is available on the website.

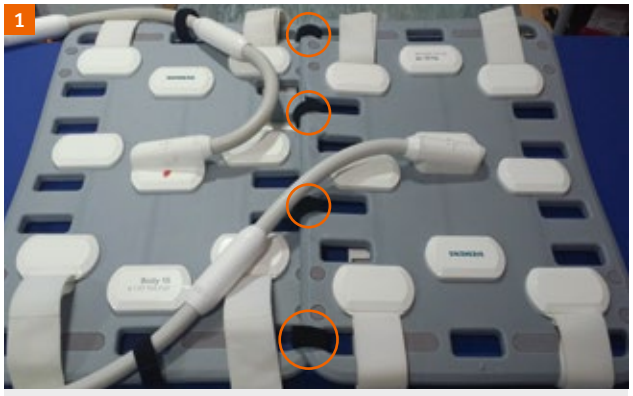

Figure 1: Improving workflow
Two Body 18 coils linked with Velcro loops (circled). This improves the reproducibility of positioning and reduces set-up time while remaining flexible.

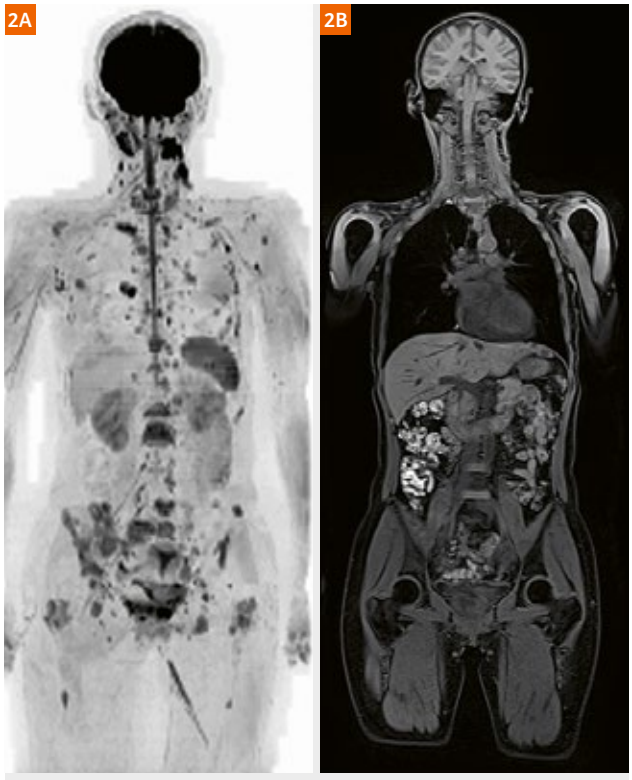

Figure 2: Range of imaging required
(2A) Coronal b900 MIP projection and **(2B)** composed coronal Dixon water images illustrating the vertex to mid-thigh range of coverage for this protocol.

Patient and equipment set-up

Patient comfort is absolutely critical to compliance with this protocol, so utilize any equipment required for comfort (e.g. extra padding, pillows, knee pad, etc.).

The patient should be advised to use the toilet where possible because the full protocol can take up to one hour.

Patients will warm up – particularly when scanning at 3T – and so the patient should wear a gown or entirely metal-free light clothing. Ensure adequate air flow to reduce the impact of heating.

Find out if the patient is able to hold their breath – if they can, use a breath-hold technique when scanning the chest and abdomen to reduce motion artifacts.

An optimal set-up includes the use of the anterior Head/Neck coil however this may not always be possible if the patient is kyphotic (Fig. 3).

Position the patient's head-first, with arms down by their side. The patient should be asked to move so that their shoulders are as close to the Head/Neck coil as possible, minimising any gap.

Place and secure anterior Body coils as required for coverage to mid-thigh. The superior margin of the first Body coil should be in line with SP1 as marked on the table-top.

As always, provide your patient with the call buzzer and adequate hearing protection.

Occasionally, due to patient body habitus, it may be necessary to place the first anterior Body coil overlapping the anterior part of the Head/Neck coil to ensure comfort.

Remember to make detailed notes of the patient set-up on their scanning record and ensure repeat visits use this set-up unless the patient's condition requires a change.

Use the positioning laser to set the start position to the inferior margin of the patient's chin – the FastView localizer will automatically move to begin acquiring at the vertex.

Form pads
Comfort and safety are key. Where possible, place foam padding between all contact points with coils, cables, the scanner and the table including elbows, sternum and knees.

Workstation
Before starting, make the following changes to the workstation options:

- Tim Planning UI active
- AutoCoilSelect ON
- Coupled graphics ON

Ready to go? It's time to scan.
Remember, you can follow along with the video from this point. Visit **www.siemens.com/wb-mri** to check it out.

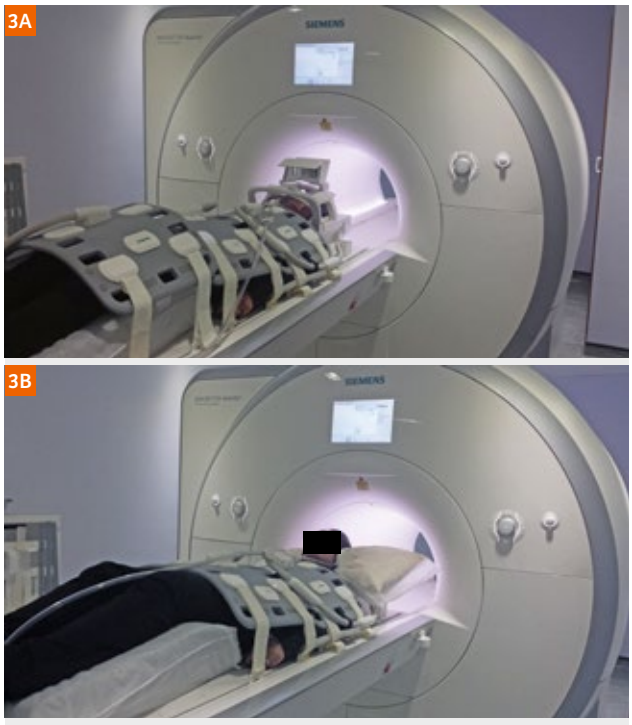

Figure 3:
(3A) Optimal coil set-up. While it is important to keep the coils as close to the patient as possible, ensuring that antorior coils remain horizontal where possible, will maximize SNR.

Position pads under the elbows and forearms.

Ensure cables do not cross over or create loops.

Use a knee pad for patient comfort – use the same pad each time for reproducibility.

(3B) Comfort set-up. Patient comfort is increased at the cost of SNR in the head, neck and distal femurs.

Table 2: Step-by-step positioning examples and acquisition tips.

Sequence details	Positioning and ranges	Acquisition tips	Adjustable parameters	Notes
Step 1 **FastView localizer** **Range:** vertex to knees **Plane:** axial (MPRs will be generated) **Method:** TimCT	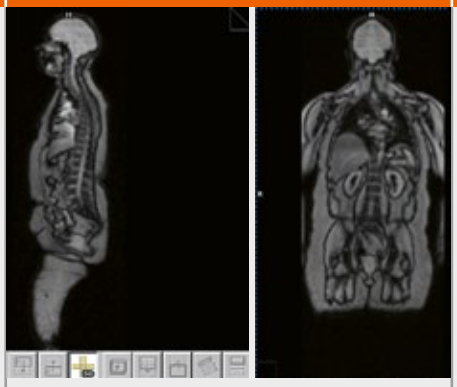	On initial set-up, set the acquisition range to as far as your table movement range will allow TimCT adjustments are enabled: this sequence will perform imaging, 3D shim and TimCT adjustments (3x movements) Where not available: utilize a set'n'go multi-planar localizer covering head to knees Once the images have been reconstructed, begin planning the spine sequences		Until this sequence has fully completed the location of the anterior coils will not display on-screen **Important: Don't proceed with planning beyond spinal imaging until the anterior coils are visible**
Step 2 **STIR and T1 spine** **Range:** whole spine **Plane:** sagittal to patient's anatomy **Method:** set'n'go	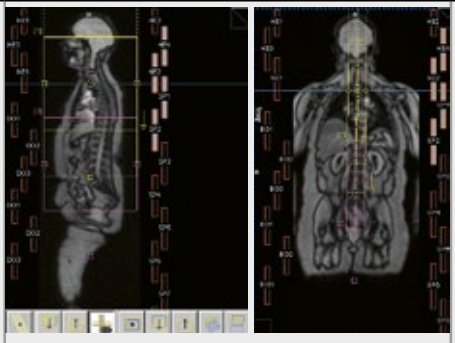	Set'n'go with automatic composing enabled H>F coverage from skull base to at least S3 Angle to cover the spine R>L – coupled graphics are **ON** so make this a best-fit To ensure anterior elements are not used during acquisition, at sequence set-up navigate to **System: Misc:** and set AutoCoilSelect **OFF** for both slice groups in both sequences once the required posterior elements are selected – save this into the protocol As all patients should always have their shoulders in the same position it is not usually necessary to change the active elements	Increase the number of slices to ensure full R>L coverage of the spine	Ensure the same number of slices are used for each station AND each sequence type (both STIR and T1)
			The TR may need to be increased to allow additional slices	Image contrast may be different between visits Record any changes
			The FOV may be increased in order to include at least S3 for very tall patients	Image resolution may be affected Usually this will not require matrix adjust-ments as long as the resolution remains constant between visits
WAIT until FastView localizer has fully completed before proceeding – this ensures anterior coils are visible and activate correctly with AutoCoilSelect ON				
Step 3 **T1 Dixon TimCT** **Range:** orbits to knees **Plane:** axial **Method:** TimCT Breath-holding where possible through the thorax and abdomen	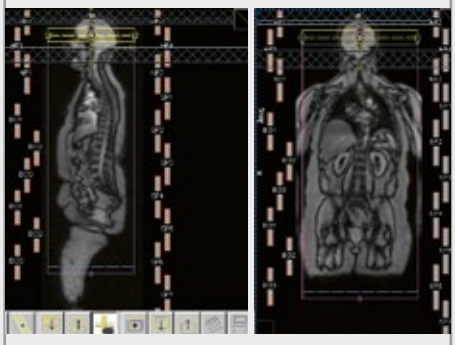	Where TimCT is not available: utilize an axial T1 Dixon set'n'go technique Adjust the position of the volume to ensure A>P coverage, equal R>L coverage using humeral heads as a guide, and ensure the blue isocenter line lies just inferior to the skull vertex (this allows the sequence to run – it may fail to start if not positioned in this manner) The volume will therefore not cover the entire brain – other sequences are included for this purpose If performing breath-holds: utilize the manual start-stop function to perform breath-holds while imaging the thorax and liver	Extend range as required to cover to mid-thigh	Detail the range selected on the patient's record to ensure reproducibility on future visits

Sequence details	Positioning and ranges	Acquisition tips	Adjustable parameters	Notes
Step 4 **Multi-b-value DWI** **Range:** vertex to knees **Plane:** axial **Method:** set'n'go	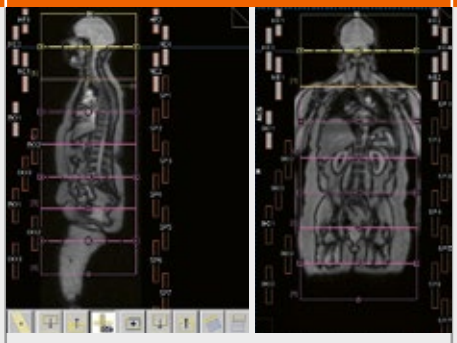	Adjust position of the set'n'go slice groups to ensure coverage from the skull vertex superiorly to at least mid-thigh inferiorly In the rare event that this range is insufficient, add another slice group (including overlap where required) Adjust position of slice groups to ensure A>P coverage, equal R>L coverage using humeral heads as a guide Manually activate the B01 element group on the first slice group – this will increase signal in the neck region		If using a fixed-frequency technique, ensure this value is copied or noted in order that it can be applied to the subsequent slice groups, however this should NOT be recorded on the patient's record as this value will necessarily change between visits A useful tip is to save this frequency as an image comment for the slice group
Step 5 **T1 Dixon CAIPIRINHA VIBE** **Range:** vertex to knees **Plane:** coronal **Method:** set'n'go Breath-holding where possible	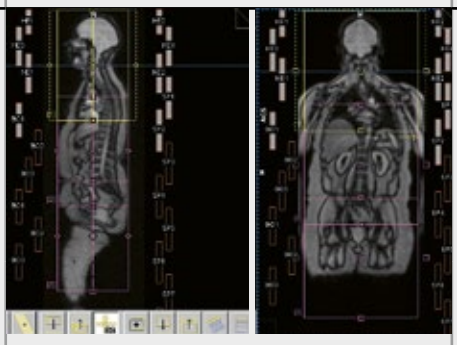	Adjust position of slice groups to ensure A>P coverage, equal R>L coverage using humeral heads as a guide. In the H>F direction, ensure some air is included superior to the skull vertex to ensure full coverage of this structure If performing breath-holds: utilize manual or auto-matic breath-hold instructions as required	Slices per slab: increase to ensure full A>P coverage if this is insuf-ficient by default Partial Fourier: use to decrease acquisition time for breath-holds where required	Your acquisition time will increase It may be necessary to introduce some partial fourier to control this Be conscious of the impact on SNR
Step 6 **T2 HASTE TimCT** **Range:** orbits to knees **Plane:** axial **Method:** TimCT	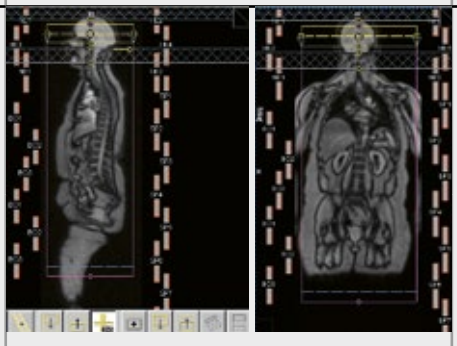	Where TimCT is not available: utilize an axial T2 HASTE set'n'go technique As this uses a copy reference from the T1 TimCT sequence it is not necessary to change the position of the volume, although care should be taken that the same range is acquired If the sequence fails to start, it is likely that a small 'footwards' change in the position of the slice group will allow it to run	Extend range as required to cover to mid-thigh	Detail the range selected on the patient's record to ensure repro-ducibility on future visits

Sequence selection and discussion

If you are using the downloadable .exar1 protocol you will find sequences which have been included and optimized based upon the experience of scanning around 30 whole body examinations each week.

You should expect the protocol to take anywhere between 30 to 60 minutes depending on what is included.

Please see the MET-RADS document [1] for the clinical justification of sequences included, however it may be helpful to touch briefly upon how the sequences have been optimized and how they can be used clinically.

Spine sequences (STIR and T1-weighted):
Both sequences are used to detect and characterize bone lesions. High-resolution STIR imaging can also help to differentiate between active and inactive metastases. In our experience, T2 imaging without fat suppression does not provide significant additional diagnostic data.

Whole-body sequences (T1 Dixon and T2 HASTE):
The multiple contrasts generated by a T1 Dixon sequence can be used to calculate the signal fat fraction (F%). This can be used to quantitatively assess response to treatment or disease progression. Flip angles have been selected to optimize T1 weighting; PD-weighted fat fractions may prove more accurate for F% estimates, but this comes at the expense of loss of the T1 contrast.

T2 HASTE imaging (in this case without fat suppression) facilitates the localization and characterization of pathologies. Asking patients to hold their breath during acquisition through the thorax and liver may improve detection of thoracic lesions or liver metastases; as such acquisition times have been kept to a minimum. The whole body axial T1 Dixon or T2 HASTE range can be acquired in under 4 minutes using TimCT where available.

Diffusion-weighted imaging:
Optimized for maximum signal generation, this sequence makes up the majority of the acquisition time. Depending on the capabilities of the scanner it is not unusual for each slice group to require over five minutes of acquisition time.

A STIR technique is used due to the improved fat suppression over a large FOV – although some centers have reported success using a SPAIR technique.

55 slices are acquired per slice group; any more and ADC values on end-of-group slices do tend to 'falsely'

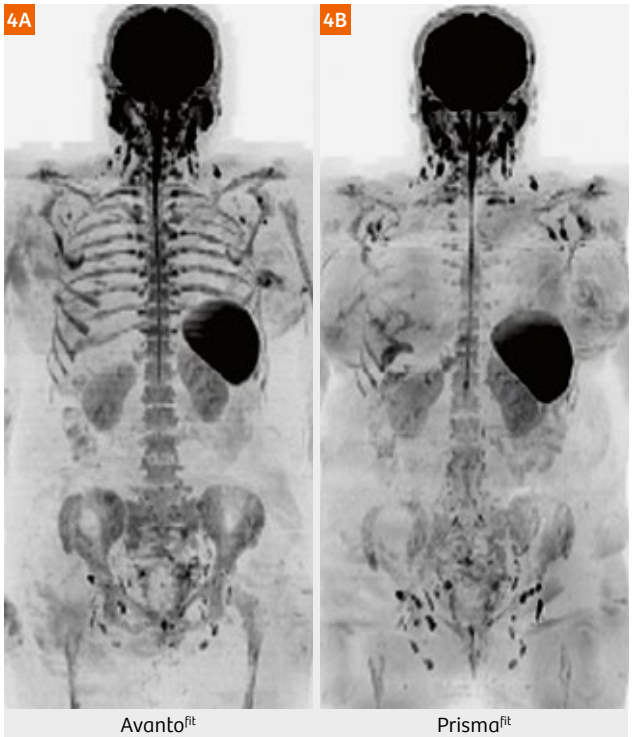

Avanto^{fit} Prisma^{fit}

Figure 4: Coronal projections of b900 MIP with inverted greyscale
Images from a patient scanned at both **(4A)** 1.5T and **(4B)** 3T. Greater signal intensity of bone marrow is demonstrated at 1.5T due to the lower susceptibility effects of bone.

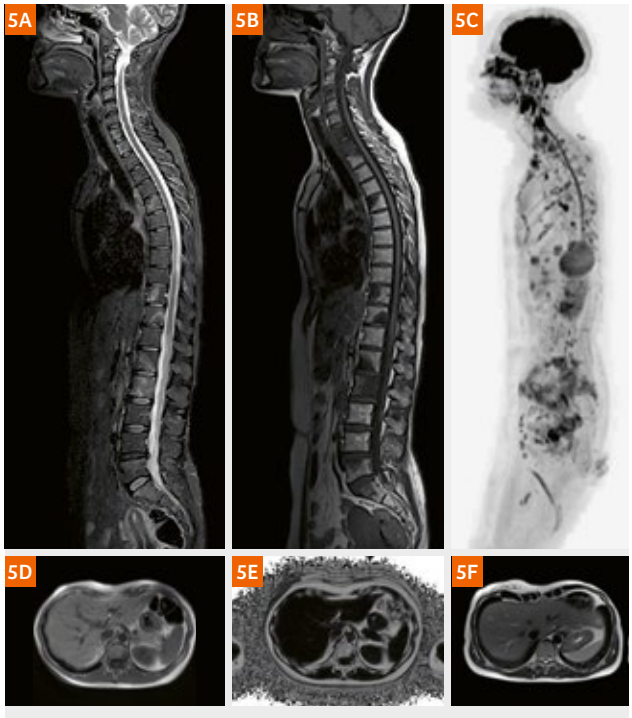

Figure 5: Example images from a completed dataset
(5A) Composed STIR and **(5B)** T1w spine images, **(5C)** sagittal projection of inverted b900 MIP, **(5D)** in-phase T1w Dixon and **(5E)** corresponding F%, **(5F)** T2w HASTE axial.

drift beyond acceptable margins [3]. An overlap can be introduced to counter this effect, although this is subject to optimization.

The optimal number of slices, and fat suppression technique, is entirely scanner-dependent and should be decided upon following rigorous testing and comparison (for example, acquiring fewer slices per station when using a shorter magnet).

Three b-values are used to optimize ADC calculation with the lowest set at b = 50 mm^2/s. For the core protocol, two b-values are sufficient, thereby reducing the acquisition time (Table 1).

Asymmetric averaging is used to optimize acquisition time while ensuring sufficient SNR at higher b-values.

The **image scale correction** factor **(System: TxRx:)** is set at 3.5, optimizing the visual appearance of hypercellular lesions versus normal bone marrow on the high b-value images.

Diffusion schemes vary between imaging centers, however we have settled on a 3D diagonal, monopolar scheme for maximum signal generation with a minimal TE. Anisotropy-sensitive techniques are unnecessary.

Eddy currents and geometric distortions, while increased using this technique, are compensated for by using the newly-released SliceAdjust feature which allows for slice-specific shimming [4]. This technique is recommended where available.

Unfortunately, the downloadable .exar1 protocol does not feature this particular sequence due to licensing and compatibility issues. Manually apply the center frequency used for the first DWI station to all subsequent stations to avoid the so-called **'broken spine'** artifact [5]. The .exar1 protocol has been set-up to allow frequency-fixing and features a 3-scan trace diffusion scheme to reduce the effect of geometric distortions where SliceAdjust is not available.

Scanning patients on different scanners is not recommended – especially at different field strengths (Fig. 4).

Contact

Will McGuire
Deputy Superintendent Radiographer
Paul Strickland Scanner Centre

Northwood
UK
will.mcguire@stricklandscanner.org.uk

Post-processing

T1-weighted fat fractions (F%) should be generated from both the TimCT and coronal VIBE series. Add the FAT and WATER series together, and then divide the FAT by the ADD. Using a scaling factor of 1000 it is possible to window more finely. Using a ROI it is possible to read off the percentage of fat in an area which can be used to monitor response of bone metastases and liver fat condition.

Coronal MPRs and radial MIPs, generated from the highest b-value series, can be used during reporting but often serve as a very visual means of communicating findings to clinical colleagues. Generate coronal MPRs at 5 mm thickness and the radial MIPs every 3 degrees (120 images) displayed using an inverted grey-scale.

Conclusion

The tricky part with WB-MRI is the initial set-up – don't be surprised if your first efforts don't produce the results you expect. A typical completed data set (Fig. 5) can consist of over 6,000 images depending on the sequences chosen and reconstructions performed, but once the protocol is in place it's fairly straight-forward for operators to perform. In our experience, treating each examination as an experiment rather than a scan will lead to success.

Keep up to date at **www.siemens.com/wb-mri** for the latest news, case studies and the video tutorial.

Acknowledgements

Many thanks to everyone involved in the development of this protocol over the years including colleagues past and present from Paul Strickland Scanner Centre, The Institute of Cancer Research and Siemens Healthineers UK and Germany.

References

1 Padhani AR, Lecouvet FE, Tunariu N, et al. METastasis Reporting and Data System for Prostate Cancer : Practical Guidelines for Acquisition, Interpretation, and Reporting of Whole-body Magnetic Resonance Imaging-based Evaluations of Multiorgan Involvement in Advanced Prostate Cancer. Eur Urol. European Association of Urology; 2017;71:81–92.
2 Kosmin M, Makris A, Joshi PV, et al. The addition of whole-body magnetic resonance imaging to body computerised tomography alters treatment decisions in patients with metastatic breast cancer. Eur J Cancer; 2017;77:109-116
3 Winfield JM, Collins DJ, Priest AN, et al. A framework for optimization of diffusion-weighted MRI protocols for large field-of-view abdominal-pelvic imaging in multicenter studies. Med. Phys; 2016;43:95–110
4 Haibo Z, Huadan X, Stemmer A, et al. Slice Specific Shimming Improves the Image Quality of Whole-Body Diffusion-Weighted Examinations at 3T. Magnetom Flash; 2017: Magnetom Vida special issue;17-21
5 Koh DM, Blackledge M, Padhani AR, et al. Whole-Body Diffusion-Weighted MRI: Tips, Tricks, and Pitfalls. AJR; 2012;199:252-262

Visit **www.siemens.com/wb-mri** to find the video tutorial.

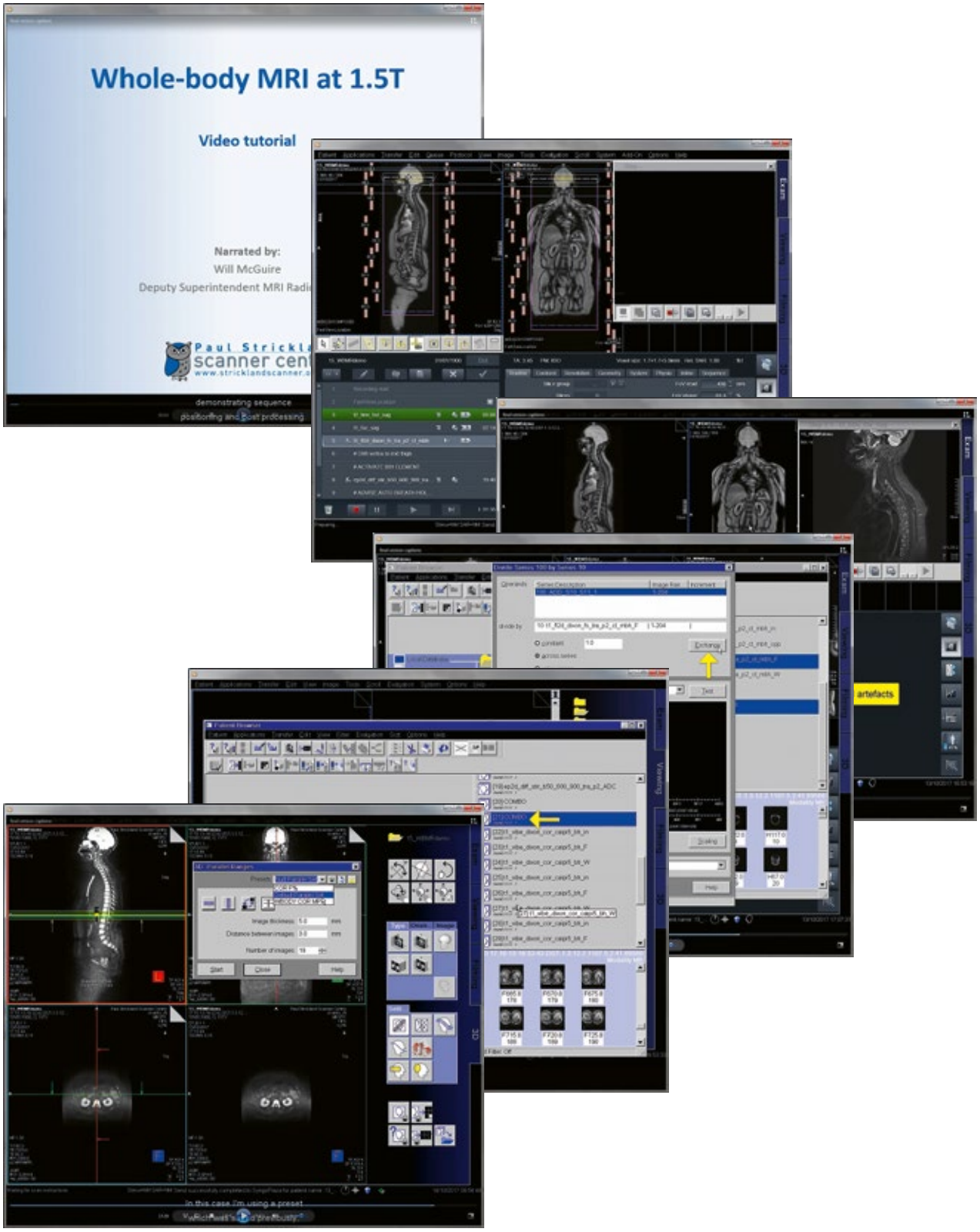

Diffusion and perfusion MR parameters to assess preoperative short course radiotherapy response in locally advanced rectal cancer: a comparative explorative study among parameters derived from standardized index of shape DCE-MRI, intravoxel incoherent motion, and diffusion kurtosis imaging

Antonella Petrillo[1]; Roberta Fusco[1]; Mario Sansone[2]; Vincenza Granata[1]; Robert Grimm[3]; Daniela Rega[4]; Paolo Delrio[4]; Francesco Bianco[4]; Massimiliano Di Marzo[4]; Fabiana Tatangelo[5]; Antonio Avallone[6]; Biagio Pecori[7]

[1] Division of Radiology, Istituto Nazionale Tumori (IRCCS) Fondazione G. Pascale, Naples, Italy
[2] Division of Information Technology and Electrical Engineering (DIETI), Naples, Italy
[3] Siemens Healthineers, Erlangen, Germany
[4] Division of Gastrointestinal Surgical Oncology, Istituto Nazionale Tumori (IRCCS), Fondazione G. Pascale, Naples, Italy
[5] Division of Diagnostic Pathology, Istituto Nazionale Tumori (IRCCS), Fondazione G. Pascale, Naples, Italy
[6] Division of Gastrointestinal Medical Oncology, Istituto Nazionale Tumori (IRCCS), Fondazione G. Pascale, Naples, Italy
[7] Divion of Radiotherapy, Istituto Nazionale Tumori (IRCCS), Fondazione G. Pascale, Naples, Italy

Abstract

Purpose
To assess preoperative Short Course Radiotherapy (SCR) tumor response in locally advanced rectal cancer (LARC) by means of parameters derived from Standardized Index of Shape (SIS) dynamic contrast-enhanced (DCE) MRI, Apparent Diffusion Coefficient (ADC), Intravoxel Incoherent Motion and Diffusion Kurtosis Imaging derived parameters by diffusion-weighted (DW) MRI.

Materials and methods
34 patients with LARC were enrolled for the study. The participants underwent MRI before and after SCR, followed by delayed surgery, retrospectively. SIS, ADC, tissue diffusion (Dt), pseudo-diffusion (Dp), perfusion fraction (fp), mean diffusivity (MD), and mean diffusional kurtosis (MK) were calculated for each patient. After surgery, the pathological TNM and tumor regression grade (TRG) were estimated. For each parameter, percentage changes between the values before and after SCR were evaluated. Non-parametric sample tests and receiver operating characteristic curve (ROC) analysis were performed.

Results
15 patients were classified as responders (TRG ≤ 2) and 19 as non-responders (TRG > 3). Seven patients had TRG 1 (pathological complete response, pCR). A Mann-Whitney test showed statistically significant differences only for the percentage change in SIS median values between responder and non-responder patients and between complete and incomplete pathological response (p value << 0.001). The best result to differentiate responders from non-responders and to assess complete pathological response was achieved by SIS with an accuracy of 89% and an area under the ROC curve of 0.95 and 0.88, respectively. A high accuracy (74%) was also obtained by perfusion fraction to detect pathological complete response after SCR with an area under the ROC of 0.70.

Conclusion
SIS is a promising DCE-MRI angiogenic biomarker for assessing preoperative treatment response after SCR with delayed surgery and it permits to discriminate pCR allowing to direct surgery for tailored and conservative treatment. However, parameters derived from IVIM and DKI reflect tissue response changes and could be used to assess pathological response in LARC after SCR.

Introduction

Total mesorectal excision combined with preoperative radiation therapy and chemotherapy (pCRT) is the current standard procedure for locally advanced rectal cancer (LARC) [1–3]. Long-course CRT has been extensively applied and results from this approach have been encouraging in terms of local control with a high percentage of tumor regression up to a significant complete response rate [1–3]. However, Short Course Radiotherapy (SCR) is known to be a valuable therapeutic option in patients with LARC. A recent meta-analysis [4] reported that SCR with immediate surgery is as effective as long CRT with deferred surgery in terms of overall and disease-free survival rates, local and distant control, and toxicity. Also, Short Course Radiotherapy with Delayed Surgery (SCRDS) (after 4~8 weeks), an optional therapy prescribed for patients with locally advanced tumors who are not fit for CRT, leads to similar results in terms of the percentage of patients with a negative margin resection and satisfactory results with regard to the downstaging and pathological response rate compared to traditional preoperative CRT [5–13].

The use of new imaging modalities to make individual assessments of therapy response could be of great clinical value to enable subsequent strategies to be tailored to each patient. Such strategies range from a tailored surgical approach, to administering an adjuvant regimen, or even a wait-and-see policy without surgery for patients with high surgical risks [14, 15].

A positive tumor response will not necessarily correspond to a significant tumor size reduction using morphological MRI [16]; it is difficult to differentiate between necrosis, fibrotic tissue, and viable residual tumor tissue within the treated areas [16, 17]. Several studies have focused on the potential added benefit of functional quantitative parameters derived from MR images [17–20]. Dynamic contrast-enhanced MRI (DCE-MRI) has proven promising for the detection of residual tumor following pre-surgery CRT [17–21]. Earlier studies investigated the functional parameters derived from DCE-MRI data in rectal cancer [18–21] such as the Standardized Index of Shape proposed by Petrillo et al. [18] as a simple semi-quantitative parameter to differentiate responders from non-responders after CRT in LARC, and preoperative treatment response after SCRDS [22]. Moreover, in various oncology fields, researchers have recommended the use of diffusion-weighted imaging (DWI) to assess treatment response [23–30]. DWI provides functional information on tissue microstructure by evaluating water proton mobility differences [23, 24]. Water diffusion characteristics depend on cell density, vascularity, viscosity of the extracellular fluid and cell membrane integrity. By quantifying these properties by means of the individual apparent diffusion coefficient (ADC), using a mono-exponential model to analyze DWI data, it can be employed as an imaging biomarker to detect biological tumor changes and to monitor and predict treatment response [25, 26]. Moreover, using a bi-exponential model to analyze DWI data, we can obtain information on both diffusion and perfusion tissue properties derived from Intravoxel Incoherent motion method (IVIM): the pure tissue coefficient (D) that describes macroscopic motion of water in the cellular interstitial space, the pseudo-diffusion coefficient (Dp) that describes the microscopic motion of blood in the vessels, and the perfusion fraction (fp) that describes the proportion of two different motions [27–30].

Also, the conventional DWI model is based on the assumption that water diffusion within a voxel has a single component and exhibits Gaussian behavior where water molecules diffuse with no restrictions [31]. However, due to the presence of microstructures (i.e., two tissue types or components within one voxel, organelles, and cell membranes), random motion or diffusion of thermally agitated water molecules within biological tissue exhibits non-Gaussian behavior [32]. In 2005, Jensen and colleagues proposed a non-Gaussian diffusion model entitled Diffusion Kurtosis Imaging (DKI) [32]. This model includes the kurtosis coefficient (K), which measures the deviation of tissue diffusion from a Gaussian model, and the diffusion coefficient (D) with the non-Gaussian bias correction.

The aim of this study is to determine the diagnostic performance of MR imaging for the assessment of tumor response after SCRDS in patients with LARC using Standardized Index of Shape (SIS) obtained from DCE-MRI, using parameters derived from ADC, IVIM, and DKI obtained from DW-MRI.

Material and methods

Patient selection

34 patients with a median age of 67 years (range 48–83 years) who refused or were considered unfit for chemo radiation and planned for neoadjuvant Short Course Radiotherapy, were evaluated in this retrospective study, conducted from May 2011 to December 2016.

Patient characteristics are described in Table 1.

All patients had a biopsy-proven rectal adenocarcinoma. Endorectal ultrasonography, MRI of pelvis and Computed Tomography (CT) scan of the chest, abdomen, and pelvis were used as staging examinations. Patients had T2-T3 rectal cancer with and without local lymph node involvement. Patients staged T2 without lymph node involvement were included only if the tumor was located less than 5 cm from the anal verge. Exclusion criteria were:

Characteristics	All patients n = 34 (%)	TRG 1–2 n = 15	TRG 3–4 n = 19	p*
Gender				> 0.05
Male/Female	26 (76.5) 8 (23.5)	10/5	16/3	
Median age (range)	67 (48–83)	69 (48–78)	68 (48–76)	
Gunderson Risk				> 0.05
Intermediate: T3N0, T2N1	8 (23.5)	3	5	
Moderately high: T2N2, T3N1, T4N0	17 (50.0)	7	10	
High: T3N2	9 (26.5)	5	4	
Distance from the anal verge				> 0.05
≤ 5 cm	14 (41.2)	6	8	
> 5 cm	20 (58.8)	9	11	
Circumferential resection margin				> 0.05
> 2 mm	15 (44.1)	6	9	
≤ 2 mm	13 (38.2)	6	7	
≤ 1 mm	5 (14.7)	2	3	
Not measurable	1 (2.9)	0	1	

Table 1:
Patient characteristics and histopathological findings.

inability to give informed consent, previous rectal surgery, and contraindications to MRI or to the administration of MR contrast media. Patients were included in the study in accordance with the approved guidelines of the Ethical Committee of the National Cancer Institute of Naples and gave their written informed consent.

Radiotherapy

All patients underwent dose-planning CT in prone position. After an online CT virtual simulation, CT datasets were transferred to a dedicated treatment planning system through a DICOM network and an individualized clinical target volume (CTV) was calculated, including the gross tumor volume with margins (2–3 cm depending on tumor position, identified by MRI imaging), the mesorectum, and regional lymph nodes depending on tumor location. We contoured the small bowel, the femoral heads, and the bladder as critical organs on all CT slices for every patient, and we evaluated the relative dose-volume histogram on the treatment planning console. Three-dimensional plans for 3D or Intensity-Modulated Radiation Therapy (IMRT) radiotherapy were generated for dual-energy, 6–20 MV X-rays, (Clinac 2100, Varian Medical Systems, Palo Alto, CA, USA), or 6–15 MV X-ray linear accelerator (Elekta Agility, Elekta Instrument AB Stockholm, Sweden) both equipped with multileaf collimators (MLC). Patients were scheduled using a 3-field or IMRT treatment arrangement to include the planning target volume within the 95% isodose. A dose of 25 Gy in 5 fractions over 1 week was prescribed to the ICRU 62 intersection point.

MRI data acquisitions

Each patient underwent MR studies before and after SCR: baseline, on average 23.8 days before starting radiotherapy and delayed, on average 61.0 days after the end of SCR. MR imaging was performed with a 1.5T scanner (MAGNETOM Symphony, Siemens Healthcare, Erlangen, Germany) equipped with a phased-array body coil. Patients were placed in a supine, head-first position. Mild rectal lumen distension was achieved with 60–90 mL of undiluted Ferumoxsil (Lumirem, Guerbet, Roissy, France) suspension introduced per rectum. Pre-contrast coronal T1w 2D turbo spin-echo (TSE) images and sagittal and axial T2w 2D turbo spin-echo images of the pelvis were obtained. Axial DWIs were then acquired (spin-echo diffusion-weighted echo-planar imaging (SE-DW-EPI) at seven b-values of 0, 50, 100, 150, 300, 600, 800 s/mm^2. Subsequently, axial, dynamic, contrast-enhanced T1w, FLASH 3D gradient-echo images were acquired. We obtained one sequence before and ten sequences, with no delay, after IV injection of 0.1 mmol/kg of a positive, gadolinium-based para-magnetic contrast medium (Gd-DOTA, Dotarem, Guerbet, Roissy, France). The contrast medium was injected using Spectris Solaris® EP MR (MEDRAD Inc., Indianola, PA, USA), with a flow rate of 2 mL/s, followed by a 10-mL saline flush at the same rate. Temporal resolution was 0.58 minutes, corresponding to 35 seconds (as reported in Table 2). Sagittal, axial, and coronal post-contrast T1w 2D turbo spin-echo images, with and without fat saturation, were then obtained (Table 2). Axial T1w pre- and post-contrast sequences were acquired at the same position as the T2w sequence. MRI total acquisition time was around 40 minutes. Patients did not receive bowel preparation, antispasmodic medication, or rectal distention before any of the MR examinations.

MR image data analysis

Image assessment was performed in a single reading session for each patient based on the consensus of two gastro-intestinal radiologists with 25 years and 10 years of experience in reading pelvic MR images.

To take into account tumor heterogeneity, based on pre-contrast T1-weighted images using the T2-weighted images as a guide [33], the radiologists manually drew regions of interest (ROI) along the contours of the tumor to obtain the DCE-MR volume of interest (VOI) for each study, covering the whole lesion with the exclusion of peripheral

Sequence	Orientation	TR/TE/FA (ms/ms/deg.)	FOV (mm x mm)	Pixel Spacing	ST/Gap (mm/mm)
T1w 2D TSE	Coronal	499/13/150	450 x 450	0.87 x 0.87	3/0
T2w 2D TSE	Sagittal	4820/98/150	250 x 250	0.78 x 0.78	3/0
T2w 2D TSE	Axial	3970/98/150	250 x 250	0.78 x 0.78	3/0
SE-DW-EPI	Axial	2700/83	270 x 230	1.70 x 1.70	4/0
T1w FLASH 3D, pre-contrast	Axial	9.8/4.76/25	330 x 247	0.59 x 0.59	3/0
T1w FLASH 3D, post-contrast	Axial	9.8/4.76/25	330 x 247	0.59 x 0.59	3/0
T1w 2D TSE	Sagittal	538/13/150	250 x 250	0.48 x 0.48	3/0
T1w 2D TSE	Coronal	538/13/150	250 x 250	0.48 x 0.48	3/0
T1w 2D TSE	Axial	450/12/150	270 x 236	0.52 x 0.52	3/0

Table 2:
Pulse sequence parameters in MR studies.

Abbreviations: TR = Repetition Time, TE = Echo Time, FOV = Field of View, FA = Flip Angle, ST = Slice Thickness, TF = Turbo Factor, AT = Acquisition Time

1

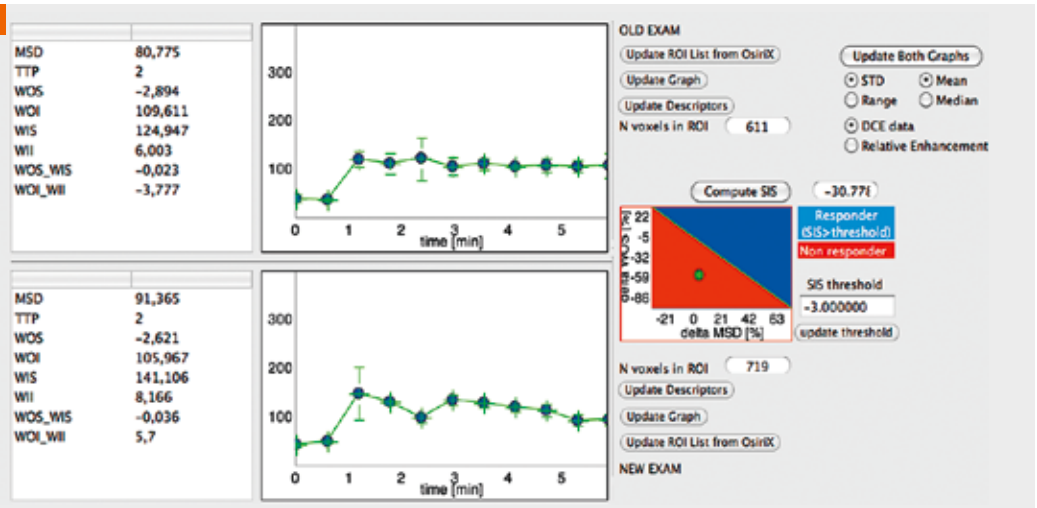

Figure 1:
SIS OsiriX plugin developed at our institution.

fat, artefacts, and blood vessels. Also, for DW-MRI, based on DWI with the highest b-value, the radiologists, manually drew regions of interest (ROI) along the contours of the tumor to obtain the DW-MR volume of interest (VOI) for each study.

For each MR descriptor, the percentage change of the mean value on the VOI between pre and post treatment was calculated as ΔX = (Xpre – Xpost) / Xpre (X is the generic shape descriptor).

No image registration was applied to the data we acquired. We took care to exclude from the analysis the slices where motion artifacts were visible. Moreover, a volumetric analysis was performed for each parameter thus minimizing errors due to voxel misalignments.

DCE-MRI features

In order to perform SIS analysis, the authors developed an OsiriX plugin (Fig. 1) [34]. Considering the segmented VOI, the maximum signal difference (MSD) and wash out slope (WOS) were calculated as reported in [35]. For the SIS analysis, we then evaluated the percentage change of MSD [$\Delta MSD = (MSD_1 - MSD_2) / MSD_1 \times 100$], of WOS [$\Delta WOS = (WOS_1 - WOS_2) / WOS_1 \times 100$] and of the two combined as described in a previous paper [18].

DWI features

For each voxel, 9 features were extracted from DWI data using the mono-exponential model, the Diffusion Kurtosis Imaging model, and Intra Voxel Incoherent Motion imaging using a conventional biexponential fitting method (CBFM).

DWI signal decay is most commonly analyzed using the monoexponential model [23, 24]:

Equation 1

$$ADC = \frac{\ln\left(\frac{S_0}{S_b}\right)}{b}$$

where S_b is the MRI signal intensity with diffusion weighting b, S_0 is the non-diffusion-weighted signal intensity, and ADC is the apparent diffusion coefficient.

For a voxel with a large vascular fraction, the MRI data decay can deviate from a monoexponential form, in particular showing rapid decay in the range of low b values generated by the IVIM effect [23, 24]. Thus, in addition to the monoexponential model, a conventional biexponential model was used to estimate the IVIM-related parameters of pseudo-diffusivity (Dp indicated also with D*), perfusion fraction (fp), and tissue diffusivity (Dt):

Equation 2

$$\frac{S_0}{S_b} = f_p \cdot \exp(-b \cdot D_p) + (1 - f_p) \cdot \exp(-b \cdot D_t)$$

Moreover, Diffusion Kurtosis imaging was included in the analysis in order to obtain the final fitted images (Mean of Diffusion Coefficient (MD) and mean of Diffusional Kurtosis (MK)).

Multi-b DW images were obtained through voxel-by-voxel fitting using the diffusion kurtosis signal decay equation (3) by applying a two-variable linear least squares algorithm as used in a previous study [32]:

Equation 3

$$S(b) = S_0 \exp\left(-b \cdot D + \frac{1}{6} b^2 \cdot D^2 \cdot K\right)$$

In this equation, D is a corrected diffusion coefficient; and K is the excess diffusion kurtosis coefficient. K describes the degree of deviation of molecular motion from the perfect Gaussian distribution. When K is equal to 0, equation (3) evolves into a conventional monoexponential equation (1):

The difference between D and ADC is that D is a corrected form of ADC for use in non-Gaussian circumstances.

The parameters of conventional DWI (ADC), IVIM (fp, Dt, Dp), and DKI (MK and MD) were obtained from the multi-b DWI data with all measured b values using the prototype post-processing software Body Diffusion Toolbox[1] (Algorithm 0 for IVIM fitting) produced by Siemens Healthcare, Erlangen, Germany.

[1] WIP, the product is currently under development and is not for sale in the US and in other countries. Its future availability cannot be ensured.

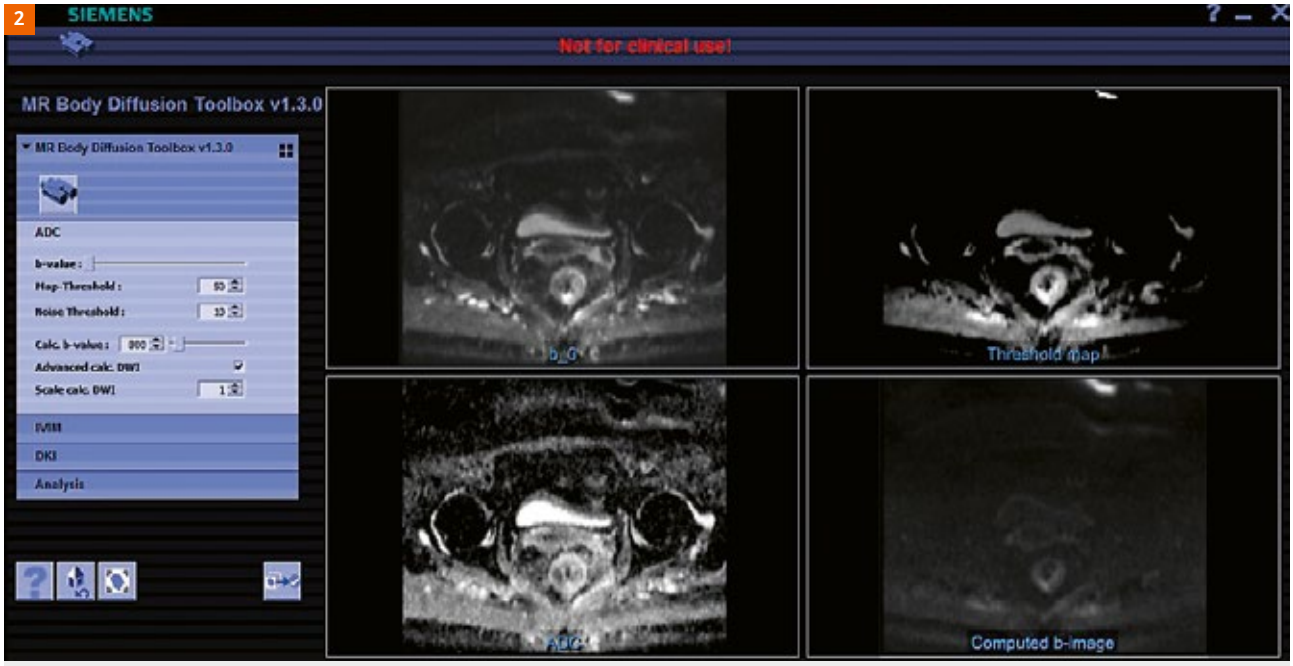

Figure 2:
Siemens Healthineers MR Body Diffusion Toolbox[1] interface.

Surgery
Surgery was performed, on average, 70.0 days after the end of radiotherapy. Based on the results of restaging and downsizing, sphincter-saving surgery was considered for all patients without clear sphincter involvement before treatment and local excision was considered for patients with a significant clinical response. The planned operation was discussed with the patients and a specific informed consent was obtained. A rectal resection with total mesorectal excision and bilateral nerve sparing, where possible, was the standard approach. In distal cancers an ultra-low anterior resection with colo-anal manual anastomosis or, in the case of sphincter involvement, an abdomino-perineal resection were performed. All patients receiving an anastomosis underwent construction of a protecting ileostomy.

Evaluation of pathologic response
Details of how the pathologic response assessment was performed have been described [36, 37]. In brief, surgical specimens containing the tumor were evaluated and scored according to tumor regression grade (TRG), as proposed by Mandard et al. [37], by an expert pathologist who was not aware of the MRI findings. A score of TRG 1 means a complete response with absence of residual cancer and fibrosis extending through the wall. TRG 2 is defined as the presence of residual cancer cells scattered through the fibrosis. TRG 3 corresponds to an increased number of residual cancer cells, with predominant fibrosis. TRG 4 indicates residual cancer outgrowing fibrosis. TRG 5 is the absence of regressive changes. Patients with a TRG 1 or 2 score were considered as responders, whereas the remaining patients (TRG 3, 4, or 5) were classified as non-responders. Patients with TRG 1 were considered as having achieved pathological complete response while patients with TRG 2–5 were considered as having incomplete pathological response [18].

Statistical analysis
A Mann-Whitney non-parametric test was performed to assess statistically significant differences between responder and non-responder patients and between pathological complete responders and incomplete responders. Receiver Operating Characteristic (ROC) curves were also used to evaluate the diagnostic performance for each parameter. The Area Under ROC Curve (AUC) was calculated and optimal thresholds were obtained by maximizing the Youden index. Sensitivity, specificity, positive predictive value (PPV), negative predictive value (NPV), and accuracy were performed considering optimal cut-off values.

A P value < 0.05 was considered significant for all tests. All analyses were performed using the Statistics Toolbox produced by Matlab R2007a (The Math-Works, Natick, MA, USA).

Results

All patients in our series had rectal adenocarcinomas. Three patients were pathologically classified as T0, 6 as T1, 20 as T2, 5 as T3. There were 7 patients with a TRG 1, 8 with a TRG 2, 11 with a TRG 3, 8 with a TRG 4, and none with a TRG 5. Therefore, 15 patients were classified as responders and 19 as non-responders according to TRG. Seven patients had pathological complete response. The results of the parameters were reported in terms of percentage changes between pre and post therapy (symbol Δ).

A Mann-Whitney test showed statistically significant differences exclusively for SIS percentage change median values between responder and non-responder patients and between complete and incomplete pathological response (p value << 0.001, Fig. 3). Figure 3 shows the boxplots for SIS in discrimination of responders from non-responders (3A) and in discrimination of complete from incomplete response (3B). Figure 4 shows the boxplots for each diffusion parameter between responders and non-responders and Figure 5 between complete and incomplete responders. Table 3 shows the change in SIS and diffusion parameters to differentiate the responders and the non-responders group and Table 4 to discriminate complete pathological response from incomplete pathological response. Results were statistically significant for every parameter (Fisher test p < 0.01). The best parameter to discriminate responders from non-responders was SIS (sensitivity 94%, specificity 84%, AUC = 0.95, cut-off value = -7.8%). For IVIM-derived parameters the best results to discriminate responders from non-responders were obtained with Dt (sensitivity 75%, specificity 74%, AUC = 0.63, cut-off value = 25.59%). SIS obtained the best diagnostic performance also to discriminate pCR (sensitivity 86%, specificity 89%, AUC = 0.88, cut-off value = 68.2%). A high AUC (0.70) was also obtained by fp to detect pathological complete response after SCR with a cut-off value = 15.32%.

Figure 6A shows ROC analysis for ΔSIS and the change in parameters derived from DW-MRI to discriminate responders from non-responders while Figure 6B shows ROC analysis for ΔSIS and change in diffusion parameters to detect complete pathological response versus incomplete pathological response.

Discussion and conclusions

In recent years, there has been growing interest in functional imaging modalities to increase diagnostic accuracy for therapy response assessment. These imaging modalities reflect the microstructural and metabolic proprieties of a tumor, allowing the evaluation of treatment-induced changes before morphological changes become apparent. DCE-MRI and DWI have emerged as

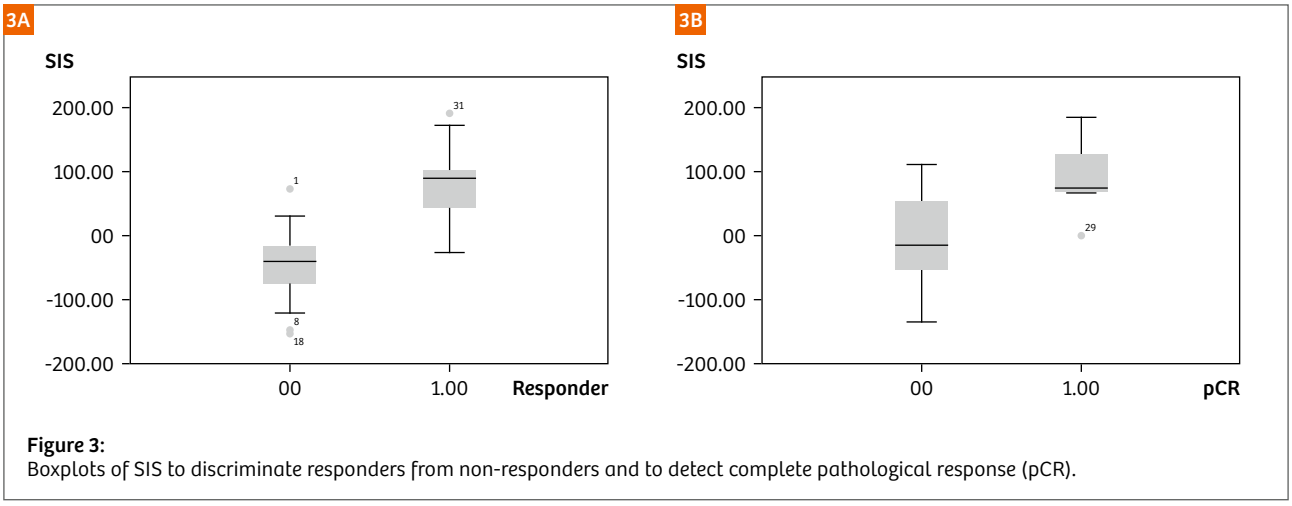

Figure 3:
Boxplots of SIS to discriminate responders from non-responders and to detect complete pathological response (pCR).

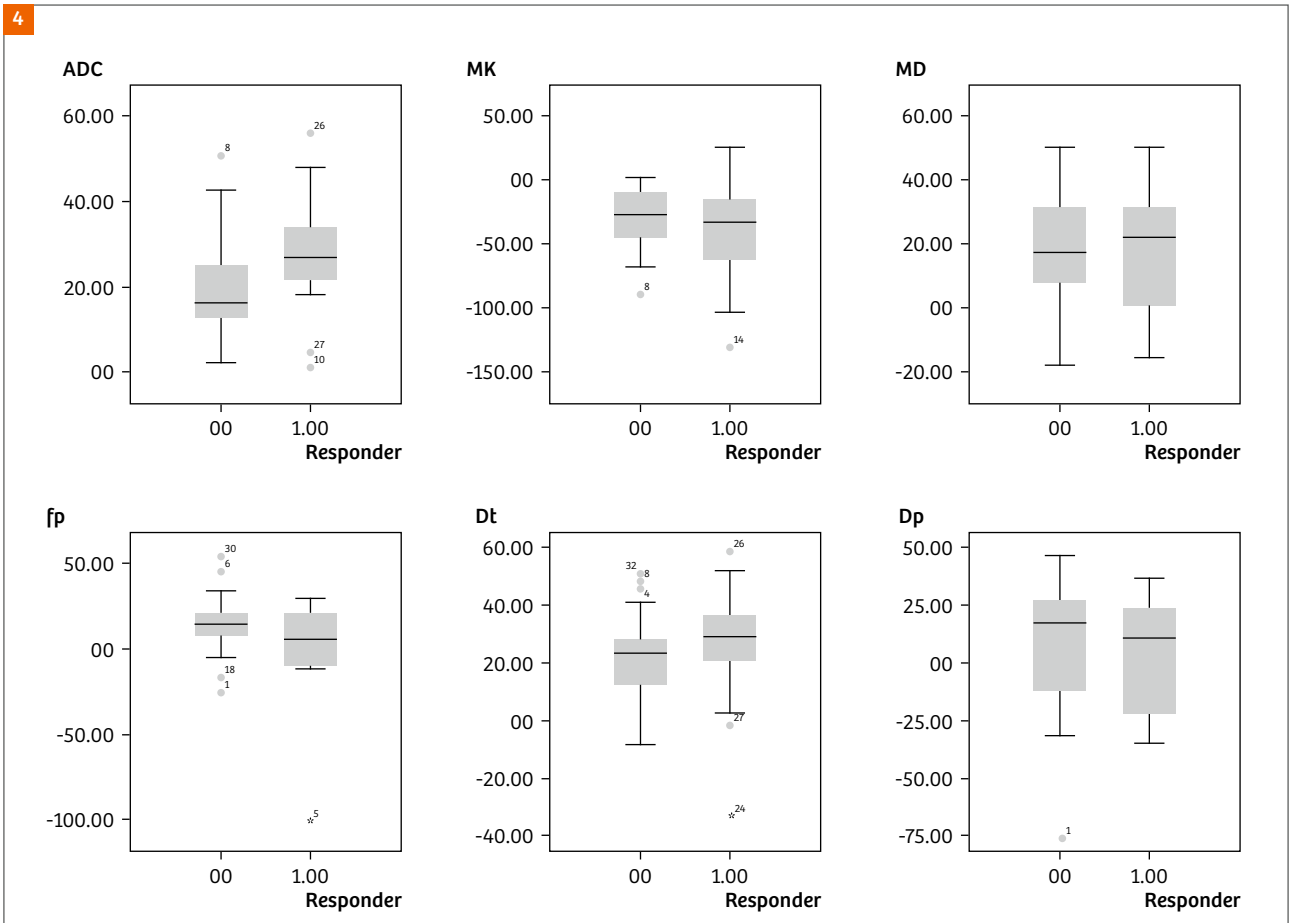

Figure 4:
Boxplots of diffusion parameters to discriminate responders from non-responders.

powerful tools for predicting and assessing neoadjuvant therapy response for rectal cancer. In fact, DCE-MR and DW-MR imaging after preoperative CRT were shown to be more valuable than morphologic MR imaging in recognizing significant and pathological complete response and in identifying residual tumor.

The objective of this study is to determine the diagnostic performance of DCE and DW imaging for the assessment of tumor response after SCRDS in patients with LARC, comparing Standardized Index of Shape (SIS) obtained by DCE-MRI and using ADC, parameters derived from Intravoxel Incoherent Motion and DKI obtained by DW-MRI. To the best of our knowledge, there are no studies in the literature focusing on a comparison of parameters derived from DCE-MRI, IVIM, and DKI to assess therapy response in locally advanced rectal cancer after SCRDS.

There are many studies that evaluate the single modality, DCE and DWI, in preoperative long CRT assessment [18–21, 38–40]. In our previous studies [18] we demonstrated the ability of DCE-MRI using the Standardized Index of Shape to discriminate responder from non-responder patients and complete pathological tumor response after CRT in LARC with a high degree of accuracy, also when compared to FDG-PET examination [41]. Several studies have already demonstrated the role of diffusion-weighted imaging in LARC for early and late assessment of therapy response [38–40] and several studies have also evaluated the use of IVIM in elaborating DW-data in different types of tumors [27–30, 42]. Moreover, there are some studies that aim to assess tumor response after SCR using metabolic change evaluations revealed by FDG-PET with contrasting results [43–46]. Two studies [45, 46] have analyzed the responses to SCR in LARC, documenting no significant metabolic responses to SCR. However, Pecori et al. [44] demonstrated that, in the course of SCR, it is possible to estimate the probability of pathological tumor responses on the basis of a logistic regression analysis of PET/CT parameters derived from three sequential studies. In another of our studies [19], we assessed parameters derived from SIS and IVIM in LARC after SCRDS, demonstrating that SIS obtained the best parameter for discriminating responders

5

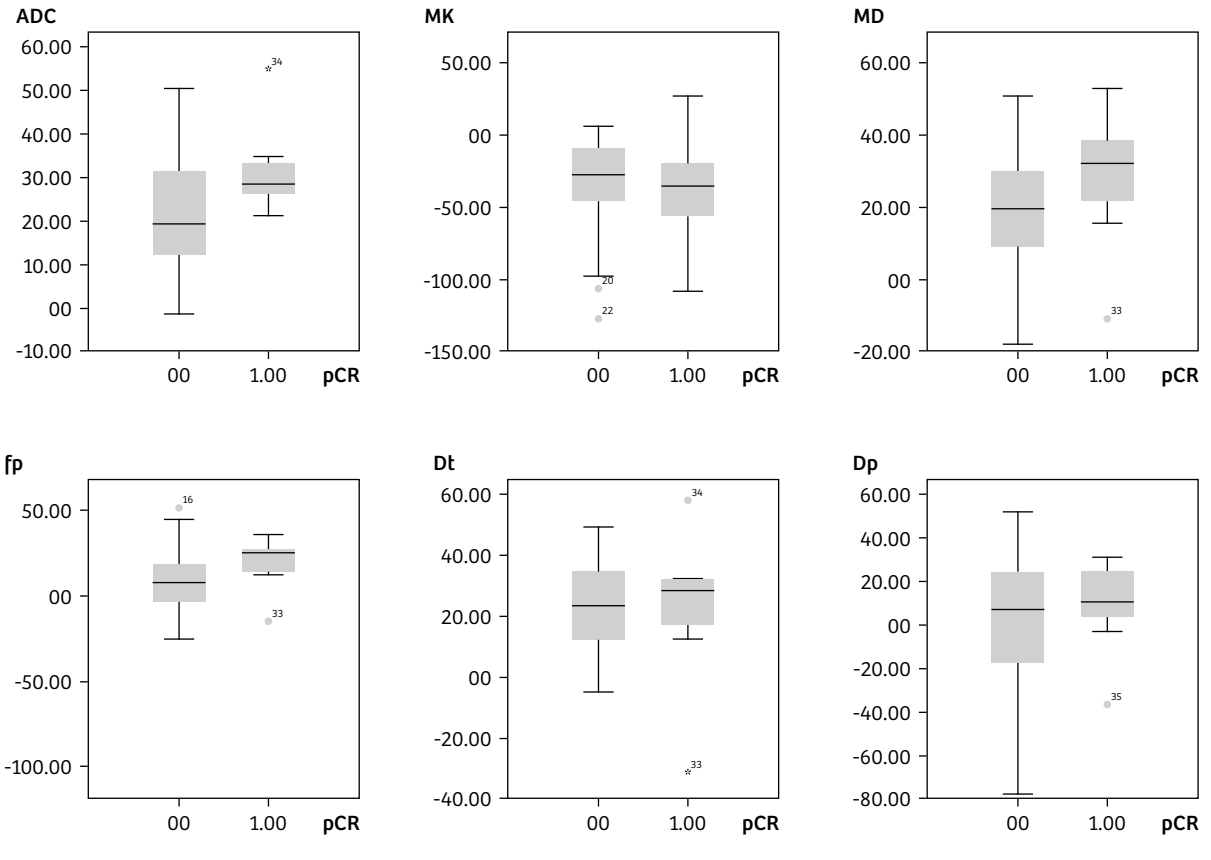

Figure 5:
Boxplots of diffusion parameters to detect complete pathological response (pCR).

from non-responders (sensitivity 94%, specificity 84%, accuracy 89%, cut-off value = -7.8%) and the best diagnostic performance also for discriminating pCR (sensitivity 86%, specificity 89%, accuracy 89%, cut-off value = 68.2%). We also demonstrated that linearly combining each possible parameter couple or all functional IVIM-derived parameters did not increase accuracy compared to SIS alone. In this study we also extrapolated parameters derived from DKI using the Siemens Healthineers MR Body Diffusion Toolbox.

Our findings showed that, on the basis of only two MRI studies (basal and preparatory), there were statistically significant differences in ΔSIS values between responder and non-responder patients and between complete and incomplete pathological response ($p << 0.01$ at Mann-Whitney test) while there were no statistically significant differences in the percentage change of the parameters derived from IVIM and DKI. The best parameter for discriminating responders from non-responders and to differentiate complete from incomplete response by ROC analysis was SIS (sensitivity 94%, specificity 84%, accuracy 89%, AUC = 0.95, cut-off value = -7.8%). However, also, ΔADC showed a good diagnostic accuracy of 71% in discriminating responders from non-responders and an accuracy of 60% in differentiating complete pathological

Responders versus non-reponders

	AUC	Sensitivity	Specificity	PPV	NPV	Accuracy	Cut-off
ADC	0.67	0.88	0.58	0.64	0.85	0.71	18.63
MK	0.37	0.06	1.00	1.00	0.56	0.57	2.19
MD	0.51	0.63	0.63	0.59	0.67	0.63	18.60
fp	0.42	0.38	0.68	0.50	0.57	0.54	15.32
Dt	0.63	0.75	0.74	0.71	0.78	0.74	25.59
Dp	0.40	1.00	0.05	0.47	1.00	0.49	-79.01
SIS	0.95	0.94	0.84	0.83	0.94	0.89	-7.76

Table 3:
Diagnostic performance of each MR-derived parameter to discriminate responders from non-responders.

Abbreviations: AUC = area under ROC curve; PPV = positive predictive value; NPV = negative predictive value

Complete versus incomplete reponders

	AUC	Sensitivity	Specificity	PPV	NPV	Accuracy	Cut-off
ADC	0.73	1.00	0.50	0.33	1.00	0.60	19.11
MK	0.40	0.14	1.00	1.00	0.82	0.83	2.19
MD	0.68	0.71	0.75	0.42	0.91	0.74	25.17
fp	0.70	0.71	0.75	0.42	0.91	0.74	15.32
Dt	0.57	0.71	0.57	0.29	0.89	0.60	25.59
Dp	0.58	0.86	0.43	0.27	0.92	0.51	-11.85
SIS	0.88	0.86	0.89	0.67	0.96	0.89	-70.00

Table 4:
Diagnostic performance of each MR-derived parameter to detect complete pathological response (pCR).

Abbreviations: AUC = area under ROC curve; PPV = positive predictive value; NPV = negative predictive value

from incomplete response after SCR. For IVIM DWI derived parameters the best results to discriminate responders from non-responders were obtained with Dt (sensitivity 75%, specificity 74%, AUC = 0.63, accuracy 74%, cut-off value = 25.59%). SIS obtained the best diagnostic performance also to discriminate pCR (sensitivity 86%, specificity 89%, accuracy 89%, AUC = 0.88%, cut-off value = 68.2%). A high accuracy AUC (74%) was also obtained by fp to detect pathological complete response after SCR with an area under ROC of 0.70, a sensitivity of 71%, specificity of 75%, and a cut-off value = 15.32%.

Further studies are necessary to evaluate whether combining different functional imaging techniques could increase the specificity therapy response after SCR, as already demonstrated by Lambrecht et al. [47] with the combination of ^{18}F-FDG PET/CT with pre-treatment DWI to increase the specificity of response assessment.

Some potential limitations deserve special consideration here: the MR images were evaluated based on the consensus of two radiologists in a single session for each patient so that the intra-observer variability was not assessed. A more extensive patient panel would probably strengthen the power of this study in SCR therapy assessment. A reproducibility analysis of MR-derived parameters was not performed, however the use of mean values for each DCE- and DW parameter, extracted by volume of interest, allows more robust measures to be obtained.

In conclusion, the Standardized Index of Shape is a promising DCE-MRI angiogenic biomarker for assessing preoperative treatment response after SCR with delayed surgery and it allows us to identify pathological complete response enabeling us to direct surgery in line with tailored and conservative treatment. However, parameters derived from IVIM and DKI reflect tissue response changes and could be used to assess pathological response.

Acknowledgements

Writing/editorial support in the preparation of this manuscript was provided by Manuela Di Giovanni, University of Technology, Sydney, Australia.

The statements by Siemens' customers presented here are based on results that were achieved in the customer's unique setting. Since there is no 'typical' hospital and many variables exist (e.g., hospital size, case mix, level of IT adoption), there can be no guarantee that other customers will achieve the same results.

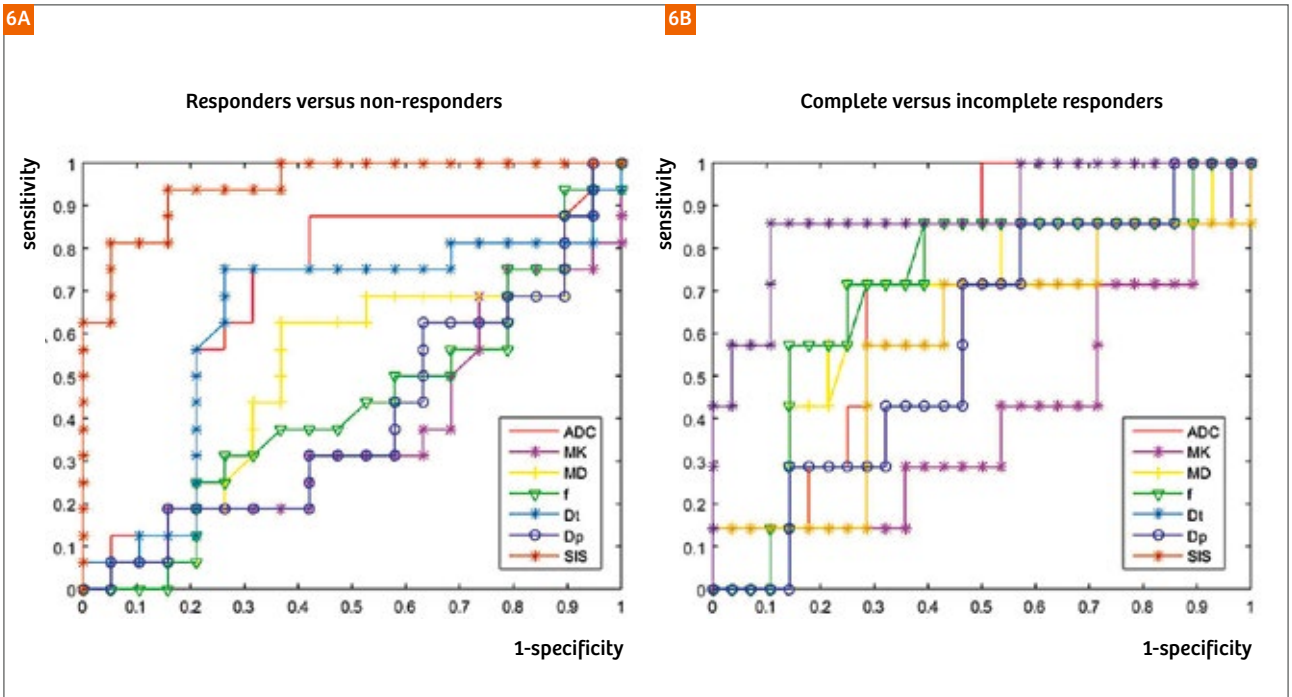

Figure 6:
ROC analysis for the best MR-derived parameters to predict pathological complete response and responder patients of SCRDS.

References

1 Avallone A, Aloj L, Delrio P, Pecori B, Leone A, Tatangelo F, Perri F, Petrillo A, Scott N, Budillon A. Multidisciplinary approach to rectal cancer: are we ready for selective treatment strategies? Anticancer Agents Med Chem. 2013 Jul 1;13(6):852-60.

2 Avallone A, Delrio P, Guida C, Tatangelo F, Petrillo A, Marone P, Cascini LG, Morrica B, Lastoria S, Parisi V, Budillon A, Comella P. Biweekly oxaliplatin,raltitrexed, 5-fluorouracil and folinic acid combination chemotherapy during preoperative radiation therapy for locally advanced rectal cancer: a phase I-II study. Br J Cancer. 2006 Jun 19;94(12):1809-15. Epub 2006 May 30.

3 Delrio P, Avallone A, Guida C, Lastoria S, Tatangelo F, Cascini GM, Marone P, Petrillo A, Budillon A, Di Marzo M, Palaia R, Albino V, De Rosa V, Parisi V. Multidisciplinary approach to locally advanced rectal cancer: results of a single institution trial. Suppl Tumori. 2005 May-Jun;4(3):8.

4 Zhou ZR, Liu SX, Zhang TS, Chen LX, Xia J, Hu ZD, Li B. Short-course preoperative radiotherapy with immediate surgery versus long-course chemoradiation with delayed surgery in the treatment of rectal cancer: a systematic review and meta-analysis. Surg Oncol. 2014 Dec;23(4):211-21.

5 Latkauskas T, Pauzas H, Gineikiene I, Janciauskiene R, Juozaityte E, Saladzinskas Z, et al. Initial results of a randomized controlled trial comparing clinical and pathological downstaging of rectal cancer after preoperative short-course radiotherapy or long-term chemoradiotherapy, both with delayed surgery. Colorectal Disease: The Official Journal of the Association of Coloproctology of Great Britain and Ireland. 2012;14(3):294–8.

6 Bujko K, Kolodziejczyk M. The 5 x 5 Gy with delayed surgery in non-resectable rectal cancer: a new treatment option. Radiotherapy and Oncology: Journal of the European Society for Therapeutic Radiology and Oncology. 2008;87(3):311–3.

7 Beppu N, Matsubara N, Noda M, Yamano T, Kakuno A, Doi H, Kamikonya N, Kimura F, Yamanaka N, Yanagi H, Tomita N. Short-course radiotherapy with delayed surgery versus conventional chemoradiotherapy: A comparison of the short- and long-term outcomes in patients with T3 rectal cancer. Surgery. 2015; 158(1):225-35.

8 Pettersson D, Holm T, Iversen H, Blomqvist L, Glimelius B, Martling A. Preoperative short-course radiotherapy with delayed surgery in primary rectal cancer. The British Journal of Surgery. 2012; 99(4):577-83.

9 Pettersson D, Lörinc E, Holm T, Iversen H, Cedermark B, Glimelius B, Martling A. Tumour regression in the randomized Stockholm III Trial of radiotherapy regimens for rectal cancer. The British Journal of Surgery. 2015; 102(8):972-8; discussion 8.

10 Radu C, Berglund A, Pahlman L, Glimelius B. Short-course preoperative radiotherapy with delayed surgery in rectal cancer – a retrospective study. Radiotherapy and Oncology: Journal of the European Society for Therapeutic Radiology and Oncology. 2008;87(3):343–9.

11 Hatfield P, Hingorani M, Radhakrishna G, Cooper R, Melcher A, Crellin A, Kwok-Williams M, Sebag-Montefiore D. Short-course radiotherapy, with elective delay prior to surgery, in patients with unresectable rectal cancer who have poor performance status or significant co-morbidity. Radiotherapy and Oncology: Journal of the European Society for Therapeutic Radiology and Oncology. 2009; 92(2):210-4.

12 Valentini V, Glimelius B, Haustermans K, Marijnen CA, Rodel C, Gambacorta MA, et al. EURECCA consensus conference highlights about rectal cancer clinical management: the radiation oncologist's expert review. Radiotherapy and Oncology: Journal of the European Society for Therapeutic Radiology and Oncology. 2014;110(1):195–8.

13 Avallone A, Piccirillo MC, Delrio P, Pecori B, Di Gennaro E, Aloj L, Tatangelo F, D'Angelo V, Granata C, Cavalcanti E, Maurea N, Maiolino P, Bianco F, Montano M, Silvestro L, Terranova Barberio M, Roca MS, Di Maio M, Marone P, Botti G, Petrillo A, Daniele G, Lastoria S, Iaffaioli VR, Romano G, Caracò C, Muto P, Gallo C, Perrone F, Budillon A. Phase 1/2 study of valproic acid and short-course radiotherapy plus capecitabine as preoperative treatment in low-moderate risk rectal cancer-V-shoRT-R3 (Valproic acid – short Radiotherapy – rectum 3rd trial). BMC Cancer. 2014 Nov 24;14:875.

14 Heo SH, Kim JW, Shin SS, Jeong YY, Kang H-K. Multimodal imaging evaluation in staging of rectal cancer. World Journal of Gastroenterology: WJG. 2014;20(15):4244-55.

15 Fusco R, Sansone M, Petrillo M, Avallone A, Delrio P, Tatangelo F, Petrillo A. Role of Magnetic Resonance Imaging in Locally Advanced Rectal Cancer, Colorectal Cancer – Surgery, Diagnostics and Treatment, Dr. Jim Khan (ed.), InTech Available from: doi 10.5772/56831.

16 Beets-Tan RG, Beets GL. Rectal cancer: review with emphasis on MR imaging. Radiology 2004;232(2):335–346.

17 Leach MO, Brindle KM, Evelhoch JL, Griffiths JR, Horsman MR, Jackson A, Jayson GC, Judson IR, Knopp MV, Maxwell RJ, McIntyre D, Padhani AR, Price P, Rathbone R, Rustin GJ, Tofts PS, Tozer GM, Vennart W, Waterton JC, Williams SR, Workman P; Pharmacodynamic/Pharmacokinetic Technologies Advisory Committee, Drug Development Office, Cancer Research UK. The assessment of antiangiogenic and antivascular therapies in early-stage clinical trials using magnetic resonance imaging: issues and recommendations. Br J Cancer 2005;92(9):1599–610.

18 Petrillo A, Fusco R, Petrillo M, Granata V, Sansone M, Avallone A, Delrio P, Pecori B, Tatangelo F, Ciliberto G. Standardized Index of Shape (SIS): a quantitative DCE-MRI parameter to discriminate responders by non-responders after neoadjuvant therapy in LARC. Eur Radiol. 2015 Jan 11.

19 Petrillo M, Fusco R, Catalano O, Sansone M, Avallone A, Delrio P, Pecori B, Tatangelo F, Petrillo A. MRI for Assessing Response to Neoadjuvant Therapy in Locally Advanced Rectal Cancer Using DCE-MR and DW-MR Data Sets: A Preliminary Report. Biomed Res Int. 2015:514740.

20 Beets-Tan RG, Beets GL. MRI for assessing and predicting response to neoadjuvant treatment in rectal cancer. Nat Rev Gastroenterol Hepatol. 2014 Aug;11(8):480-8.

21 Phongkitkarun S, Tohmad U, Larbcharoensub N, Sumbunnanondha K, Swangsilpa T, Sirachainan E. DCE-MRI-Derived Parameters as Predictors of Response to Neo-Adjuvant Chemoradiation Treatment of Rectal Carcinoma. J Med Assoc Thai. 2016 Mar;99(3):338-47.

22 Petrillo A, Fusco R, Granata V, Setola SV, Sansone M, Rega D, Delrio P, Bianco F, Romano GM, Tatangelo F, Avallone A, Pecori B. MR imaging perfusion and diffusion analysis to assess preoperative Short Course Radiotherapy response in locally advanced rectal cancer: Standardized Index of Shape by DCE-MRI and intravoxel incoherent motion-derived parameters by DW-MRI. Med Oncol. 2017 Nov 18;34(12):198.

23 Le Bihan D, Breton E, Lallemand D, Aubin ML, Vignaud J, Laval-Jeantet M. Separation of diffusion and perfusion in intravoxel incoherent motion MR imaging. Radiology. 1988 Aug;168(2):497-505.

24 Le Bihan D, Breton E, Lallemand D, Grenier P, Cabanis E, Laval-Jeantet M. MR imaging of intravoxel incoherent motions: application to diffusion and perfusion in neurologic disorders. Radiology 1986; 161(2):401-7.

25 Oto A, Yang C, Kayhan A, Tretiakova M, Antic T, Schmid-Tannwald C, Eggener S, Karczmar GS, Stadler WM. Diffusion-weighted and dynamic contrast-enhanced MRI of prostate cancer: correlation of quantitative MR parameters with Gleason score and tumor angiogenesis. AJR Am J Roentgenol. 2011 Dec;197(6):1382-90.

26 Curvo-Semedo L, Lambregts DM, Maas M, Thywissen T, Mehsen RT, Lammering G, Beets GL, Caseiro-Alves F, Beets-Tan RG. Rectal cancer: assessment of complete response to preoperative combined radiation therapy with chemotherapy – conventional MR volumetry versus diffusion-weighted MR imaging. Radiology. 2011 Sep;260(3):734-43.

27 A, Deux J-F, Brugieres P, Rahmouni A. Liver cirrhosis: intravoxel

incoherent motion MR imaging-pilot study. Radiology 2008; 249(3): 891-9.
28 Wirestam R, Borg M, Brockstedt S, Lindgren A, Holtas S, Stahlberg F. Perfusion-related parameters in intravoxel incoherent motion MR imaging compared with CBV and CBF measured by dynamic susceptibility contrast MR technique. Acta Radiol. 2001; 42(2): 123-8.
29 Granata V, Fusco R, Catalano O, Guarino B, Granata F, Tatangelo F, Avallone A, Piccirillo M, Palaia R, Izzo F, Petrillo A. Intravoxel incoherent motion (IVIM) in diffusion-weighted imaging (DWI) for Hepatocellular carcinoma: correlation with histologic grade. Oncotarget. 2016 Nov 29;7(48):79357-64.
30 Granata V, Fusco R, Catalano O, Filice S, Amato DM, Nasti G, Avallone A, Izzo F, Petrillo A. Early Assessment of Colorectal Cancer Patients with Liver Metastases Treated with Antiangiogenic Drugs: The Role of Intravoxel Incoherent Motion in Diffusion-Weighted Imaging. PLoS One. 2015 Nov 13;10(11):e0142876.
31 Koh DM, Collins DJ, Orton MR. Intravoxel incoherent motion in body diffusion-weighted MRI: reality and challenges. AJR Am J Roentgenol 2011; 196(6): 1351–1361.
32 Jensen JH, Helpern JA. MRI quantification of non-Gaussian water diffusion by kurtosis analysis. NMR Biomed. 2010; 23:698–710.
33 Dresen RC, Beets GL, Rutten HJ, Engelen SM, Lahaye MJ, Vliegen RF, de Bruïne AP, Kessels AG, Lammering G, Beets-Tan RG. Locally advanced rectal cancer: MR imaging for restaging after neoadjuvant radiation therapy with concomitant chemotherapy. Part I. Are we able to predict tumor confined to the rectal wall? Radiology 2009;252(1):81-91.
34 SIS Tool by Antonella Petrillo available on request at an.petrillo@istitutotumori.na.it
35 Fusco R, Petrillo A, Petrillo M, Sansone M. Use of Tracer Kinetic Models for Selection of Semi-Quantitative Features for DCE-MRI Data Classification. Applied Magnetic Resonance. 2013;44(11):1311-24.
36 Andreola S, Leo E, Belli F, Bonfanti G, Sirizzotti G, Greco P, Valvo F, Tomasic G, Gallino GF. Adenocarcinoma of the lower third of the rectum surgically treated with a < 10-mm distal clearance: preliminary results in 35 N0 patients. Ann Surg Oncol 2001;8(7):611–615.
37 Mandard AM, Dalibard F, Mandard JC, Marnay J, Henry-Amar M, Petiot JF, Roussel A, Jacob JH, Segol P, Samama G, et al. Pathologic assessment of tumor regression after preoperative chemoradiotherapy of esophageal carcinoma. Clinicopathologic correlations. Cancer. 1994 Jun 1;73(11):2680-6.
38 Choi MH, Oh SN, Rha SE, Choi JI, Lee SH, Jang HS, Kim JG, Grimm R, Son Y. Diffusion-weighted imaging: Apparent diffusion coefficient histogram analysis for detecting pathologic complete response to chemoradiotherapy in locally advanced rectal cancer. J Magn Reson Imaging. 2015 Dec 15. Available from: doi: 10.1002/jmri.25117.
39 Doi H, Beppu N, Kato T, Noda M, Yanagi H, Tomita N, Kamikonya N, Hirota S. Diffusion-weighted magnetic resonance imaging for prediction of tumor response to neoadjuvant chemoradiotherapy using irinotecan plus S-1 for rectal cancer. Mol Clin Oncol. 2015 Sep;3(5):1129-34.
40 Nougaret S, Vargas HA, Lakhman Y, Sudre R, Do RK, Bibeau F, Azria D, Assenat E, Molinari N, Pierredon MA, Rouanet P, Guiu B. Intravoxel Incoherent Motion-derived Histogram Metrics for Assessment of Response after Combined Chemotherapy and Radiation Therapy in Rectal Cancer: Initial Experience and Comparison between Single-Section and Volumetric Analyses. Radiology. 2016 Aug;280(2):446-54.
41 Petrillo A, Fusco R, Petrillo M, Granata V, Delrio P, Bianco F, Pecori B, Botti G, Tatangelo F, Caracò C, Aloj L, Avallone A, Lastoria S. Standardized Index of Shape (DCE-MRI) and Standardized Uptake Value (PET/CT): Two quantitative approaches to discriminate chemo-radiotherapy locally advanced rectal cancer responders under a functional profile. Oncotarget. 2017 Jan 31;8(5):8143-53.
42 Iima M, Le Bihan D. Clinical Intravoxel Incoherent Motion and Diffusion MR Imaging: Past, Present, and Future. Radiology. 2016 Jan;278(1):13-32.
43 Rega D, Pecori B, Scala D, Avallone A, Pace U, Petrillo A, Aloj L, Tatangelo F, Delrio P. Evaluation of Tumor Response after Short-Course Radiotherapy and Delayed Surgery for Rectal Cancer. PLoS One. 2016 Aug 22;11(8):e0160732.
44 Pecori B, Lastoria S, Caracò C, Celentani M, Tatangelo F, Avallone A, Rega D, De Palma G, Mormile M, Budillon A, Muto P, Bianco F, Aloj L, Petrillo A, Delrio P. Sequential PET/CT with [18F]-FDG Predicts Pathological Tumor Response to Preoperative Short Course Radiotherapy with Delayed Surgery in Patients with Locally Advanced Rectal Cancer Using Logistic Regression Analysis. PLoS One. 2017 Jan 6;12(1):e0169462.
45 Siegel R, Dresel S, Koswig S, Gebauer B, Hunerbein M, Schneider W, Schlag PM. Response to preoperative short-course radiotherapy in locally advanced rectal cancer: value of f-fluorodeoxyglucose positron emission tomography. Onkologie. 2008; 31(4):166-72.
46 Janssen MH, Ollers MC, van Stiphout RG, Buijsen J, van den Bogaard J, de Ruysscher D, Lambin P, Lammering G. Evaluation of early metabolic responses in rectal cancer during combined radiochemotherapy or radiotherapy alone: sequential FDG-PET-CT findings. Radiotherapy and Oncology: Journal of the European Society for Therapeutic Radiology and Oncology. 2010; 94(2):151-5.
47 Lambrecht M, Deroose C, Roels S, Vandecaveye V, Penninckx F, Sagaert X, van Cutsem E, de Keyzer F, Haustermans K. The use of FDG-PET/CT and diffusion weighted magnetic resonance imaging for response prediction before, during and after preoperative chemoradiotherapy for rectal cancer. Acta Oncol 2010;49:956–63.

Contact Roberta Fusco
Division of Radiology, Department of Diagnostic Imaging, Radiant and Metabolic Therapy,
Istituto Nazionale Tumori (IRCCS) Fondazione G. Pascale

Via Mariano Semmola 80131
Naples
Italy
Phone: 00390815903738
Fax: 00390815903825
r.fusco@istitutotumori.na.it

Machine-specific MRI quality control procedures for stereotactic radiosurgery treatment planning

Ali Fatemi, Ph.D.[1,2]; Somayeh Taghizadeh, M.S.[1,2]; Claus Chunli Yang, Ph.D.[1]; Madhava R. Kanakamedala, M.D.[1]; Srinivasan Vijayakumar, M.D.[1]; Roberto Rey-Dios, M.D.[1,3]; Bart Morris, M.S.[1]; William N. Duggar, M.S.[1]; Edward Florez, Ph.D.[2]

[1] Department of Radiation Oncology, University of Mississippi Medical Center, Jackson, MS, USA
[2] Department of Radiology, University of Mississippi Medical Center, Jackson, MS, USA
[3] Department of Neurosurgery, University of Mississippi Medical Center, Jackson, MS, USA

Abstract

Purpose
MR images are necessary for accurate contouring of intracranial targets, determination of gross target volume (GTV) and evaluation of organs at risk (OAR) during stereotactic radiosurgery (SRS) treatment planning procedures. Many centers use MRI simulators or regular diagnostic MRI machines for SRS treatment planning; while both types of machine require two stages of quality control (QC), both machine- and patient-specific, before use for SRS, no accepted guidelines for such QC currently exist. This article describes appropriate machine-specific QC procedures for SRS applications.

Methods and materials
We describe adaptation of American College of Radiology (ACR)-recommended QC tests using an ACR MRI phantom for SRS treatment planning. In addition, commercial Quasar MRID^{3D} and Quasar GRID^{3D} phantoms (Modus Medical, London, ON, Canada) were used to evaluate the effects of B_0 inhomogeneity, gradient nonlinearity, and a Leksell G frame (SRS frame) and its accessories on geometrical distortion in MR images.

Results
QC procedures found maximal in-plane distortions of 3.5 mm and 2.5 mm in the x and y directions, respectively, and < 1 mm distortion at a head-sized region of interest. MR images acquired using a Leksell G frame and localization devices showed a mean absolute deviation of 2.3 mm from isocenter. The results of modified ACR tests were all within recommended limits and baseline measurements have been defined for regular weekly QC tests.

Conclusions
With appropriate QC procedures in place, it is possible to obtain clinically useful MR image SRS treatment plans on a regular basis. MRI examination for SRS planning can benefit from the improved localization and planning possible with the superior image quality and soft tissue contrast achieved under optimal conditions.

Sequence/contrast	Parameters	Disease
Axial T1-weighted MPRAGE	1 x 1 x 1 mm^3, TR/TE = 2200/2.91 ms, 300 Hz/pixel	Brain metastasis, pituitary/parasellar lesions, acoustic neuroma/schwannoma, trigeminal neuralgia, AVM
Axial T2-weighted SPACE	0.9 x 0.9 x 1 mm^3, TR/TE = 1400/184 ms, 345 Hz/pixel	Pituitary/parasellar lesions, acoustic neuroma/schwannoma, AVM
Axial T2-weighted CISS	0.9 x 0.9 x 1 mm^3, TR/TE = 5.48/2.38 ms, 340 Hz/pixel	Pituitary/parasellar lesions, acoustic neuroma/schwannoma, trigeminal neuralgia

Table 1:
Approved MRI pulse sequences for SRS treatment planning.

Abbreviations: MPRAGE = magnetization-prepared 180-degree radio-frequency pulses and rapid gradient-echo; SPACE = sampling perfection with application optimized contrasts using different flip angle evolution; CISS = Three-dimensional (3D) constructive interference in steady state; TR = Time of Repetition; TE = Time of Echo

Introduction

Using MR images for stereotactic radiosurgery (SRS) treatment planning requires careful consideration of a number of factors [1], including choice of the correct MRI pulse sequences (3D, no slice gap, less geometrical distortion, high signal-to-noise ratio (SNR) and isotropic spatial resolution), immobilization devices (MRI-compatible SRS frame), customized RF coils (proper sensitivity, low RF deposition, consequently less contour deformation) such as a single channel send-and-receive RF head coil (Rx/Tx RF head coil), and most importantly, confirmation that the MRI images acquired possess high geometrical accuracy and stability.

Existing MR quality control (QC) procedures [2–6] are inadequate for assessing MRI scanners for SRS treatment-planning purposes, primarily because existing tests have been developed for machines used in general diagnostic radiology. There, the goal is to maintain image quality rather than spatial fidelity and signal intensity [7]. Several well-established references from the American College of Radiology (ACR) [2, 3] and the American Association of Physicists in Medicine (AAPM) [4–6] provide guidance regarding QC procedures for MRI scanners used in diagnostic radiology, but no guidance documents currently describe the unique QC factors that must be considered when using MRI scanners in SRS treatment planning [7–9]. However, existing quality

Daily QA (MRI technologists) using ACR phantom	Monthly QA (Therapy physicist/MRI physicist) using MRID^{3D}, GRID^{3D}, and ACR phantoms	Annual QA (MRI physicist) using MRID^{3D}, GRID^{3D}, and ACR phantoms
Inspect bore for loose metal (bobby pins, earrings, etc.)	Patient safety (monitors, intercom, panic ball, emergency buttons, and signage)	20-channel RF coil integrity check
Tx/Rx and 20-channel RF coil SRS check using uniform phantom	Patient comfort (bore light and fan)	B_0 constancy
Patient safety (intercom, panic ball, detector)	Percent signal ghosting	B_{1+} constancy
Geometry accuracy and B_0 check using ACR phantom	Percent image uniformity	Gradient linearity constancy
	High/low contrast accuracy	Slice thickness accuracy
Weekly QA (MRI technologists) using ACR phantom	Coach position accuracy	Slice position accuracy
Transmitter gain constancy	Image artifact	Geometrical accuracy
Center frequency constancy	Geometrical accuracy (large field-of-view)	Rx/Tx RF head coil check
20-channel RF head coil SNR	Geometrical accuracy (small field-of-view) with and without frame	20-channel RF head coil check
Rx/Tx RF head coil SNR		Dynamic field map
Slice thickness accuracy		Eddy current compensation
Slice position accuracy		Gradient delay
Geometric accuracy and B_0 check using ACR phantom		Gradient sensitivity
		Body coil image brightness
		Magnet shim
		Rx gain calibration
		Body coil tuning
		Spike
		PMU transmit
		Rx stability
		Tx stability

Table 2 :
QC tests and frequencies for MRI guided Stereotactic Radiosurgery (SRS).

Abbreviations: Tx/Rx RF coil = single channel send/receive radio-frequency coil; PMU = Phasor Measurement Unit

Test	MRI machine tolerance
MRI geometrical distortion	
Evaluate distortion vector, combined effect (B_0 inhomogeneity and gradient nonlinearity) over large field-of-view (37 cm)	< 1 mm over 20 cm DSV and < 2 mm over 37 cm DSV
Evaluate B_0 inhomogeneity over large field-of-view (37 cm)	2 ppm
Evaluate the geometrical distortion vector with stereotactic frame (small field-of-view, 20 cm)	< 1 mm
Adapted ACR QC tests	
Setup and table position accuracy	< 1 mm
Center frequency	Pass/Fail
Signal ghosting	≤ 2.5%
Transmitter gain or attenuation	Pass/Fail
High contrast spatial resolution	Row and column resolution ≤ 1 mm
Low contrast detectability	9 rows total for up to 1.5T
Magnetic field homogeneity	Action limit ± 2 ppm
Artifact evaluation	Pass/Fail
Magnetic field homogeneity	Action limit ± 2 ppm
Geometrical accuracy	Within < 1.5 mm of actual length
Visual checklist	Pass/Fail
Slice position accuracy	Difference from actual position ≤ 3 mm
Slice thickness accuracy	Action limit is 5 ± 0.7 mm
20-channel RF head coil evaluation	Signal-to-noise ratio (SNR) PIU ≥ 87.5% (< 3T) Percentage Signal Ghosting (PSG) ≤ 2.5%
Rx/Tx RF head coil evaluation	Signal-to-noise ratio (SNR) PIU ≥ 87.5% (< 3T) Percentage Signal Ghosting (PSG) ≤ 2.5%
Rx/Tx RF head coil check	Pass/Fail
20-channel RF head coil check	Pass/Fail
Dynamic field map	Pass/Fail
Eddy current compensation	Pass/Fail
Gradient delay	Pass/Fail
Gradient sensitivity	Pass/Fail
Body coil image brightness	Pass/Fail
Magnet shim	Pass/Fail
RX gain calibration	Pass/Fail
Body coil tuning	Pass/Fail
Spike	Pass/Fail
PMU transmit	Pass/Fail
Rx stability	Pass/Fail
Tx stability	Pass/Fail
Assessment of MRI safety program	**Pass/Fail**

Table 3 :
Summary of MRI acceptance QC tests for SRS treatment planning.

Abbreviations: DSV = Diameter Spherical Volume; PIU = Percentage Image Uniformity

control tests can be modified to provide the necessary information for a given SRS-planning application by testing over appropriate volumes and using SRS-specific MR imaging parameters.

Development of our QC process started with evaluation of gross machine factors, including B_0 inhomogeneity and gradient non-linearity, over a large field-of-view using the scanner body coil, then narrowed to study the effects on geometrical stability of MR images due to use of an MRI-compatible SRS frame and its localizer using a Tx/Rx RF head coil [10]. Finally, adapted ACR tests were performed to evaluate the image contrast, spatial resolution, gradient stability for accurate slice selection and thickness, RF coil sensitivity, and acquisition of artifact-free MR images. Testing these factors ensures that acquired images possess the quality and resolution required for precision SRS treatment planning, accurately identifying disease extent and proximity relative to adjacent organs at risk (OAR) [1].

We are establishing a quality assurance (QA) program to continuously and systematically evaluate MRI scanner performance, safety and stability for SRS treatment planning. Our goal in this article is to describe our QC tests and strategy in establishing a QA program for MRI-guided SRS treatment planning. This paper focuses narrowly on MRI machine-specific aspects of the QC procedure and leaves patient-specific QC tests, including patient-specific geometrical distortion evaluation, correction methods, customized RF coils, patient comfort, MRI safety, and MRI pulse sequence optimization, for future reports.

Method and materials

We recently installed a Leksell Gamma Knife® Icon™ SRS treatment unit[1] (Elekta AB, Stockholm, Sweden) and a 1.5T MAGNETOM Aera RT Pro edition (Siemens Healthcare, Erlangen, Germany) MRI machine at our institute. The SRS committee consists of three physicists, a radiologist, a radiation oncologist, and a neurosurgeon, who work together to develop guidelines for MRI-guided SRS treatment planning. MR images are used to assess cases of brain metastasis, pituitary/parasellar lesions, acoustic neuroma, trigeminal neuralgia, and arteriovenous malformation (AVM).

The MRI SRS QC procedure has been developed based on factors including imaging site, MRI pulse sequence(s), adapted or standard RF coils, and any immobilization devices required. SRS patients are scanned on a regular diagnostic MRI table, using a Leksell G frame with immobilization and localization devices, or frameless, as appropriate. In our institute, we use a Tx/Rx CP head coil (Siemens Healthcare, Erlangen, Germany) to fit the Leksell G frame, plus an MRI indicator box with an adaptor to the coil, and are still able to keep the specific absorption rate (SAR) under 3 W/kg. The downside of using such an RF coil is a less-than-ideal SNR and long scanning time; thus, we use a regular 20-channel RF head coil for frameless cases. MRI pulse sequences have been evaluated by the SRS committee based on disease site and treatment planning criteria detailed in Table 1.

We summarize the commissioning and quality control (QC) tests (test, frequency, and machine tolerance) in Tables 2 and 3.

1. Evaluation of geometrical distortion over a large field-of-view

We used a QUASAR™ MRID^{3D} (Modus Medical, London, ON, Canada) geometrical distortion phantom (Fig. 1) to measure B_0 inhomogeneity and gradient non-linearity using a reverse gradient technique over a 37 x 32 cm (W x L) phantom area. The phantom was scanned with a 3D VIBE T1-weighted sequence: 1 mm^3 isotropic voxels, NEX of 2, TE of 4 ms, TR of 9 ms, a flip angle ~10°, and a bandwidth of 120 Hz/pixel. QUASAR™ MRID^{3D} comes with easy-to-use image analysis software for calculation of the phantom boundary distortion vector field, volumetric 3D distortion vector field, and B_0 distortion vs. gradient distortion, using 3D spherical harmonic analysis.

[1] The information shown herein refers to products of 3rd party manufacturer's and thus are in their regulatory responsibility. Please contact the 3rd party manufacturer for further information.

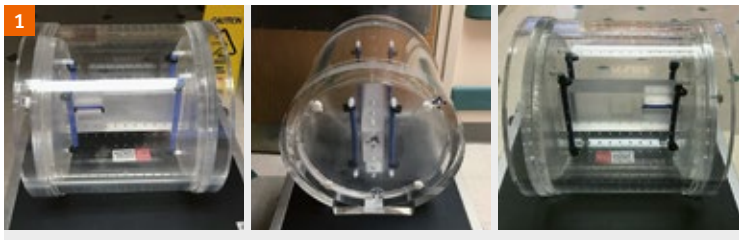

Figure 1:
Quasar MRID^{3D} geometrical distortion phantom

Figure 2:
(2A) Quasar GRID^{3D} image distortion phantom
(2B) Standard ACR

2. Evaluation of the effect of an SRS frame and localizer on geometrical stability of MR images

We used a QUASAR™ GRID^{3D} Image Distortion Phantom and analysis system (Modus Medical, London, ON, Canada) to evaluate MR image distortion due to the introduction of an SRS frame and localizers. The system is comprised of a phantom and analysis software which work together to produce a 3D map of spatial distortion with submillimeter accuracy throughout a volume of interest. The phantom (Fig. 2A) is an acrylic cube containing a 1-cm 3D grid of channels filled with copper sulfate solution. The region of interest is a 14 x 13 x 11 cm^3 volume containing 2002 vertex locations, the positions of which are known to within 0.1 mm.

The phantom accurately and reproducibly mounts securely to the SRS Leksell Frame G at a known position. It fits within both the Leksell® MR Indicator and Leksell® CT Indicator. We scanned our phantom using a 3D MPRAGE pulse sequence: T1-weighted, 1 x 1 x 1 mm^3, TR/TE of 2200/3.74 ms, and 350 Hz/pixel. The MPRAGE is the only MRI pulse sequence being used for treatment planning and the rest of the sequences will be registered rigidly.

3. ACR MRI tests adapted for SRS treatment planning

We used a standard MRI ACR phantom (Fig. 2B) to evaluate the rest of our adapted QC MRI tests. The ACR phantom has been scanned based on MRI pulse sequences and parameters summarized in Table 4. All QC tests with their tolerances are summarized in Table 2.

Protocol	Phantom used	TR (ms)	TE (ms)	FOV (mm)	# Slices	Slice thickness (mm)	GAP	NEX	Matrix	BW
ACR T1 Localizer	ACR	200	20	25	1	20	N/A	1	256 x 256	Routine (15.6 kHz)
ACR T1 Axial	ACR	500	20	25	11	5	5	1	256 x 256	Routine (15.6 kHz)
ACR T2 Axial	ACR	2000	20/80	25	11	5	5	1	256 x 256	Routine (15.6 kHz)
Site T1 Axial	ACR	Site protocol	Site protocol	25	11	5	5	Site protocol	256 x 256	Site protocol BW
Site T2 Axial	ACR	Site protocol	Site protocol	25	11	5	5	Site protocol	256 x 256	Site protocol BW
Low BW Axial[1]	ACR	500	20	25	1	5	N/A	1	256 x 256	Minimum BW @ 256 x 256 matrix
Low BW Coronal[1]	ACR	500	20	25	1	5	N/A	1	256 x 256	Minimum BW @ 256 x 256 matrix
Low BW Sagittal[1]	ACR	500	20	25	1	5	N/A	1	256 x 256	Minimum BW @ 256 x 256 matrix
High BW Axial[1]	ACR	500	20	25	1	5	N/A	1	256 x 256	Minimum BW @ 256 x 256 matrix
High BW Coronal[1]	ACR	500	20	25	1	5	N/A	1	256 x 256	Minimum BW @ 256 x 256 matrix
High BW Sagittal[1]	ACR	500	20	25	1	5	N/A	1	256 x 256	Minimum BW @ 256 x 256 matrix

Table 4 :
MRI pulse sequences and parameters for adapted MRI ACR QC tests.

Abbreviations: BW = Bandwidth

[1] Acquired three separate series, each consisting of a single image through the center of phantom with minimum and highest bandwidths.

4. Evaluating MRI safety

As part of our acceptance tests we used a gauss meter to carefully map and post the 5-gauss line with proper signage. We monitor all patients through both a questionnaire and in-person consultation to make sure that any person with a cardiac pacemaker or neurosimulators does not cross the 5-gauss line. Our MRI room is also equipped with a Ferroguard® (Metrasens Ltd., Lemont, IL, USA) wall mounted system deployed in an entryway mode on both sides of the doorway. This system provides real-time monitoring of the local ferromagnetic environment with an audible alert system. We also check the patient/console intercom system, table-top button (magnet housing and console), emergency stop buttons, emergency rundown unit, and door switches on a regular basis.

5. Establishing MRI quality assurance program

We summarize our proposed QC tests and their frequencies in Table 2. What follows is a formulaic approach to monitor B_0 inhomogeneity and geometrical distortion with weekly and daily QC tests using an ACR phantom. We found that incorporating these tests into recommended weekly ACR tests run by a technologist and using only an MRI ACR phantom makes the process faster and more efficient in our busy clinic.

First, we defined our reference B_0 inhomogeneity and geometrical distortion during monthly and commissioning processes using Quasar MRID^{3D}. The MRI image geometrical distortion and machine B_0 inhomogeneity were defined over a 37 x 32 cm (W x L) area on three dimensions (Δx, Δy, Δz) and absolute value from MRI isocenter. Next, we scanned the regular ACR MRI phantom and defined B_0 inhomogeneity using a bandwidth difference technique, and defined geometrical distortion using sagittal slices 1 and 5 for all three dimensions. We used geometrical distortion measurements for slice 5 (Δx, Δy) and the sagittal plane (Δz) for baseline calculation, assuming that slice 5 is at or very close to the MRI isocenter. Finally, the average baseline was defined based on equation 1 and 2 for the same slices and diameter on both MRID^{3D} and ACR phantoms. The baseline measure is used for weekly checks, and we define our tolerance as 2% changes, and action level as a measured 4% difference.

Equation 1:

$$Base_{B0} = ACR_{B0} - MRID^{3D}{}_{B0}$$

$Base_{B0}$ is an averaged B_0 inhomogeneity at the same slice at MRID^{3D} and ACR phantoms; $MRID^{3D}{}_{B0}$ is the measured average B_0 inhomogeneity in ppm; and ACR_{B0} is averaged B_0 inhomogeneity in (ppm) using the bandwidth difference technique, and

Equation 2:

$$Base_{geometrical\ distortion} = ACR_{geometrical\ distortion} - MRID^{3D}{}_{geometrical\ distortion}$$

Where $Base_{geometrical\ distortion}$ is the geometrical distortion at the slice and orientation at MRID^{3D} and ACR phantoms; $ACR_{geometrical\ distortion}$ is the measured geometrical distortion at slice 5 and sagittal plane on all three directions (Δx, Δy, Δz); and $MRID^{3D}{}_{geometrical\ distortion}$ is the measured geometrical distortion at the same ACR slice and orientation.

Results

The geometrical distortion over a 37 x 32 cm (W x L) area was evaluated in all three dimensions (Δx, Δy, Δz), absolute distance from MRI isocenter. Table 5 contains summary statistics; the maximum distortion in the x and y plane (axial plane) was 3.5 mm and 2.5 mm at the boundaries.

The detailed measurements along all three coordinates and their absolute values with respect to MRI isocenter is shown in Figure 3. The B_0 inhomogeneity along the z direction was measured separately using an inverse gradient technique, and those data are also shown in Figure 3.

We used a QUASAR™ GRID^{3D} Image Distortion Phantom and analysis system to evaluate image distortion in MR images due to the presence of an SRS frame and localizers. The data in the axial plane of the MR images showed a maximum of 0.5 mm in the x-direction, 1.5 mm in the y-direction; in the z-direction the maximum of 2.6 mm was observed at the phantom boundary (11 cm from MRI isocenter). The results showed a mean absolute deviation of 2.3 mm from isocenter. We defined our ACR phantom weekly B_0 inhomogeneity and geometrical distortion baselines: the reference B_0 inhomogeneity using MRID^{3D} phantom was evaluated on all three axes (axial: 1.89 ppm, coronal: 0.135 ppm and sagittal: 0.068 ppm) as well as on average (0.699 ppm), all well-defined within our limits of ± 2 ppm. The $Base_{B0\ inhomogeneity}$ based on Equation 1 was defined as 0.03 ppm.
The $Base_{geometrical\ distortion}$ was defined for our MRI ACR phantom at slice 5 as 0.6 mm in the x-direction, 0.8 mm in the y-direction, and 0.5 mm in the sagittal plane.

Continued on page 92.

	Mean (mm)	STD (mm)	Max (mm)	> 2.5 mm (%)
dx	0.91	0.67	3.5	3
dy	0.52	0.39	2.51	0
dz	2.38	2.45	13.1	34
dr	2.79	2.36	13.19	40

Table 5 :
Summary statistical of MRID[3D] geometrical distortion measurements.

Abbreviations: STD = Standard Deviation

3

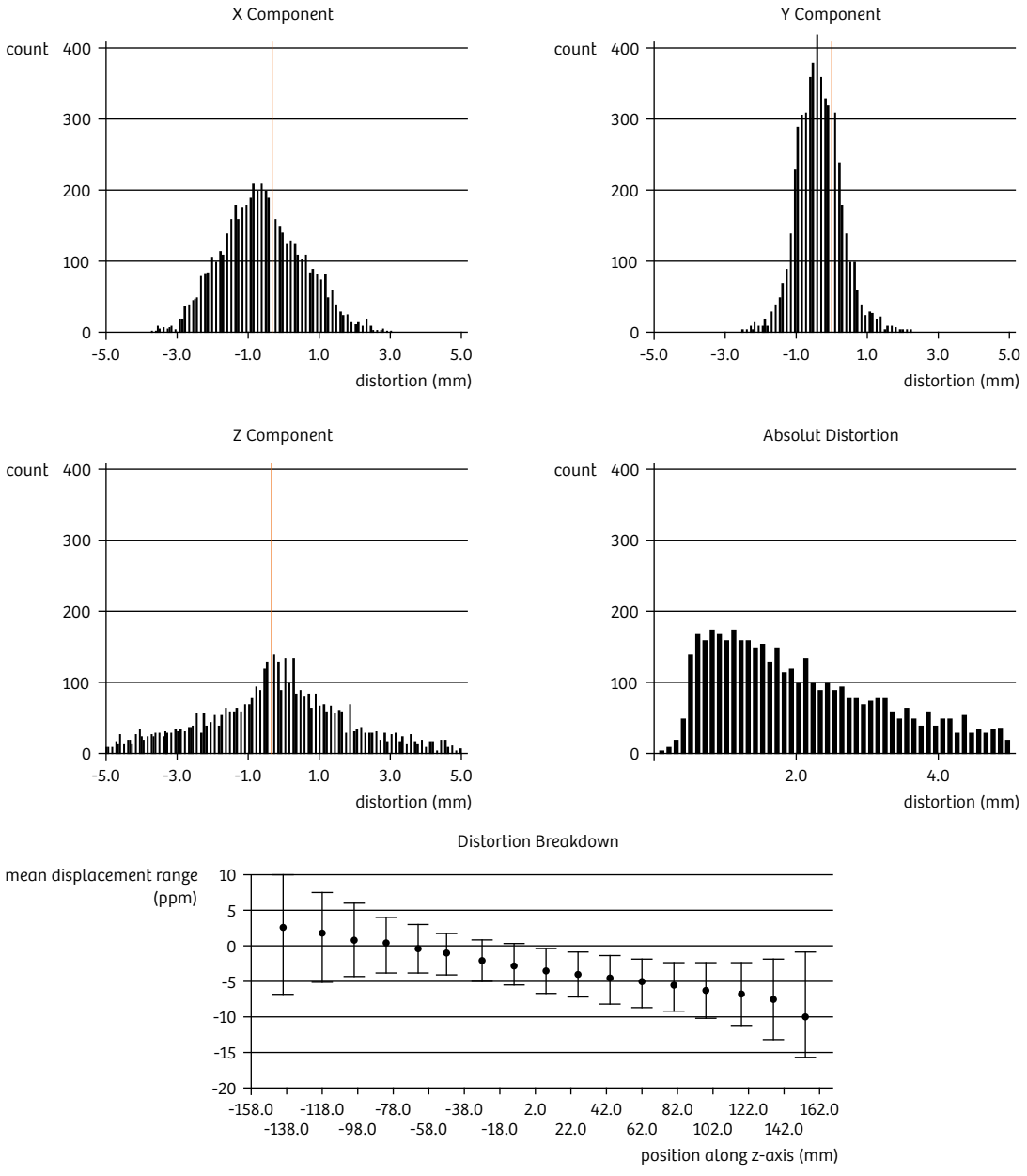

Figure 3:
B_0 inhomogeneity and distortion measurement results using an MRID[3D] phantom.

MRI equipment evaluation summary		
1.	Setup and table position accuracy	Pass
2.	Center frequency	Pass
3.	Transmitter gain or attenuation	Pass
4.	Geometric accuracy measurements	Pass
5.	High-contrast spatial resolution	Pass
6.	Low-contrast detectability	Pass
7.	Artifact evaluation	Pass
8.	Visual checklist	Pass
9.	Magnetic field homogeneity	Pass
	Method of testing	BW diff
10.	Slice-position accuracy	Pass
11.	Slice-thickness accuracy	Pass
12.	Radiofrequency coil checks (20-channel RF head coil)	
	a. SNR	Pass
	b. Volume coil percent image uniformity	Pass
	c. Percent signal ghosting	Pass
13.	Radiofrequency coil checks (Rx/Tx RF head coil)	
	a. SNR	Pass
	b. Volume coil percent image uniformity (PIU)	Pass
	c. Percent signal ghosting	Pass
14.	Rx/Tx RF head coil check	Pass
15.	20-channel RF head coil check	Pass
16.	Dynamic field map	Pass
17.	Eddy current compensation	Pass
18.	Gradient delay	Pass
19.	Gradient sensitivity	Pass
20.	Body coil image brightness	Pass
21.	Magnet shim	Pass
22.	RX gain calibration	Pass
23.	Body coil tuning	Pass
24.	Spike	Pass
25.	PMU transmit	Pass
26.	Rx stability	Pass
27.	Tx stability	Pass

Table 6 :
MRI SRS QC results.

Abbreviations: PMU = Phasor Measurement Unit

All adopted ACR measures were within our defined tolerance, as summarized in Table 6. Specifically, the 20-channel and Rx/Tx RF head coils have been tested thoroughly for SNR, PIU and PSG, and the results were found to fall within our accepted limits.

Discussion

The methodology discussed herein describes practical strategies we have implemented through lessons learned performing clinical MRI QA and SRS treatment planning [11–14]. We focus on discussion of major issues encountered during our QC procedures.

The MRI machine specifications which have the greatest potential to affect SRS treatment planning are B_0 and B_1 inhomogeneity and gradient non-linearity, which affect the geometrical accuracy and intensity uniformity of MR images. Use of single channel Rx/Tx RF head coils, a Leksell G frame (SRS frame) and accessories for SRS treatment planning only exacerbates these issues. Using an MRID^{3D} phantom over a 37 x 32 cm (W x L) area gives enough information about MR image distortion due to B_0 inhomogeneity and gradient non-linearity to allow acquired images to be used for SRS treatment planning. As we expected, geometrical distortion is within 1 mm accuracy in the axial plane (x and y directions), and 2 mm along the z direction 10 cm from isocenter (almost head size), but it worsens to the order of 5 mm at the boundaries (16 cm away from isocenter).

Immobilization devices constructed from materials optimized for radiation therapy may not necessarily be optimal for MRI (e.g. carbon fiber) [15–17]. In our experience, it is no longer sufficient for immobilization device materials (Leksell G frame, screws, adaptor, and MRI localizer) to be simply MRI-compatible; these materials and devices should be MRI-optimal. Poor material choices can contribute to magnetic susceptibility induced geometric distortions. Our phantom results specifically on 3D axial T2 SPACE and axial T2 CISS sequences show artifacts even after pulse sequence optimization and use of different orientations. It is essential that some MRI sequences reviewed by the SRS team be repeated using a different sequence, such as 2D axial T2 or T1-weighted Turbo Spin Echo (TSE). However, our results from Quasar™ GRID^{3D} shows that images acceptable for treatment planning can be obtained with the use of Laksell frame and localization devices by using the right MRI pulse sequence and a Tx/Rx RF head coil.

Our proposed SRS MRI QA program has been reviewed and approved by our QA committee, and peer reviewed at every step by SRS committee members. Our aim is to minimize the scanning time and maximize efficiency.

One major change proposed was use of the MRI ACR phantom for weekly geometrical accuracy checks rather than the MRID^{3D}. This streamlines the process and the technologist can incorporate these results into the regular weekly checks.

Our results indicated that gradient nonlinearity-induced geometric distortions can be severe and must be corrected using 3D distortion correction prior to using MR images for SRS treatment planning. However, even with 3D distortion correction, residual distortions can persist for large FOV prescriptions. One compounding factor is that some MRI scanners permit acquisition of image volumes positioned off-center from isocenter in the superior/inferior direction. This approach increases the likelihood of scanning in regions of nonlinear gradients and, therefore, increases the likelihood of residual distortions. At a minimum, the magnitude of these residual distortions should be characterized as a function of radial distance from isocenter for each scanner. Ideally, the residual distortions would be corrected.

High MR image intensity uniformity is critical in SRS treatment planning. Phased-array RF coils require correction for differences in the sensitivity profiles of each coil element during reconstruction to optimize image uniformity. These corrections, often based on a quick prescan image, become increasingly important when flexible phased-array RF coils, wrapped around the patient in various positions, are utilized. Our results indicate that by using prescan normalization and postprocessing corrections the MR images collected are within preset limits and SNR, PIU and PSG tests serve as good indications for variation.

The participation of the dedicated SRS team, including the medical physicist, radiation oncologist, and neuro-surgeon in the quantification, protocol modification and development of quality assurance procedures, as well as verification of MRI data used for SRS planning, is critical. Moreover, the scanner selection considerations, specifications, chosen MRI pulse sequences, and post processing packages are extremely important in having a successful program of MRI-guided SRS treatment planning.

Conclusions

In conclusion, we describe an MRI machine QC procedure to maintain clinically acceptable MR image acquisition for SRS treatment planning purposes. MRI examinations for SRS planning can benefit from the improved localization and planning possible with the superior image quality and soft tissue contrast achieved with appropriate MRI QA. We recommend convening a team of experts who meet periodically to review cases, discuss new MRI pulse

sequences and technology, including newly available post-processing software packages, and who can develop a custom QA program for the facility. We strongly believe this type of dialog opens opportunities for greater use of MRI images in SRS treatment planning, especially in a new era of MRI-guided radiotherapy available in commercial machines.

Acknowledgments

The authors would like to thank Brain Barker and especially all members of the MRI service crew for fruitful discussions.

References

1 P. M. Evans, Anatomical imaging for radiotherapy, Phys. Med. Biol. 2008, 53, R151–R191.
2 American College of Radiology (ACR). Magnetic resonance imaging quality control manual. 2015.
3 American College of Radiology (ACR). MR accreditation program phantom test guidance. 2005.
4 American Association of Physicists in Medicine (AAPM). AAPM Report 28: Quality assurance methods and phantoms for magnetic resonance imaging. 1990.
5 American Association of Physicists in Medicine (AAPM). AAPM Report 34: Acceptance testing of magnetic resonance imaging systems. 1992.
6 American Association of Physicists in Medicine (AAPM). AAPM Report 100: Acceptance testing and quality assurance procedures for magnetic resonance imaging facilities. 2010.
7 V. S. Khoo and D. L. Joon, New developments in MRI for target volume delineation in radiotherapy, Br. J. Radiol. 2006,79, S2–S15.
8 P. Metcalfe, G. P. Liney, L. Holloway, A. Walker, M. Barton, G. P. Delaney, S. Vinod, and W. Tome, The potential for an enhanced role for MRI in radiation-therapy treatment planning, Techol. Cancer Res. Treat. 2013, 12, 429–446.
9 S. Hanvey, A. H. Sadozye, M. McJury, M. Glegg, and J. Foster, The influence of MRI scan position on image registration accuracy, target delineation, and calculated dose in prostatic radiotherapy, Br. J. Radiol. 2012, 1256–1262.
10 B. Belaroussi, J. Milles, S. Carme, Y. M. Zhu, and H. Benoit-Cattin, Intensity non-uniformity correction in MRI: Existing methods and their validation, Med. Image Anal. 2006, 10, 234–246.
11 Y. Wang, P. J. Rossman, R. C. Grimm, S. J. Riederer, and R. L. Ehman, Navigator-echo-based real-time respiratory gating and triggering for reduction of respiration effects in three-dimensional coronary MR angiography, Radiology, 1996, 198, 55–60.
12 A. Fransson, P. Andreo, and R. Potter, Aspects of MR image distortions in radiotherapy treatment planning, Strahlenther. Onkol. 2001, 177, 59–73.
13 American Association of Physicists in Medicine (AAPM). Comprehensive QA for radiation oncology: Report of AAPM Radiation Therapy Committee Task Group 40, Med. Phys. 1994, 31, 581–618
14 P. Jezzard and S. Claire, "Sources of distortion in functional MRI data," Hum. Brain Mapp.1999, 8, 80–85.
15 N. Baldwin, K. Wachowicz, and B. G. Fallone, A two-step scheme for distortion rectification of magnetic resonance images, Med. Phys.2009, 36, 3917–3926.
16 M. L. Kessler, Image registration and data fusion in radiation therapy, Brit. J. Radiol. 2006, 79, S99–S108.
17 S. Devic, MRI simulation for radiotherapy treatment planning, Med. Phys. 2012, 39(11), 6701–6711.

The concepts and information presented in this paper are based on research and are not commercially available.

Contact

Ali Fatemi, Ph.D., MCCPM
Senior physicist, Director of MR Guided Radiotherapy Lab, Assistant professor
Departments of Radiology and Radiation Oncology
University of Mississippi Medical Center

2500 North State Street
Jackson, Mississippi 39216
USA
Phone: +1 (601)345-0135
afatemi@umc.edu

Meet Siemens Healthineers

Siemens Healthineers: Our brand name embodies the pioneering spirit and engineering expertise that is unique in the healthcare industry. The people working for Siemens Healthineers are totally committed to the company they work for, and are passionate about their technology. In this section we introduce you to colleagues from all over the world – people who put their hearts into what they do.

Oakville, Canada

Bart Schraa

Bart has been working as Charge MR Technologist for 10 years at the Daniel Den Hoed Cancer clinic of the Erasmus Medical Center Rotterdam in The Netherlands. During the period from 1999 to 2003 Bart has been providing training for Siemens MR systems worldwide as a free-lancer, and visited countries like Saudi-Arabia, Oman, Hong Kong and Taiwan. In 2003 Bart joined Siemens Netherlands in a full time position as Clinical Education Specialist. Bart obtained his Master of Science in Medical Imaging from the London South Bank University, UK, in 2010. In 2012, Bart accepted the position as Team Lead MR Applications in Canada and moved with his wife and three daughters (2, 5 and 8 years old at that time) to Canada.

How did you first come into contact with MRI?
My first contact with MRI was 30 years ago while I was still working as an X-ray technologist in the hospital. At that time, it was still a very mythical technology; there were only a few parameters that could be changed by buttons up and down such as TR and TE. Soon after I started working at the Daniel Den Hoed Cancer Clinic in Rotterdam, I became a (charge) MRI technologist. My first encounter working with a MRI system was a Siemens' MAGNETOM SP 63, 1.5T scanner which was soon upgraded to a MAGNETOM Vision system. During my last few years working at the Daniel Den Hoed, an additional 1.5T MAGNETOM Sonata system was installed. The platform was initially using the Numaris 3.5 operating system based on Unix, but soon upgraded to the first version of *syngo* MR (aka MREase).

What fascinates you most about MRI?
MRI is a technology that seems to evolve rapidly and continuously in the diagnostic imaging field. One of the greatest hurdles was the long reconstruction time due to the lack of speed of hardware. With the current computer hardware, it seems that almost everything is possible within a reasonable time frame. Emerging techniques like compressed sensing, which actually not that new, can now be applied in a clinical environment and provide the reconstructed images almost within an acceptable time. While at the beginning we had 10 minutes to plan for the next protocol since the previous one was still running, nowadays we have only a very short time available. Scan times as short as 1–2 minutes for regular protocols become more and more the standard. For examinations that involve breath-hold protocols we might only have 12 seconds to set up the next protocol. I believe that we are only (again) at the beginning of a new era of MRI thanks to the development of several new technologies. Soon the acquisition of the images is going to be much faster by use of new and latest techniques such as Simultaneous Multi-

Slice and Compressed Sensing. Therefore, we will need smarter software to help us keeping up with the speed of acquisition, this is where the Dot technology will continue to prove to be of great help.

What fascinates you most about your job?
I love to share my knowledge with and learn from our MAGNETOM users to make full use of our scanners. That applies both to our research oriented sites as well as clinical sites. Especially in Canada, there are so many different sites and most are running the Siemens Healthineers "high end" scanners. There are quite a few research sites in Canada, so there is never a dull moment. I really like that we work as a team of Clinical Education Specialists (CES) here and at the same time work together with the MR sales team as well as our technical colleagues from Customer Services. It feels like working as an MR team rather than only working as an MR CES team. I am also one of the Master MR Education Specialists, and each year we have a one week workshop in Erlangen to discuss my experiences with colleagues as well as with the developers. I also like to support our customers not only from a clinical point of view, but also explaining them how the latest techniques work from a physics point of view.

What do you think are the most important developments in MRI?
Since the examination times in MRI are still relatively long (2–3 minutes), there is quite some pressure from the healthcare insurance companies as well as from the governments to increase patient throughput for each center not just in Canada. Time is money! I think we are just at the start from what is going to be a very interesting development. The challenge is to make our software smarter by using Artificial Intelligence (AI). Siemens has already set the first big steps (using AI) by developing the Dot technology. The Dot engines allow for very streamlined workflows and standardization of the image quality and reduces the variance in scan time due to different technologists (with varying experience) operating the system. Apart from the Dot technology, techniques have been developed that make it possible to scan patients almost regardless of their ability to cooperate (for example holding their breath, or to lay still). These techniques include BLADE, StarVIBE, GRASP-VIBE, HeartFreeze and so on. Also, the potential reduction in scan time by Simultaneous Multi-Slice for TSE might be a game changer just like when we started with parallel imaging.

What would you do, if you could do for one month whatever you wanted?
Professionally I would like to make sure that all our protocols make use as much of the Dot technology as we have. Currently, not yet all protocols on the scanners are fully making use of this Dot technology. It would be great if all protocols on the scanners would make use of all aspects as much as possible such as AutoAlign and AutoCoverage apart from the guidance and parameter card. The benefit for our MAGNETOM users would be, through standardized positioning and coverage of the anatomy of interest, that there is a consistent quality of the examination. This facilitates easier reporting by the radiologist and allows for easier follow-up examinations. In the end this would benefit the quality of care for patients.

Privately, one of the trips that I would to do again would be to travel through Western Australia and the Northern Territories. It was something that I have done for only 10 days in the nineties. Taking a shower by diving into a lake (watch out for the fresh water crocodiles ☺) and sleeping under the sky with just a sleeping bag was such a great experience that I would like to do it again but this time with my wife and 3 kids (and all them are not favoring camping).

MR compatible laser bridge with direct laser steering[1] for precise patient marking and positioning

RT Dot Engine with optimized RT protocols for consistent scans

RT specific coil holders for proper positioning

Flex, UltraFlex and BioMatrix coils for excellent image quality

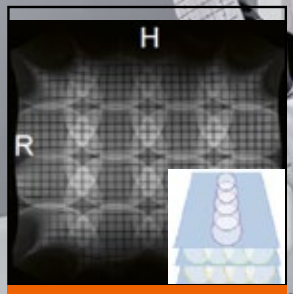

Dedicated **QA recommendations**

RT compatible indexed flat table tops and high accuracy table (z positioning accuracy +/- 0.5 mm)[2]

[1] Optional
[2] Accuracy for repositioning from one direction

Advance your clinical capabilities with the MAGNETOM RT Pro edition

siemens.com/magnetom-world-rt

SIEMENS Healthineers

The entire editorial staff at the Sydney Medical School at the University of Sydney, Australia and at Siemens Healthineers extends their appreciation to all the radiation oncologists, technologists, physicists, experts, and scholars who donate their time and energy – without payment – in order to share their expertise with the readers of MAGNETOM Flash.

MAGNETOM Flash – Imprint

Publisher:
Siemens Healthcare GmbH
Magnetic Resonance,
Karl-Schall-Str. 6, D-91052 Erlangen, Germany

Editor-in-chief:
Antje Hellwich
(antje.hellwich@siemens-healthineers.com)

Guest Editor:
Professor Paul Keall
Professor and NHMRC Senior Principal
Research Fellow
Director of the ACRF Image X Institute
Sydney Medical School, Australia

Editorial Board:
Reto Merges; Wellesley Were;
Sunil Kumar S.L., Ph.D.;
Gary R. McNeal, MS (BME)

Review Board:
Matthias Drobnitzky; Daniel Fischer;
Elena Nioutsikou, Ph.D.; Efren Ojeda;
Martin Requardt, Ph.D.; Glen Roberts;
Gregor Thörmer, Ph.D.

Production:
Norbert Moser, Clemens Ulrich
Siemens Healthcare GmbH

Layout:
Agentur Baumgärtner,
Friedrichstr. 4, D-90762 Fürth, Germany

Printer:
G. Peschke Druckerei GmbH,
Taxetstr. 4, D-85599 Parsdorf b. Munich, Germany

We welcome your questions and comments about the editorial content of MAGNETOM Flash. Please contact us at magnetomworld.med@siemens.com.

Manuscripts as well as suggestions, proposals and information are always welcome; they are carefully examined and submitted to the editorial board for attention. MAGNETOM Flash is not responsible for loss, damage, or any other injury to unsolicited manuscripts or other materials. We reserve the right to edit for clarity, accuracy, and space. Include your name, address, and phone number and send to the editors, address above.

MReadings: MR in RT is also available online:

www.siemens.com/magnetom-world-rt

On account of certain regional limitations of sales rights and service availability, we cannot guarantee that all products included in this brochure are available through the Siemens sales organization worldwide. Availability and packaging may vary by country and is subject to change without prior notice. Some/All of the features and products described herein may not be available in the United States.

The information in this document contains general technical descriptions of specifications and options as well as standard and optional features which do not always have to be present in individual cases, and which may not be commercially available in all countries. Due to regulatory reasons their future availability cannot be guaranteed. Please contact your local Siemens organization for further details.

Siemens reserves the right to modify the design, packaging, specifications, and options described herein without prior notice. Please contact your local Siemens sales representative for the most current information.

Note: Any technical data contained in this document may vary within defined tolerances. Original images always lose a certain amount of detail when reproduced.

Siemens Healthineers Headquarters
Siemens Healthcare GmbH
Henkestr. 127
91052 Erlangen
Germany
Phone: +49 9131 84-0
siemens-healthineers.com

Published by Siemens Healthcare GmbH · Order No. A91MR-1100-93C-7600 · Printed in Germany · 5850 05181.5 ·